STRUCTURE OF THE SUMATRA-ANDAMAN SUBDUCTION ZONE

by

Jeremy Dale Pesicek

A dissertation submitted in partial fulfillment of

the requirements for the degree of

Doctor of Philosophy

(Geophysics)

at the

UNIVERSITY OF WISCONSIN-MADISON

2009

Abstract

We have conducted studies of the Sumatra-Andaman subduction zone using newly available teleseismic data resulting from the aftershock sequences of the 2004, 2005, and 2007 great earthquakes that occurred offshore of the island of Sumatra. In order to better exploit the new data, existing methodologies have been adapted and advanced in several ways to obtain results at a level of precision not previously possible from teleseismic data. Seismic tomography studies of the mantle were conducted using an improved iterative technique that accounts for fine-scale three-dimensional (3-D) velocity variations inside the study region and coarser global velocity variations outside the region. More precise earthquake locations were determined using a double-difference technique that has been extended to teleseismic distances using spherical ray tracing through the nested 3-D regional-global velocity models. Earthquake relocation was included in the iterative tomography scheme and was found to significantly enhance the recovery of slab velocity anomalies. Finally, because crustal structure is poorly constrained by the teleseismic data, 3-D density modeling of the crust was conducted using newly available satellite gravity data and a spherical prism gravity algorithm.

The results of these studies better constrain the structure of the Sumatra-Andaman subduction zone, including the geometry of the mantle slab, position of the megathrust, and structural features of the downgoing plate. Tomography results reveal continuous upper mantle slab anomalies with significant variations in dip throughout the region. Broad curvature of the fast anomalies beneath northern Sumatra, similar to curvature of the trench and volcanic arc at the surface, is interpreted as folding of the upper mantle

slab. Earthquake relocations show systematic shifts of the hypocenters to the northeast and to shallower depths, each with average changes of 5 km. Reduced scatter in the relocations better constrain the megathrust plate boundary and the regions of coseismic slip during the 2004 and 2005 great earthquakes. In addition, the relocations reveal discrete seismic features on the downgoing plate not previously visible in teleseismic catalogs. The new velocity model and earthquake locations provide the most comprehensive view of the deep structure of the Sumatra-Andaman subduction zone yet available.

Acknowledgments

I am very thankful to have had Cliff Thurber as my advisor during my graduate studies at the University of Wisconsin. Cliff is a fantastic advisor who has helped me in innumerable ways over the past five years and these words will do little to convey the amount of gratitude that I feel toward him. Thank you, Cliff.

Several other faculty members have also been helpful throughout my graduate studies. Thanks to Kurt Feigl, Harold Tobin, Brad Singer, Dante Fratta, Laurel Goodwin, and Chuck DeMets for their efforts to improve my writing and thinking about my thesis studies. I am also very grateful to have had the technical assistance of Lee Powell at my disposal over the years. His wizardry at the computer was invaluable to me. I also thank Heather DeShon and Haijiang Zhang for their support in various forms over the years, and Sri Widiyantoro, Bob Engdahl, Tim Masterlark, and Mohammand Asgarzadeh for help with various aspects of the research.

My time as a graduate student has been overall quite enjoyable and I owe many people for enhancing my graduate life both inside and outside the realm of science. In no particular order, I thank my parents, Dale and CeCe Pesicek, Ninfa and Val Bennington, Paul Riley, Tim Oleson, Bryn Benford, Jennie Cook, Karen Mullins, Shirley Baxa, Bill Unger, Guoqing Lin, Ellen Syracuse and Francisco Correa-Mora. Finally, over the past year or so I owe much of my happiness to MaryRuth Kotelnicki and I thank her for all her support while I was finishing and defending my dissertation. Financial support for my graduate studies was provided by the National Science Foundation and by NASA.

Table of Contents

List of Figures and Tables

Chapter 2

Chapter 3

Chapter 4

Chapter 5

Chapter 6

CHAPTER 1: Introduction

The 26 December 2004 great Sumatra-Andaman Earthquake is the largest earthquake (Mw 9.1) to have occurred in the last 40 years and is one of the largest ever recorded by seismic instruments, exceeded only by the 22 May 1960 Chile great earthquake (Mw 9.5) and the 28 March 1964 Alaska great earthquake (Mw 9.2). It released as much energy as the United States uses in 6 months (4.3×10^{18} J) [*Bilham,* 2005]. Seafloor motion during the earthquake displaced 30 km^3 of seawater, causing the most devastating tsunami in history, which killed hundreds of thousands of people. Its seismic waves were the first from an M>9 earthquake to be recorded by the global network of broadband seismometers, and its effects were still being recorded weeks afterward. Ground motions from the earthquake exceeded 1 cm at every point of the Earth's surface [*Park et al.,* 2005].

The complexity of the rupture of the Sumatra-Andaman great earthquake is unprecedented and has been the subject of many studies [e.g., *Ammon et al.,* 2005; *Kruger and Ohrnberger,* 2005; *Gahalaut et al.,* 2006; *Piatanesi and Lorito,* 2007]. It was followed 3 months later by the second largest earthquake to have occurred in the past 40 years, the Mw 8.6 Nias Island earthquake, which ruptured a smaller patch of the megathrust directly south of the 2004 rupture. Together these two events ruptured ~1600 km of the boundary between the downgoing and overriding plates [*Lay et al.,* 2005] and generated over 5000 teleseismically-recorded aftershocks within the first 36 weeks following the 2004 event [*Dewey et al.,* 2007]. The subduction zone responsible for these events and their aftershocks, and in particular the region between the 2004 and

2005 epicenters, is highly complex. In the broadest sense, the plate boundary accommodates northward motion of the Indo-Australian plate beneath the Eurasian plate along the regional Sunda Trench. The convergence along this trench is highly oblique, and has led to the development of a forearc microplate and numerous subparallel faults that accommodate the along-strike component of convergence. These include the Sumatra fault that runs the entire length of Sumatra Island, and various backarc ridge and transform faults in the Andaman Sea, which join the Sumatra fault offshore northern Sumatra. Since the work of Fitch [1972], it has been recognized as the classic example of slip partitioning due to the highly oblique convergence.

In the region of the epicenters of the 2004 and 2005 great earthquakes, additional complexity arises at the plate boundary. This region hosts subduction of the north trending Investigator Fracture Zone (IFZ) and the Wharton Fossil Rift (WFR). In addition, the trench and the volcanic arc exhibit a change in curvature in this region as their orientation shifts from NW to a more westerly trend before again turning northwestward north of Sumatra. Perhaps not coincidentally, this region of curvature of the plate boundary correlates with the location of the axis of the diffuse deformational boundary between the Indian and Australian plates, which are known to exhibit relative motion with respect to one another as they both march northward toward collision with the Eurasian plate [e.g. *Wiens et al.,* 1986].

As a result of the 2004 and 2005 great earthquakes and the wealth of modern digital seismic and geodetic data they have created, the complex tectonic boundary on which these two events occurred has become the focus of many studies by various groups

of geophysicists. These data have allowed detailed investigations of the events themselves and their effects, and also of the structure of the plate boundary. Because of the remoteness of the subduction zone and the uneven distribution of local seismic stations in the region, there is very limited local seismic data. Thus, global teleseismic catalogs provide the most comprehensive datasets of seismicity along the subduction zone where these two great earthquakes occurred. Yet, teleseismic data are inherently low-resolution data. The large distance seismic waves travel to reach far off stations acts to filter out much of the most informative high frequency components. Finding new ways to better exploit these data are critical if we hope to gain further insight into the plate boundary on which the great earthquakes of 2004 and 2005 occurred.

In the following chapters, I present several studies in which existing methodologies have been advanced and adapted for use on the newly available teleseismic data from the Sumatra, Andaman Islands, and Burma segments of the Sunda subduction zone. In chapter 2, I present mantle tomography results for the region from a linear inversion of travel time delays using methodology modified from Widiyantoro and van der Hilst [1996; 1997]. The results of this chapter were published in *Geophysical Research Letters* in 2008 [*Pesicek et al.,* 2008]. In Chapter 3, I have employed a fully 3-D nonlinear technique to solve the same tomography problem, with methodology based on the work of Widiyantoro et al. [2000]. I have advanced this methodology in several ways and have obtained an improved iterative solution that properly accounts for source mislocation. The results of this chapter have passed coauthor approval and will likely be submitted in September 2009.

Chapter 4 deals more fully with the earthquake relocation method first used in Chapter 3. In chapter 4, I discuss the extension of the double-difference tomography algorithm of Zhang and Thurber [2003] to teleseismic distances in order to improve upon the accuracy and precision of the teleseismic earthquake locations in the Sumatra-Andaman region. I tested the algorithm's relocation capabilities and discuss the impacts of the location improvements on features of the subduction boundary and its seismogenic zone. The method and its results will be submitted for publication, after coauthor review and further analysis of the relocations has been performed.

Finally, in Chapter 5 I stray from studies of teleseismicity in the region and attempt to constrain 3-D structural heterogeneity of the subduction boundary at shallow depths (where tomography resolution is minimal) using satellite gravity data. I constructed a starting density model based on existing Finite Element Model (FEM) designs [*Masterlark and Hughes,* 2008] and made forward iterative adjustments to it to better match long wavelength features of the gravity signal. The results of this chapter are currently awaiting feedback from coauthors. This work may be included in future generations of FEMs of the region, but might also be published as a separate paper.

This dissertation presents work that is largely collaborative in nature. Therefore, in addition to listing coauthors at the beginning of each chapter, I would like to briefly summarize each coauthor's major contributions to the work in this dissertation. Chapters 2-4 were conducted using freely available data from the International Seismological Center (ISC) and the National Earthquake Information Center (NEIC). However, these data were compiled by E.R. Engdahl and improved upon by the Engdahl, van der Hilst,

and Buland (EHB) method [*Engdahl et al*., 1998, 2007] before their use in Chapters 2-4. Furthermore, H.R. DeShon improved the picks for a small subset of these data using waveform cross-correlation (CC) techniques, which were also used to form the precise CC differential times discussed in Chapter 4. The tomography algorithm that formed the basis of Chapters 2 and 3 was provided to us and supported by S. Widiyantoro. The double-difference (DD) relocation algorithm used in Chapters 3 and 4 was developed for use in the Sumatra region by H. Zhang, with assistance and modifications coming from C. Thurber and me. The adaptation for depth phase ray tracing to both the tomography and relocation codes was developed and tested by C. Thurber and me. The spherical prism gravity algorithm used in Chapter 5 was provided to us and supported by M. Asgarzadeh and T. Masterlark provided the initial density model. However, the responsibility for the results and interpretations discussed herein is mine.

References

Ammon, C. J. et al. (2005), Rupture Process of the 2004 Sumatra-Andaman Earthquake, *Science, 308*, 1133-1139.

Bilham, R. (2005), A flying start, then a slow slip, *Science, 308*, 1126-1127.

Dewey, J. W., G. Choy, B. Presgrave, S. Sipkin, A. C. Tarr, H. Benz, P. Earle, and D. Wald (2007), Seismicity associated with the Sumatra-Andaman Islands earthquake of 26 December 2004, *Bull. Seismol. Soc. Am., 97*, 25-42.

Engdahl, E. R., van der Hilst, R. D., and R. Buland (1998), Global teleseismic earthquake relocation with improved travel times and procedures for depth determination, *Bull. Seismol. Soc. Am., 88*, 722-743.

Engdahl, E. R., A. Villasenor, H. R. DeShon, and C. H. Thurber (2007), Teleseismic relocation and assessment of seismicity (1918-2005) in the Region of the 2004 Mw 9.0 Sumatra-Andaman and 2005 Mw 8.6 Nias Island great earthquakes, *Bull. Seismol. Soc. Am., 97*, S43-61.

Fitch, T. J. (1972), Plate convergence, transcurrent faults, and internal deformation adjacent to southeast Asia and the western Pacific, *J.Geophys.Res, 77*, 4432–4460.

Gahalaut, V. K., B. Nagarajan, J. K. Catherine, and S. Kumar (2006), Constraints on 2004 Sumatra–Andaman earthquake rupture from GPS measurements in Andaman–Nicobar Islands, *Earth Planet. Sci. Lett., 242*, 365-374.

Kruger, F. and M. Ohrnberger (2005), Tracking the rupture of the Mw = 9.3 Sumatra earthquake over 1,150 km at teleseismic distance, *Nature, 435*, 937-939.

Lay, T., H. Kanamori, C. J. Ammon, M. Nettles, S. N. Ward, R. C. Aster, S. L. Beck, S. L. Bilek, M. R. Brudzinski, and R. Butler (2005), The great Sumatra-Andaman earthquake of 26 December 2004, *Science, 308*, 1127-1133.

Masterlark, T. and K. L. H. Hughes (2008), Next generation of deformation models for the 2004 M9 Sumatra-Andaman earthquake, *Geophys. Res. Lett., 35*, L19310.

Park, J., T. R. A. Song, J. Tromp, E. Okal, S. Stein, G. Roult, E. Clevede, G. Laske, H. Kanamori, and P. Davis (2005), Earth's free oscillations excited by the 26 December 2004 Sumatra-Andaman earthquake, *Science, 308*, 1139-1144.

Pesicek, J. D., C. H. Thurber, S. Widiyantoro, E. R. Engdahl, and H. R. DeShon (2008), Complex slab subduction beneath northern Sumatra, *Geophys. Res. Lett., 35*, L20303.

Piatanesi, A. and S. Lorito (2007), Rupture Process of the 2004 Sumatra-Andaman Earthquake from Tsunami Waveform Inversion, *Bull. Seismol. Soc. Am., 97*, S223-231.

Widiyantoro, S., A. Gorbatov, B. L. N. Kennett, and Y. Fukao (2000), Improving global shear wave traveltime tomography using three-dimensional ray tracing and iterative inversion, *Geophys. J. Int., 141*, 747-758.

Widiyantoro, S. and van der Hilst, R. D. (1996), Structure and Evolution of Lithospheric Slab Beneath the Sunda Arc, Indonesia, *Science, 271*, 1566-1570.

Widiyantoro, S. and van der Hilst, R. D. (1997), Mantle structure beneath Indonesia inferred from high-resolution tomographic imaging, *Geophys. J. Int., 130*, 167-182.

Wiens, D. A., S. Stein, C. Demets, R. G. Gordon, and C. Stein (1986), Plate tectonic models for Indian Ocean "intraplate" deformation; Intraplate deformation; characteristics, processes and causes, *Tectonophysics, 132*, 37-48.

Zhang, H. and C. H. Thurber (2003), Double-difference tomography: the method and its application to the Hayward Fault, California, *Bull. Seismol. Soc. Am., 93*, 1875-1889.

CHAPTER 2: Complex Slab Subduction Beneath Northern Sumatra

J. D. Pesicek, C. H. Thurber, S. Widiyantoro, E. R. Engdahl, and H. R. DeShon

Abstract

New data provided by the 2004-2005 Sumatra-Andaman great earthquake sequences allows us to image with improved detail the *P*-wave velocity structure beneath Sumatra and adjacent regions. Below northern Sumatra, we find that the slab is folded at depth, exhibiting geometry similar to that of the volcanic arc and the trench at the surface. We speculate that this fold plays a major role in the segmentation of the Sumatra megathrust, and may impede rupture propagation in the region. North of Sumatra, significant slab material in the mantle transition zone is imaged for the first time, and we infer the presence of a major tear between the upper mantle and transition zone there.

2.1 Introduction

The boundary between the Andaman and Sunda subduction zones is marked by a distinct bend in the trench offshore northern Sumatra. This area also hosts subduction of the Investigator Fracture Zone (IFZ) and the Wharton Fossil Ridge (WFR), and is the locus of the southeast termination point of the diffuse deformational boundary between the Indian and Australian plates. It is also the boundary between the rupture areas of the 2004 Mw 9.1 and 2005 Mw 8.7 megathrust earthquakes (Figure 2.1). Consequently, there is great interest in characterizing the nature of the incoming and downgoing plate in order to determine how the plate geometry may be affecting subduction and seismogenesis. In this study, we perform a tomographic inversion of teleseismic data using a nested regional-global approach [*Widiyantoro and van der Hilst,* 1996] in order to determine the *P*-wave velocity structure of the Indonesia region. We focus on the Burma (Myanmar), Andaman, and Sumatra subduction zones (Figure 2.1), where new data provided by the 2004-2005 megathrust sequences (Figure 2.S1) [*Engdahl et al.,* 2007] provide a substantial increase in ray coverage (Figure 2.S2). This increase in data allows us to use smaller model cell sizes and results in significant improvements in slab amplitude recovery. In our new model, the fast subducting slab is well imaged in the upper mantle throughout the region, with significant variations in dip along strike. We interpret folding of the subducting slab beneath northern Sumatra and speculate on its relation to shallow structure and seismogenesis. In addition, we present evidence for a significant tear in the upper mantle slab below Burma. Finally, we show that, in the lower mantle, the ancient Neo-Tethys slab is a distinct and prominent feature.

2.2 Data and Methodology

We inverted global teleseismic arrival time data for events that are well constrained by the Engdahl, van der Hilst, and Buland (EHB) criteria for single event relocation [*Engdahl et al.,* 1998]. Our dataset includes global earthquakes for the time period 1964-2006 and earthquakes in the Sumatra region from 1918-2006 [*Engdahl et al.,* 2007]. This includes 1,664,212 first arriving *P* phases and 38,801 depth phases (26,877 *pP* and 11,924 *pwP*), which increase upper mantle sampling. We employed the nested regional-global tomographic method of *Widiyantoro and van der Hilst* [1996, 1997]. The model space was parameterized into 0.5º cells regionally with cell thickness increasing with depth, from 35 km at the surface to 110 km at the base of the regional model at 1500 km depth. While previous studies have focused on the southern and eastern subduction zones of Indonesia, we focus on the northwestern subduction zones and we have extended the northern boundary of the regional model to 25º N (compared to 15º N in *Widiyantoro and van der Hilst* [1996, 1997]) to fully encompass the Andaman and Burma subduction zones. The finer regional model cells are surrounded by 5º global cells that also vary in thickness to 2889 km depth, with an average thickness of ~180 km. We performed a single iteration, computing initial arrival time residuals relative to the ak135 global model [*Kennett et al.,* 1995]. We excluded arrivals with a residual greater than 3 standard deviations, which for our data is ~6 sec. The inverse solution was obtained via the conjugate gradient least squares algorithm *LSQR* [*Paige and Saunders,* 1982]. We conducted checkerboard resolution tests (Figures S3, S4) and synthetic slab

tests (Figures S5, S6) and we compared our model to other previously published Indonesian tomography images for which rigorous resolution tests have been conducted [*Hafkenscheid et al.,* 2001; *Replumaz et al.,* 2004; 1997; *Widiyantoro and van der Hilst,* 1996]. We observe all of the main large-scale mantle features of these studies along the Burma, Andaman, and Sumatra subduction zones, and our comparisons indicate similar recovery of features throughout the Indonesia region, with generally enhanced amplitude. Thus, we are confident that the features we discuss below are at least as well recovered and resolved as previous models and are superior in the Sumatra region, due to increased data coverage.

2.3 Discussion

We image a strong slab signature of fast *P*-wave anomalies along the Burma, Andaman, and Sumatra arcs at upper mantle depths (Figures 2.2, 2.3). The dip of the imaged slab varies from moderately dipping below Burma and northern Sumatra (25-50º) to more steeply dipping (60-90º) below the Andaman Islands and southern Sumatra (Figure 2.2). This variation in slab dip roughly correlates with the age of the incoming seafloor (steeper dips correlate with older subducting slabs) and agrees with the dip inferred by previous studies [*Kennett and Cummins,* 2005; *Shapiro et al.,* 2008] and with well-constrained teleseismic event relocations [*Engdahl et al.,* 2007]. The latter correlate well with the upper edge of the subducting slab (Figures 2.2, 2.S7).

Below northern Sumatra, there is a distinct change in the strike of the slab (Figure 2.3) that mimics the trend of the trench and the shape of the volcanic arc observed at the surface (Figure 2.1). At depth, however, the slab does not appear to be as gently curved. Rather, the slab segments northwest and southeast of the center of the bend are relatively planar and meet to form a relatively sharp fold (Figures 2.4, 2.S8). The shape of this fold and its position agree well with fast anomalies seen in previous tomographic studies [*Hafkenscheid et al.,* 2001; *Replumaz et al.,* 2004] at similar depths. In addition, *Fauzi et al*. [1996] also infer a deflection in the location of the slab in their study of seismicity below Toba Caldera. They used local earthquake relocations to deduce the slab location from depths of 75-175 km.

Given the correlation of this fold with the location of the bend in the trench and the volcanic arc and its inferred presence as shallow as 75 km depth [*Fauzi et al*. 1996], we infer that this fold is a primary and continuous feature of the subducting slab from the surface into the mantle transition zone. Although we cannot yet resolve this fold at crustal depths, projection of the inferred fold axis to the surface places it in the area of maximum curvature of the trench (Figure 2.S8). We expect that future higher resolution studies will delineate this fold at shallower levels.

The proximity of this slab fold to the locations of the 2004 and 2005 megathrust earthquakes (Figure 2.4) suggests that the fold may influence rupture propagation. *Briggs et al*. [2006] identify a saddle-shaped region on Simeulue Island that experienced minimal uplift from the 2004 and 2005 megathrust events. They suggest that this region may serve as an impediment to rupture propagation. The saddle could be the surface

expression of the fold axis and the structural cause for rupture termination hypothesized by *Briggs et al*. [2006]. Alternatively, the axis of this fold might be expressed on the megathrust as the tear inferred by *Briggs et al*. [2006] south of Simeule Island, between the Banyak Islands and Nias Island. *Shapiro et al*. [2008] show that the oceanic lithosphere subducting here is hotter and thinner than lithosphere subducting to the north and south. The megathrust below these islands likely hosts the subducted continuation of the WFR and/or the IFZ. A thinned and folded subducting slab could develop a tear that would influence rupture propagation along the megathrust.

If this fold is indeed continuous from the surface to at least 530 km depth as we contend, then this implies that the initiation of the bend in the subduction zone must have developed earlier than previously thought. *Richards et al*. [2007] estimate that the slab below Sumatra at 800 km depth began subducting at ~25 Ma. Assuming a constant rate of subduction, this implies that the folded slab now at 530 km depth began subducting at ~17 Ma. Recent studies of the tectonic evolution of SE Asia [*Replumaz et al*., 2004; *Richards et al*., 2007] do not show significant bending of the trench until ~5 Ma, and thus cannot account for this feature. If the lithospheric fold controls the bend in the trench, then bending must have begun prior to 5 Ma.

The origin of this fold, and the bend in the trench may be tied to the evolution of the Wharton spreading ridge, which first began subducting beneath Java at 70 Ma [*Whittaker et al*., 2007]. The lithospheric fold we observe in the upper mantle below Sumatra is likely the result of oblique subduction of the WFR, extinct since ~45 Ma [*Deplus et al*., 1998]. This would require the fold and the trench bend to have migrated

northwest with respect to the overriding plate, following the migration of the WFR [*Whittaker et al.,* 2007]. Alternatively, the fold may be a static feature of the plate boundary, independent of any structure on the downgoing plate. However, this seems unlikely, given the obliquity of subduction. We suspect that the fold is a result of deformation of the Indo-Australian plate along the thinned and weakened axis of the WFR. The structural complexities resulting from this scenario would certainly affect rupture propagation on the megathrust.

The upper mantle slab north of Sumatra, along the Andaman segment, appears to dip much more steeply, nearly 90° (Figure 2.2b), in good agreement with previous tomographic studies [*Kennett and Cummins,* 2005; *Shapiro et al.,* 2008]. This has been associated with slab roll back and extension in the Andaman Sea [*Kennett and Cummins,* 2005; *Richards et al.,* 2007] since at least 11 Ma [*Khan and Chakraborty,* 2005]. North of the Andaman segment, below Burma, the slab dips more moderately, about 30° (Figure 2.2a). Our results show that significant amounts of slab material exist in the transition zone below Indochina that had not been imaged in previous studies (Figures 2.2a, 2.3). The lack of continuity between upper mantle and transition zone anomalies (Figures 2.2a, 2.S9) below the Burma and Andaman arcs suggests that there may be a slab tear between these segments and the adjacent northern Sumatra segment. Despite vertical smearing in our results at these depths (as indicated by Figures 2.S3-2.S6), a clear contrast in the trend of the slab in the transition zone (530 and 615 km layers in Figure 2.3) as compared to shallower depths, suggests that the tear occurs in the slab above the transition zone. The cause and timing of this tear with respect to the tectonic

development of the region is unclear. However, it most likely initiated somewhere along the Burma segment, where slab separation is largest, and then propagated laterally southward toward the fold below northern Sumatra.

In the lower mantle below central and southern Sumatra, we see significant subhorizontal high velocity anomalies that generally appear contiguous with the upper mantle slab. These anomalies dip in the opposite direction (toward the southwest) to that of the slab in the upper mantle (Figures 2.2c-d). The depth, contrasting dip, and NW trend of the lower mantle features (Figure 2.3) suggest that they are all remnants of the ancient Neo-Tethyan oceanic lithosphere, subducted during the Cretaceous, that previous tomographic studies have observed and interpreted [e.g. *van der Hilst et al.,* 1997; *Van der Voo et al.,* 1999]. *Widiyantoro and van der Hilst* [1996] show distinctly separate anomalies below southern Sumatra and propose a slab tear in this region. In contrast, our higher-resolution results show that the slab extends through the transition zone, well into the lower mantle below southern Sumatra, and is not clearly distinguishable from the deeper, broader lower mantle anomalies. Thus, the location of the tear separating the upper mantle slab from the lower mantle remnant Neo-Tethys slab is most likely farther north below northern Sumatra.

2.4 Summary

Our new model reveals that the slab subducting below western Indochina and Sumatra exhibits a complex geometry that has developed as the region has evolved

tectonically. The most dramatic feature from our results is the fold in the slab below northern Sumatra, which may be acting as a barrier to rupture along the megathrust. The upper mantle slab below Burma appears separated from its deeper extension, implying that a tear exists there. Future plate reconstructions must account for both the folding and tearing of the slab evident in our results. Important outstanding issues include the cause and timing of folding, and the details of its potential influence on stress accumulation and rupture initiation and propagation.

Acknowledgements

This manuscript benefitted greatly from thoughtful reviews by Richard Briggs, James Conder, and Richard Allen. This material is based upon work supported in part by the National Science Foundation under grants EAR-0337495 (CT), EAR-0608988 (HD and CT), and EAR-0609613 (EE), and by NASA, under award NNX06AF10G. The data were provided by the ISC and NEIC. Figures were produced using GMT [*Wessel and Smith,* 1998] and TOMOEYE [*Gorbatov et al.,* 2004].

References

Ammon, C. J. et al. (2005), Rupture process of the 2004 Sumatra-Andaman Earthquake, *Science, 308*, 1133-1139.

Briggs, R. W. et al. (2006), Deformation and slip along the Sunda Megathrust in the great 2005 Nias-Simeulue earthquake, *Science, 311*, 1897-1901.

Coffin, M.F., L.M. Gahagan and L.A. Lawver, (1998), Present-day plate boundary digital data compilation. *University of Texas Institute for Geophysics Technical Report No. 174*, pp. 5.

Deplus, C., M. Diament, H. Hebert, G. Bertrand, S. Dominguez, J. Dubois, J. Malod, P. Patriat, B. Pontoise, and J. Sibilla (1998), Direct evidence of active deformation in the eastern Indian oceanic plate, *Geology, 26*, 131-134.

Engdahl, E. R., van der Hilst, R. D., and R. Buland (1998), Global teleseismic earthquake relocation with improved travel times and procedures for depth determination, *Bull. Seismol. Soc. Am., 88*, 722-743.

Engdahl, E. R., A. Villasenor, H. R. DeShon, and C. H. Thurber (2007), Teleseismic relocation and assessment of seismicity (1918-2005) in the Region of the 2004 Mw 9.0 Sumatra-Andaman and 2005 Mw 8.6 Nias Island great earthquakes, *Bull. Seismol. Soc. Am., 97*, S43-61.

Fauzi, R. McCaffrey, D. A. Wark, Sunaryo, and P. Y. Prih Haryadi (1996), Lateral variation in slab orientation beneath Toba Caldera, northern Sumatra, *Geophys. Res. Lett., 23*, 443-446.

Gorbatov, A., A. Limaye, and M. Sambridge (2004), Tomoeye; a Matlab package for visualization of three-dimensional tomographic models, *Geochem. Geophys. Geosyst., 5*.

Hafkenscheid, E., S. J. H. Buiter, M. J. R. Wortel, W. Spakman, and H. Bijwaard (2001), Modelling the seismic velocity structure beneath Indonesia; a comparison with tomography; Active subduction and collision in Southeast Asia (SEASIA), *Tectonophysics, 333*, 35-46.

Kennett, B. L. N. and P. R. Cummins (2005), The relationship of the seismic source and subduction zone structure for the 2004 December 26 Sumatra–Andaman earthquake, *Earth Planet. Sci. Lett., 239*, 1-8.

Kennett, B. L. N., E. R. Engdahl, and R. Buland (1995), Constraints on seismic velocities in the Earth from traveltimes, *Geophys. J. Int., 122*, 108-124.

Khan, P. K. and P. P. Chakraborty (2005), Two-phase opening of Andaman Sea: a new seismotectonic insight, *Earth Planet. Sci. Lett., 229*, 259-271.

Paige, C. and M. A. Saunders (1982), LSQR: An algorithm for sparse linear equations and least squares problems, *ACM Trans. Math. Soft., 8*, 43-71.

Replumaz, A., H. Kárason, van der Hilst, R. D., J. Besse, and P. Tapponnier (2004), 4-D evolution of SE Asia's mantle from geological reconstructions and seismic tomography, *Earth Planet. Sci. Lett., 221*, 103-115.

Richards, S., G. Lister, and B. L. N. Kennett (2007), A slab in depth: Three-dimensional geometry and evolution of the Indo-Australian plate, *Geochem. Geophys. Geosyst., 8*, Q12003.

Shapiro, N. M., M. H. Ritzwoller, and E. R. Engdahl (2008), Structural context of the great Sumatra-Andaman Islands earthquake, *Geophys. Res. Lett., 35*, 1-5.

Natawidjaja, D. H., K. Sieh, M. Chlieh, J. Galetzka, B. W. Suwargadi, H. Cheng, R. L. Edwards, J. Avouac, and S. N. Ward (2006), Source parameters of the great Sumatran megathrust earthquakes of 1797 and 1833 inferred from coral microatolls, *J. Geophys. Res.*, 111, 37.

van der Hilst, R. D., S. Widiyantoro, and E. R. Engdahl (1997), Evidence for deep mantle circulation from global tomography, *Nature, 386*, 578-584.

Van der Voo, R., W. Spakman, and H. Bijwaard (1999), Tethyan subducted slabs under India, *Earth Planet. Sci. Lett., 171*, 7-20.

Wessel, P. and Smith, W. H. F. (1998), New, improved version of generic mapping tools released, *EOS Trans. AGU, 79*, 579-579.

Whittaker, J. M., R. D. Müller, M. Sdrolias, and C. Heine (2007), Sunda-Java trench kinematics, slab window formation and overriding plate deformation since the Cretaceous, *Earth Planet. Sci. Lett.*, 255, 445-457.

Widiyantoro, S. and van der Hilst, R. D. (1996), Structure and evolution of lithospheric slab beneath the Sunda Arc, Indonesia, *Science, 271*, 1566-1570.

Widiyantoro, S. and van der Hilst, R. D. (1997), Mantle structure beneath Indonesia inferred from high-resolution tomographic imaging, *Geophys. J. Int., 130*, 167-182.

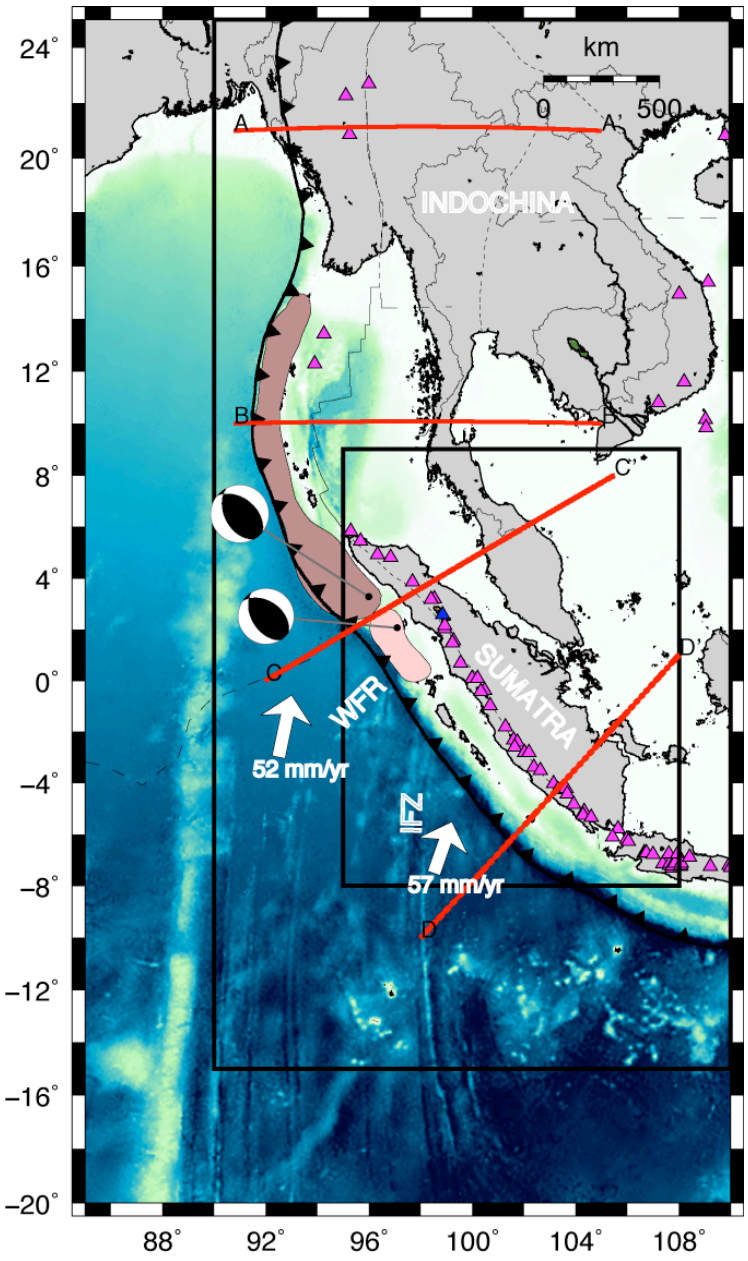

Figure 2.1. Map of the Burma, Andaman, and Sumatra subduction zones showing the positions of the cross-sections in Figure 2.2. Also shown are the Harvard Centroid Moment Tensor solutions, epicenters, rupture areas [*Ammon et al.*, 2005] of the 2004 and 2005 megathrust earthquakes, and the locations of the Investigator Fracture Zone (IFZ) and Wharton Fossil Ridge (WFR). Volcanoes are shown as magenta triangles (Toba Caldera is blue). ETOPO5 bathymetry, tectonic boundaries [*Coffin et al.*, 1998], and convergence vectors [*Sieh and Natawidjaja,* 2000] are also shown. The west and south edges of our regional model are shown, and correspond to the limits of the layers in Figure 2.3. The inset box shows the area represented in Figures 2.4 and 2.S6.

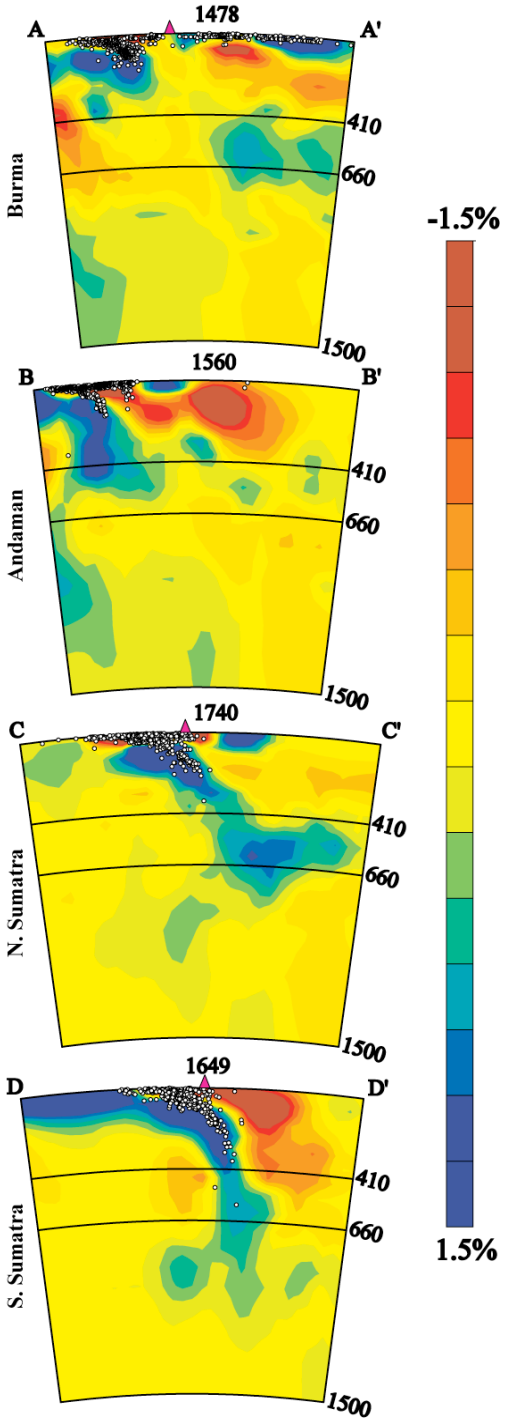

Figure 2.2. Cross-sections through the model (positions shown in Figure 2.1) showing the contrasting dips of the slab in different regions. Perturbations relative to ak135 [*Kennett et al*., 1995] are shown from -1.5% to 1.5%. Earthquake relocations [*Engdahl et al*., 2007] (circles) and volcano positions (triangles) are also shown. For each region, cross-section lengths are listed in km at the top.

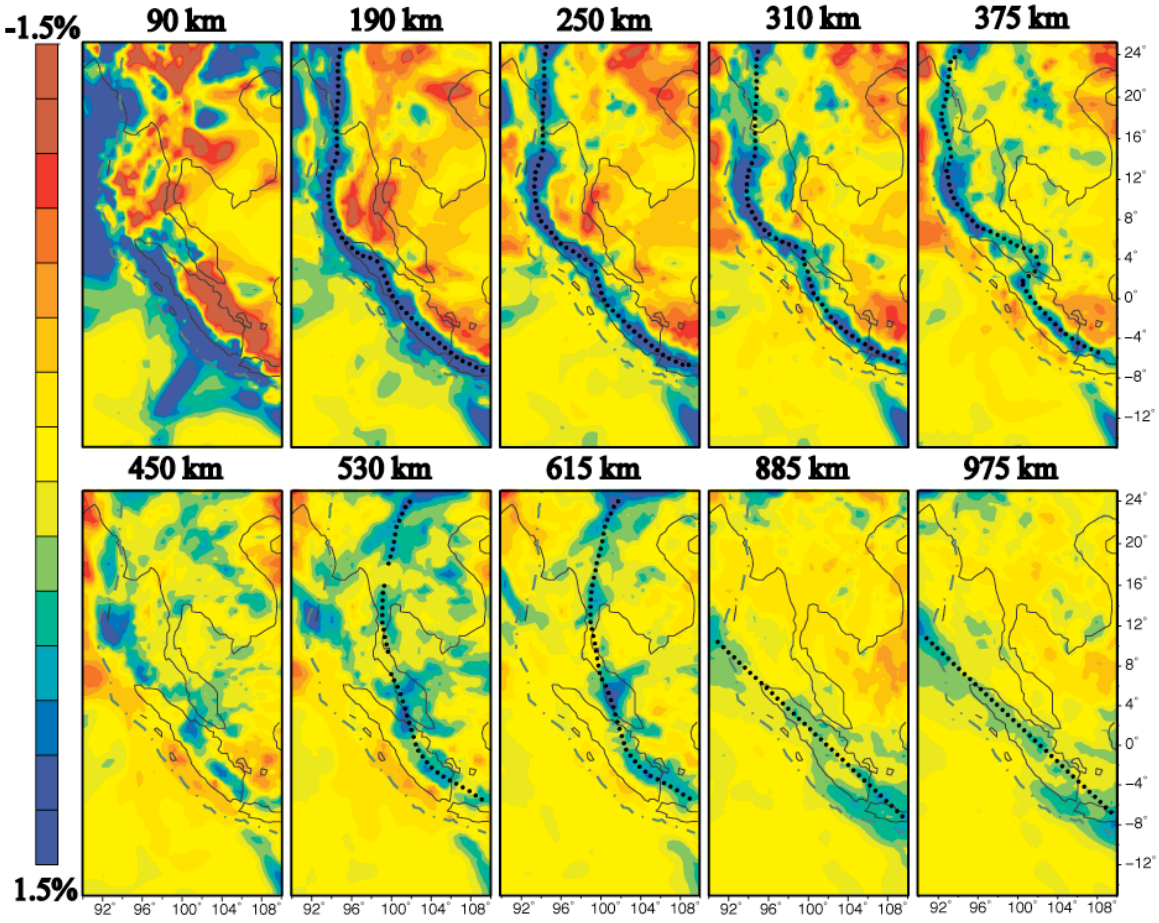

Figure 2.3. Selected model depth layers with the same scale as Figure 2.2. A fold in the upper mantle slab is evident from 190-530 km. In general, three slab trends are inferred from the model results and shown as dotted black lines: 1) the shallow trend mimicking current subduction plate boundaries, 2) the concave east shape of transition zone material, and 3) the NW-SE trend of the lower mantle remnant Neo-Tethys slab.

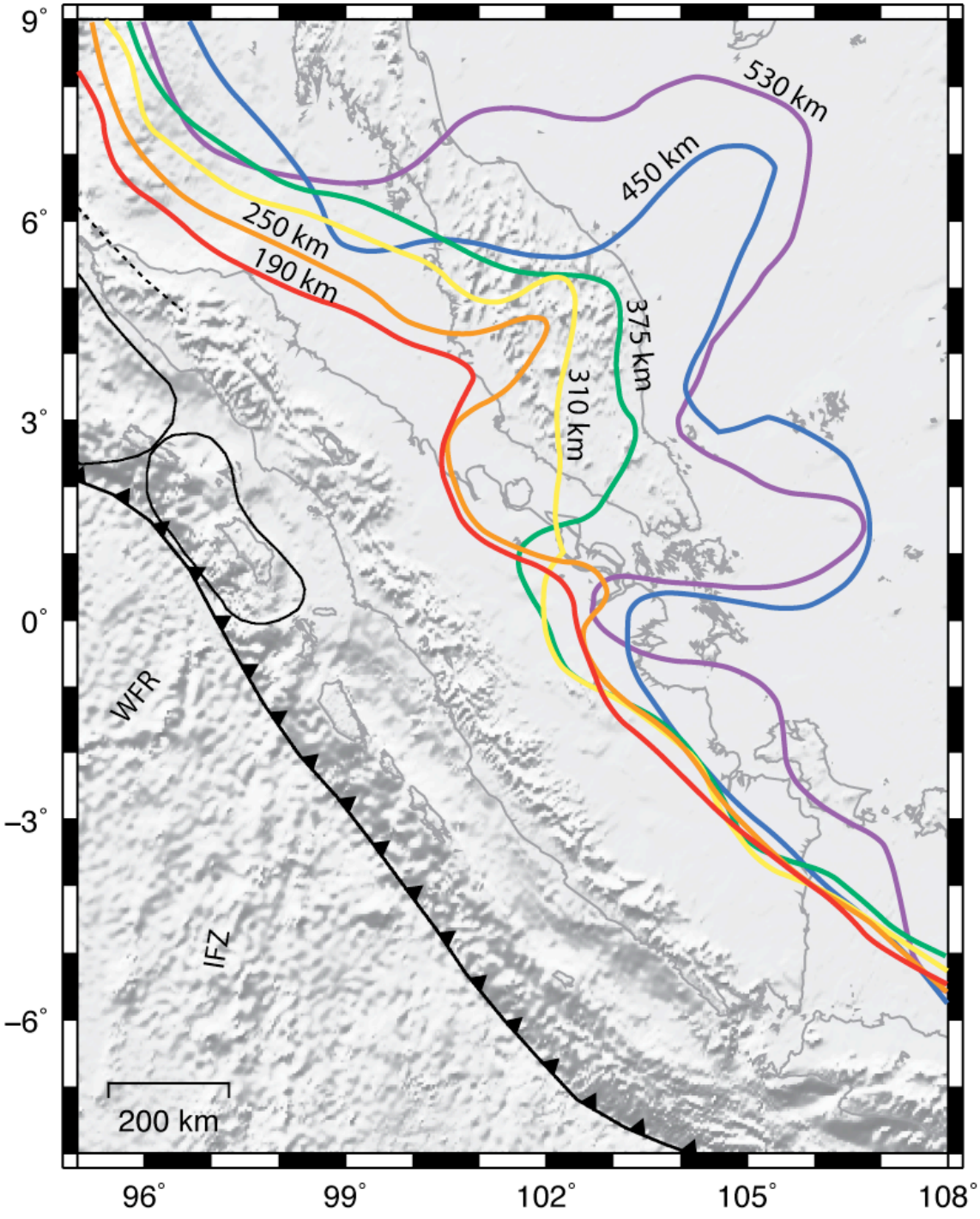

Figure 2.4. Map showing smoothed tracings of the +0.5% velocity perturbation contours at model layer depths from 190-530 km. Bending of the contours illustrates folding of the subducting slab at these depths (see also Figure 2.S6).

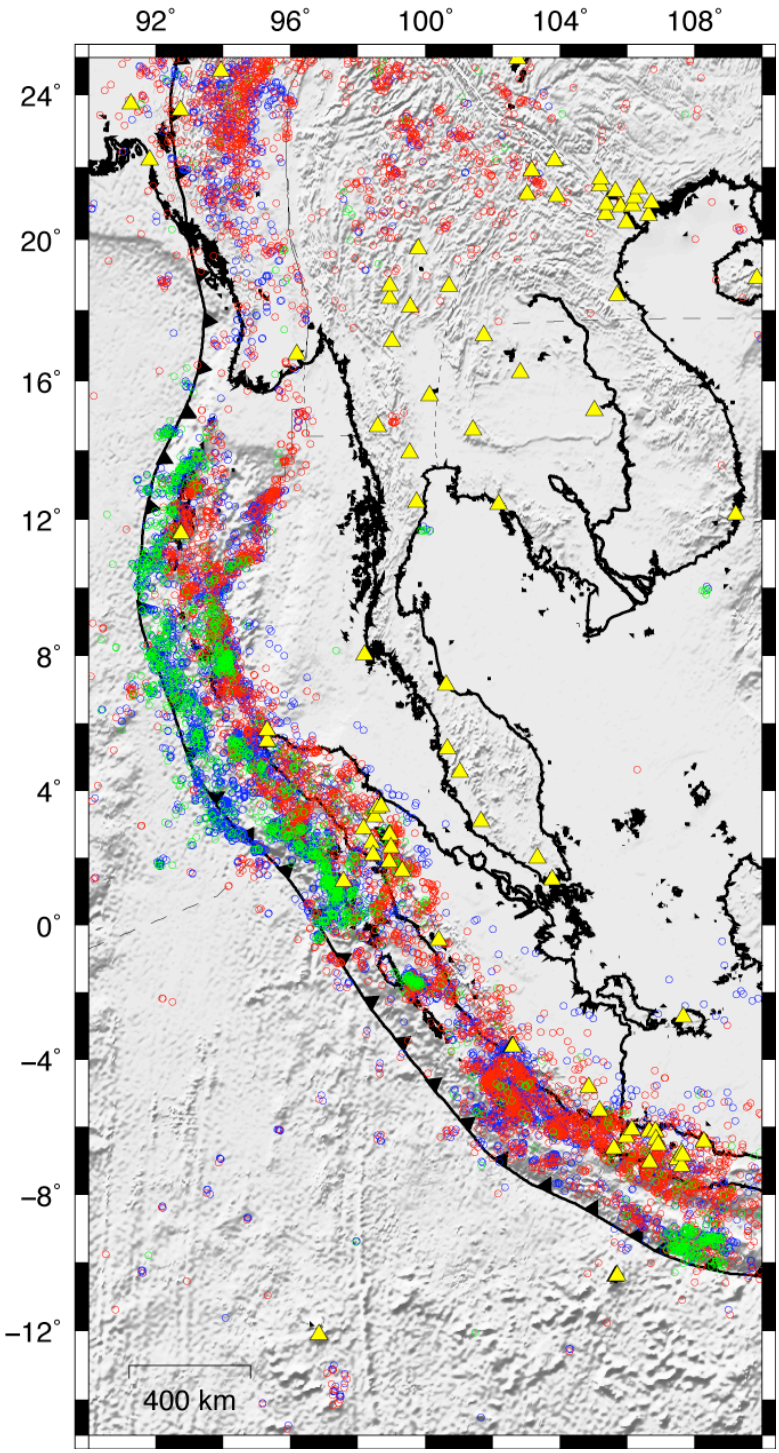

Figure 2.S1. Map of the regional model space showing the distribution of local sources and receivers (yellow triangles). Events prior to December 2004 are shown in red, events following the 2004 great earthquake through 2006 are shown in green, both of which are overlain on the locations of the *pP* and *pwP* bounce points (blue).

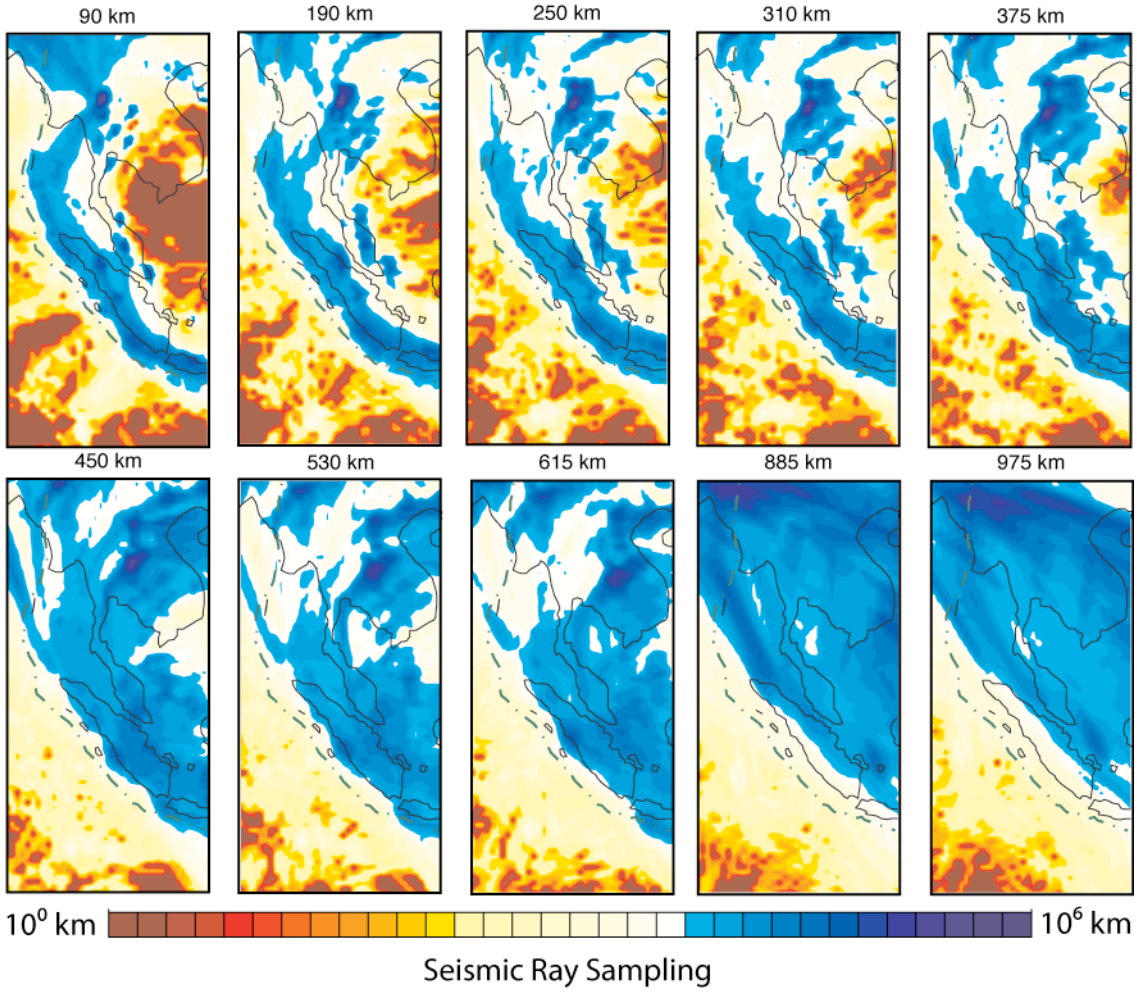

Figure 2.S2a. Seismic ray sampling (including *pP* and *pwP*) prior to the December 2004 great earthquake plotted logarithmically by total ray length in each model cell.

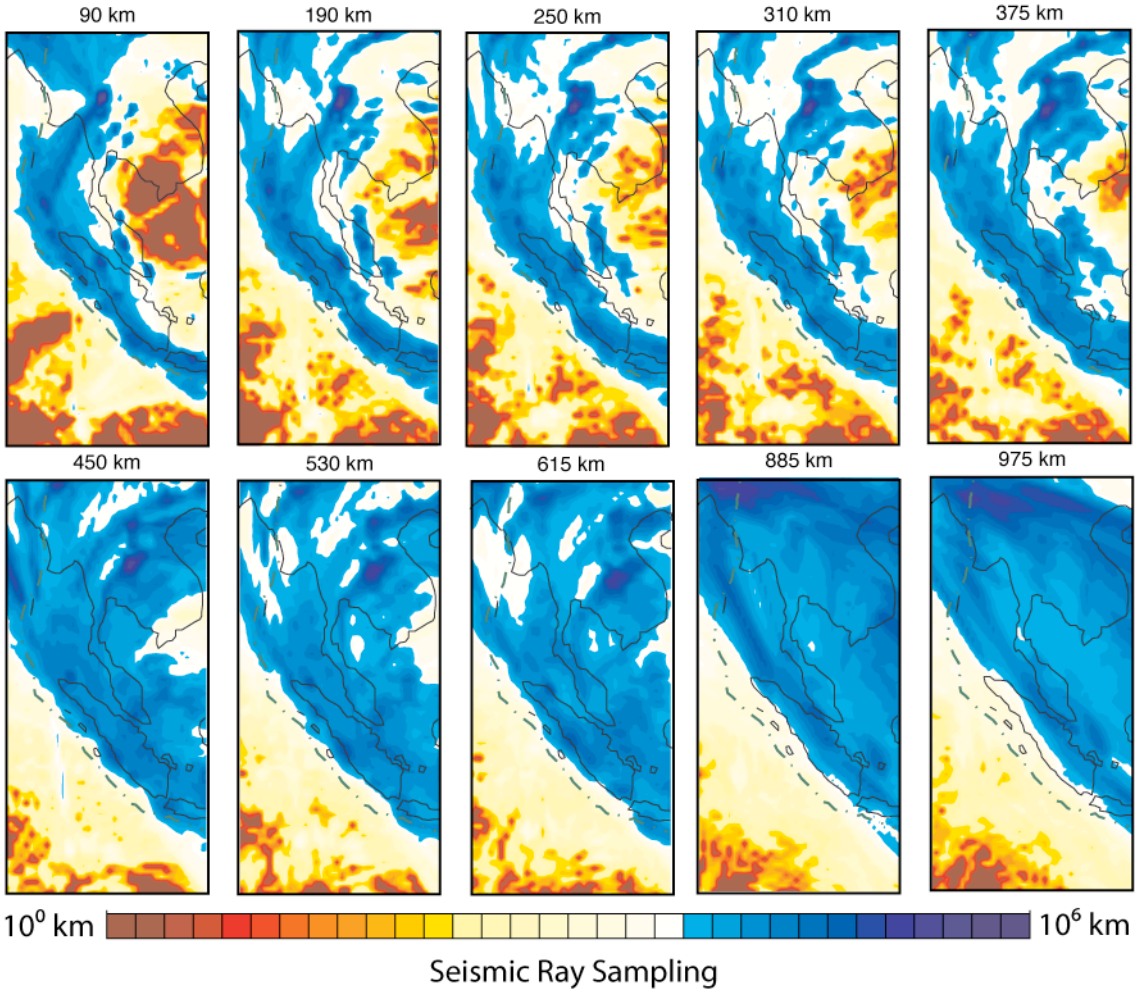

Figure 2.S2b. Seismic ray sampling of all data used in inversion plotted logarithmically by total ray length in each model cell. The addition of data from the 2004-2005 great earthquake sequences (see Figure 2.S1) has resulted in better ray sampling in the region compared to previous studies.

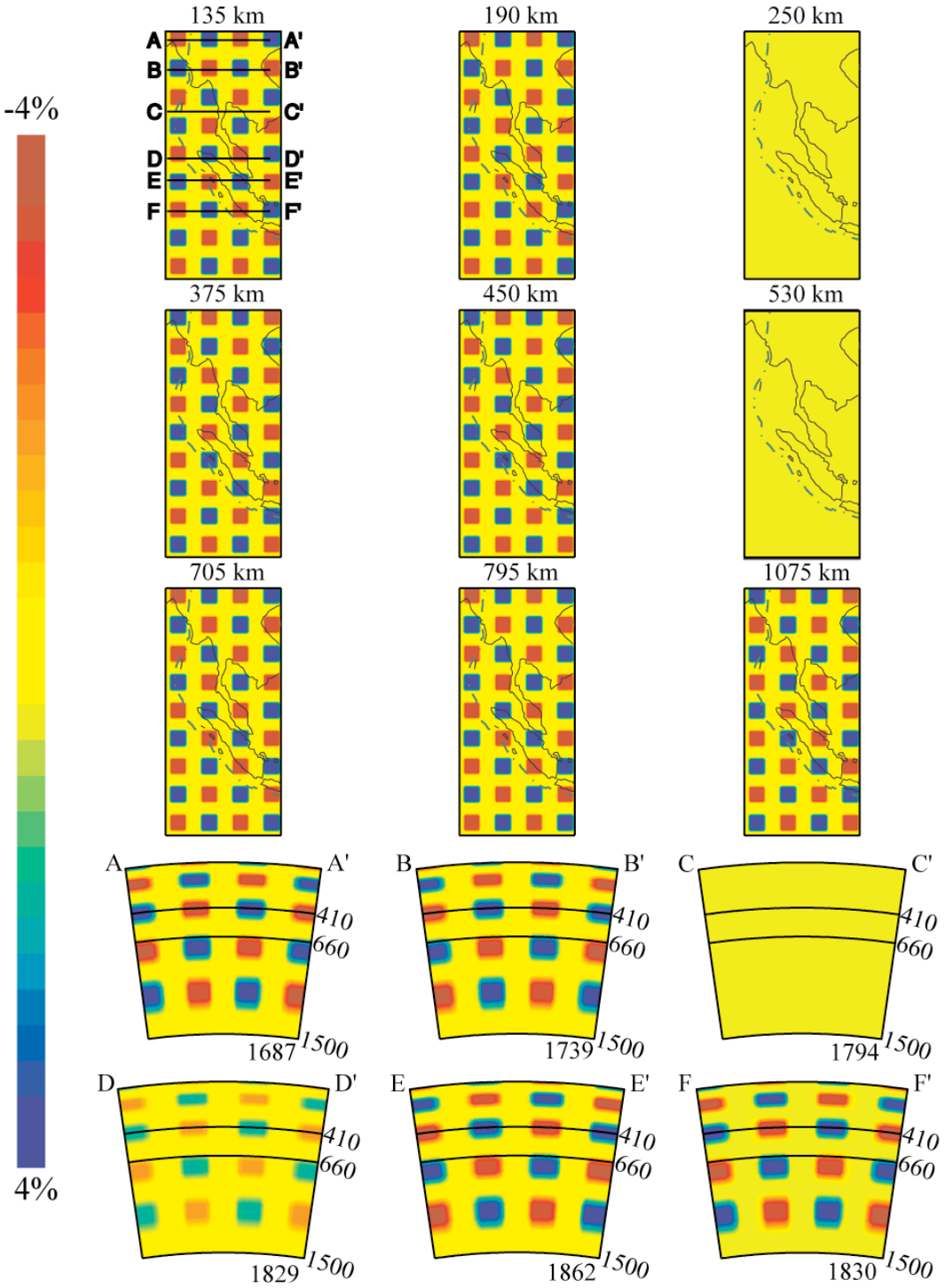

Figure 2.S3a. Input model for synthetic checkerboard resolution tests. One second of random noise is added to the residuals between the predicted travel times and those calculated through this input model. Checkers are 4% anomalies, and are 2.5° by 2.5° and two layers thick. Layers and cross-sections without input checkers are shown in order to assess smearing.

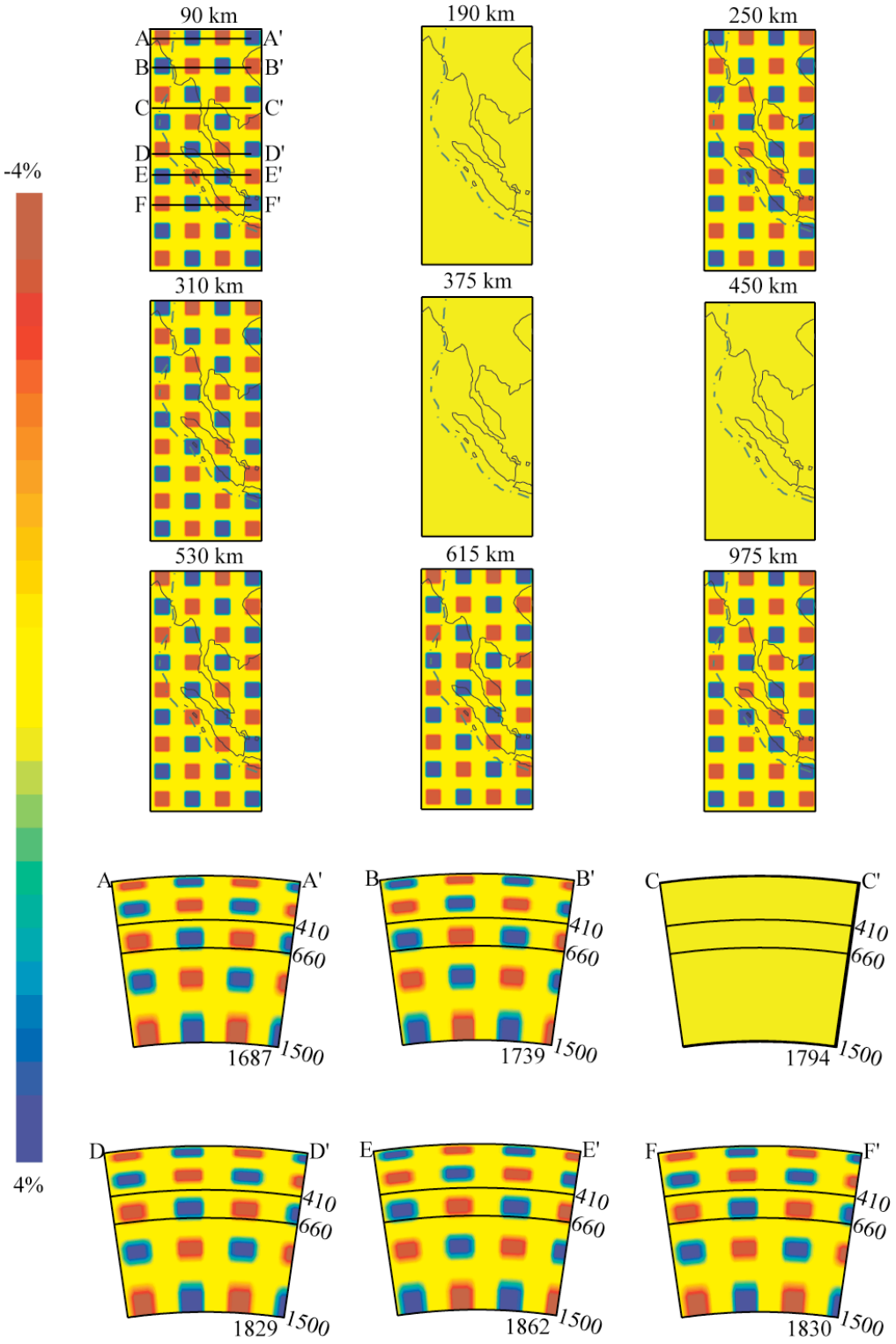

Figure 2.S3b. Alternate input model for synthetic checkerboard resolution tests. Checkerboard pattern is shifted two layers in depth. Layers that are blank (checkered) in Figure 2.S3a are now checkered (blank).

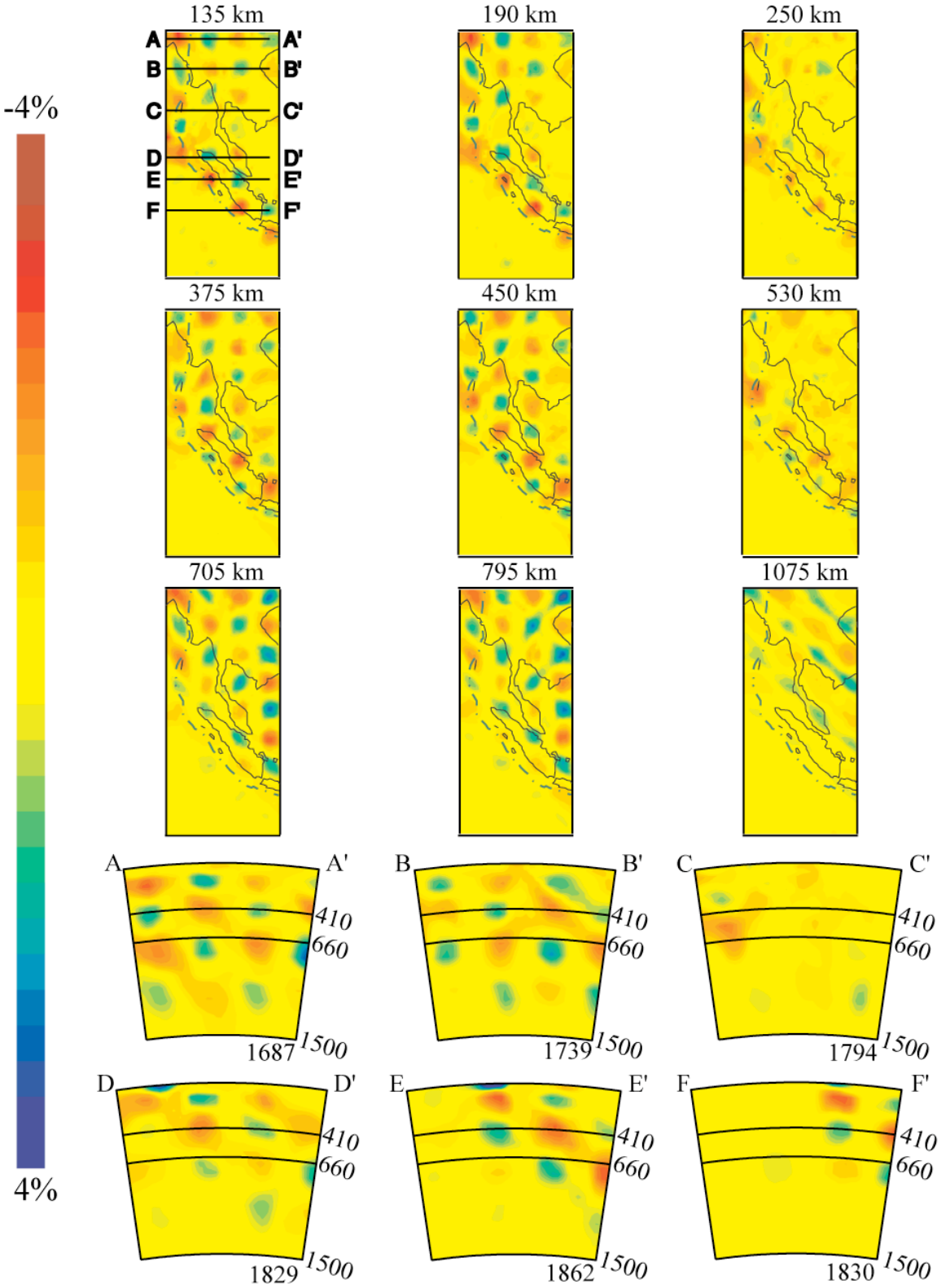

Figure 2.S4a. Checkerboard resolution test results for Figure 2.S3a.

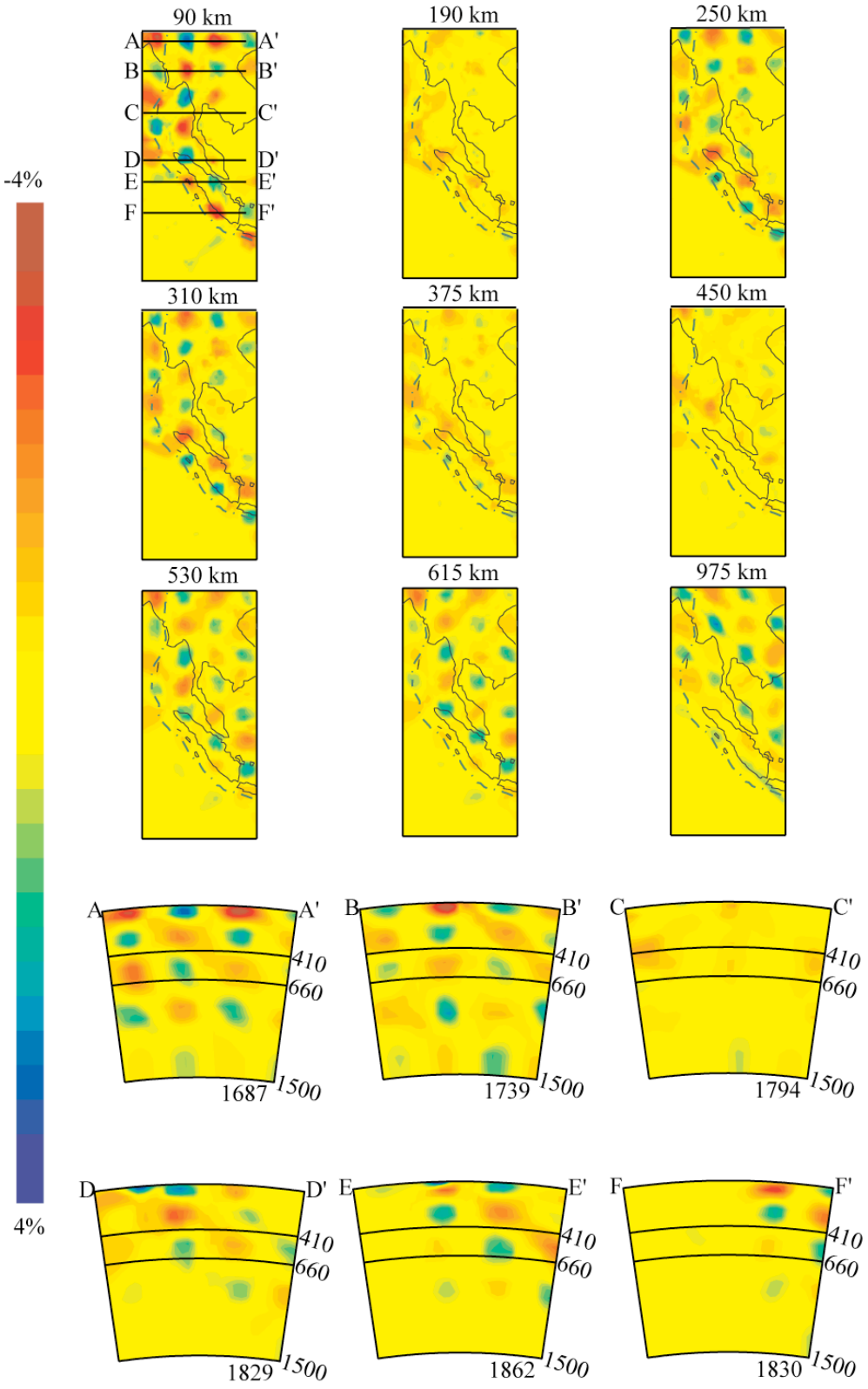

Figure 2.S4b. Checkerboard resolution test results for Figure 2.S3b.

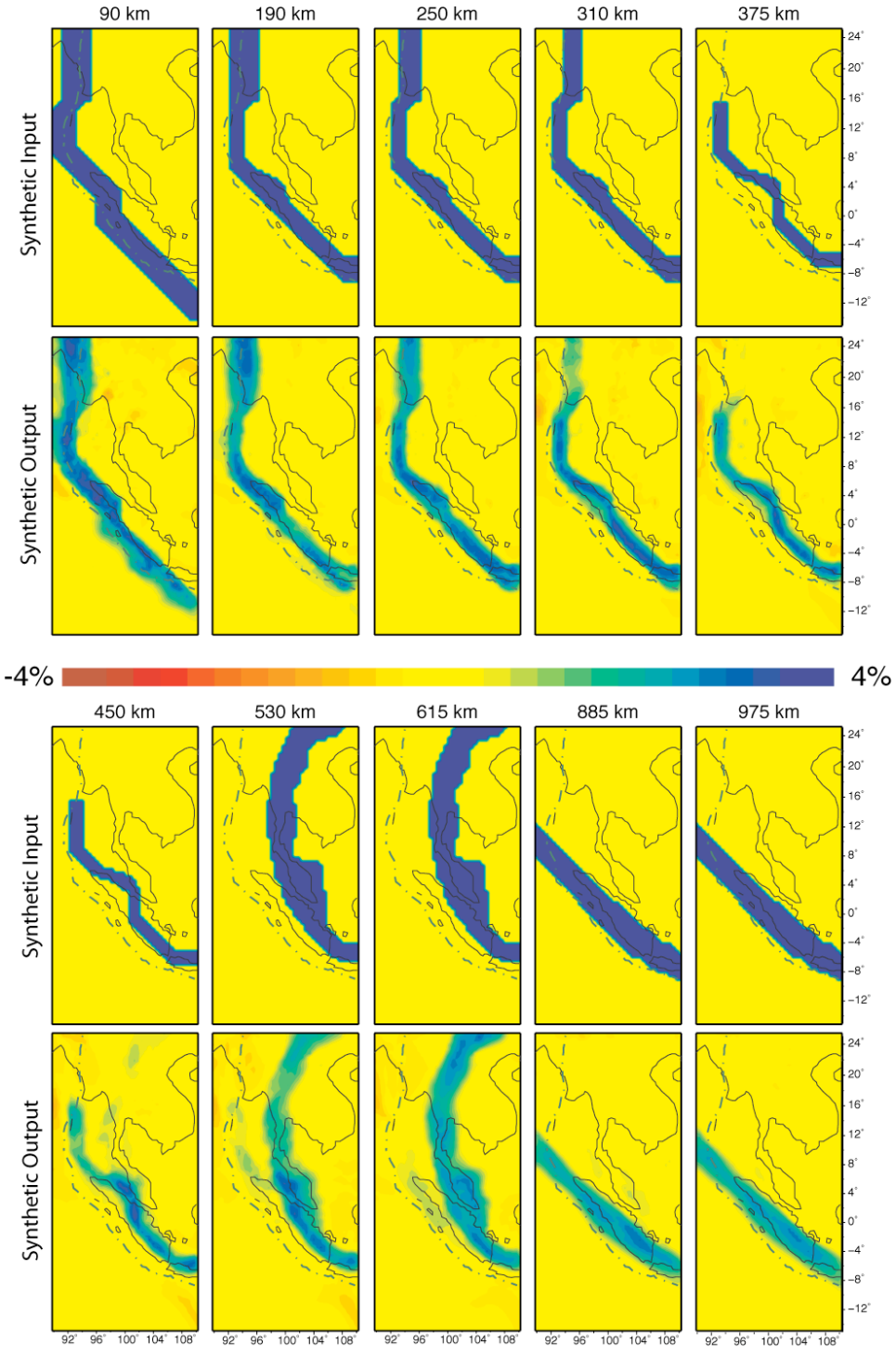

Figure 2.S5. Synthetic slab input model shown for the same layers as shown in Figure 2.3. One second of random noise is added to the residuals between the predicted travel times and those calculated through this input model. The 4% anomaly input model was designed to mimic actual structures interpreted from the real model.

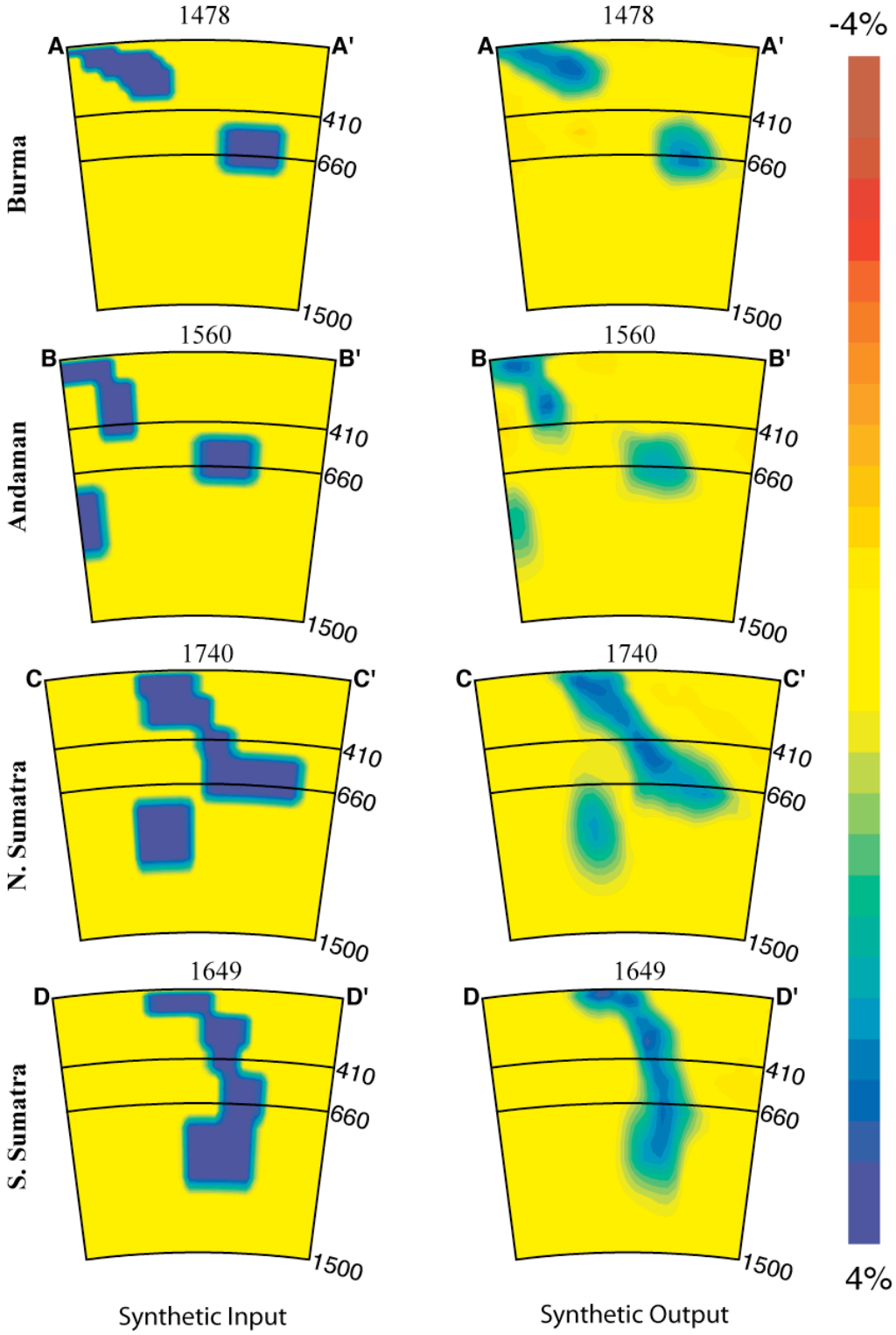

Figure 2.S6. Synthetic slab resolution test results indicate that the interpreted structures discussed in the text can be resolved by our inversion. Cross-section locations are the same as Figure 2.2, and are shown in Figure 2.1.

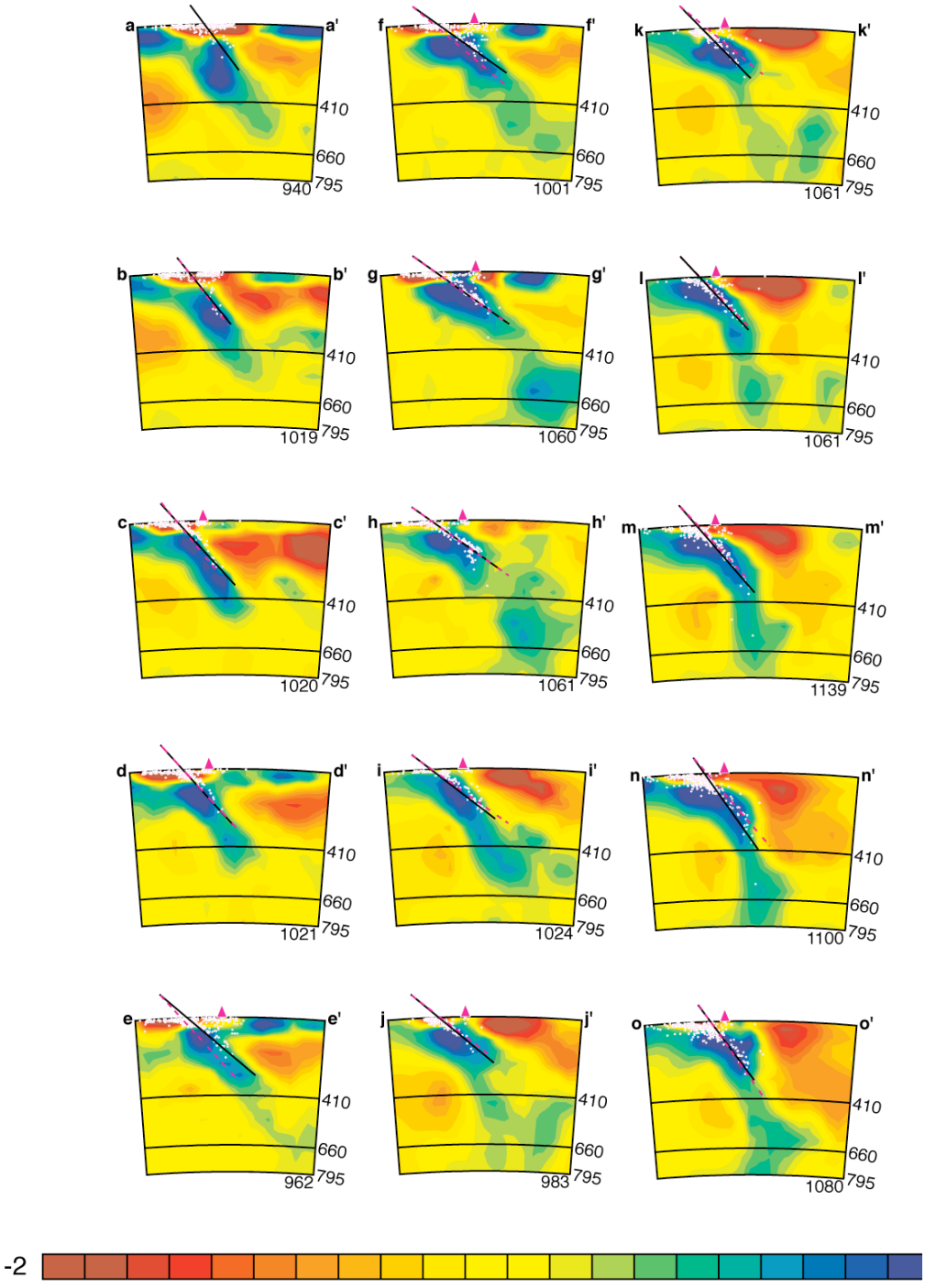

Figure 2.S7a. Cross-sections (locations shown in Figure 2.S7b) illustrating the change in dip of EHB seismicity and P-wave velocity anomaly associated with the folded slab below Sumatra. Black lines are the interpreted dip of the slab. Magenta dashed lines show the dip of the previous cross-section, superimposed to show the change in dip between cross-sections. Significant changes are observed at e-e' and k-k' and shallower dips are observed across the fold (sections e-k).

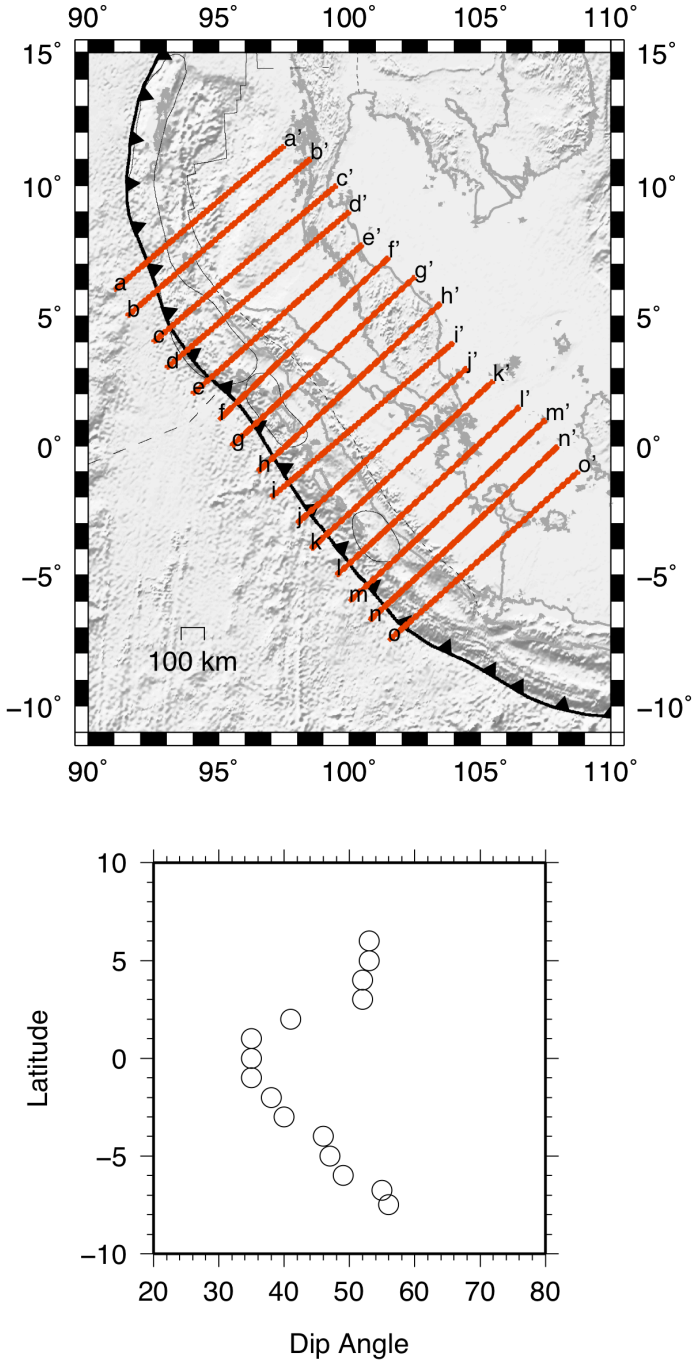

Figure 2.S7b. Cross-section locations for Figure 2.S7a (top) and plot of change in dip with latitude of the cross-section (bottom). Latitudes at the beginning of each section are plotted versus dip angles for the corresponding cross-section measured from the black lines in Figure 2.S7a.

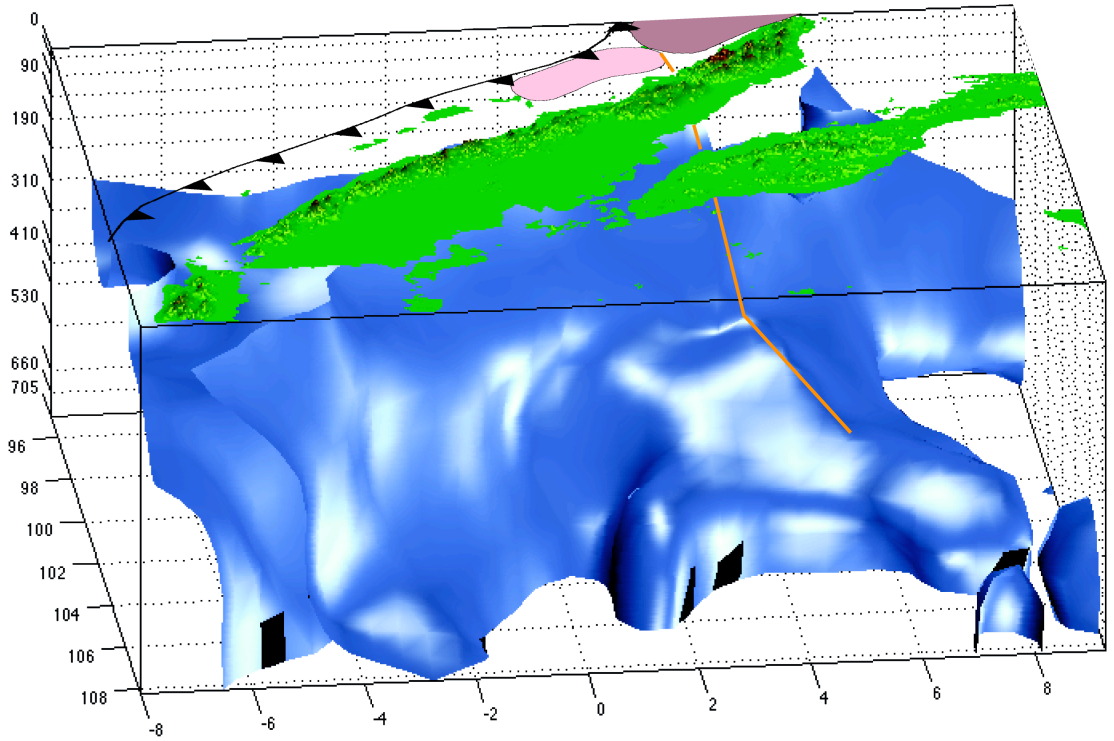

Figure 2.S8. 3-D smoothed iso-surface plot for +0.85% perturbation relative to ak135 [*Kennett et al.,* 1995] illustrating the slab fold beneath northern Sumatra. Our inferred fold axis is shown as an orange line, projected to the surface, where it approximately locates between the rupture areas of the 2004 (magenta) and 2005 (pink) megathrusts and corresponds to the area where the trench bends significantly. At depth, the fold deflects laterally as it encounters the transition zone, as shown by the kink in the orange axis line. Vertically exaggerated topography is also shown.

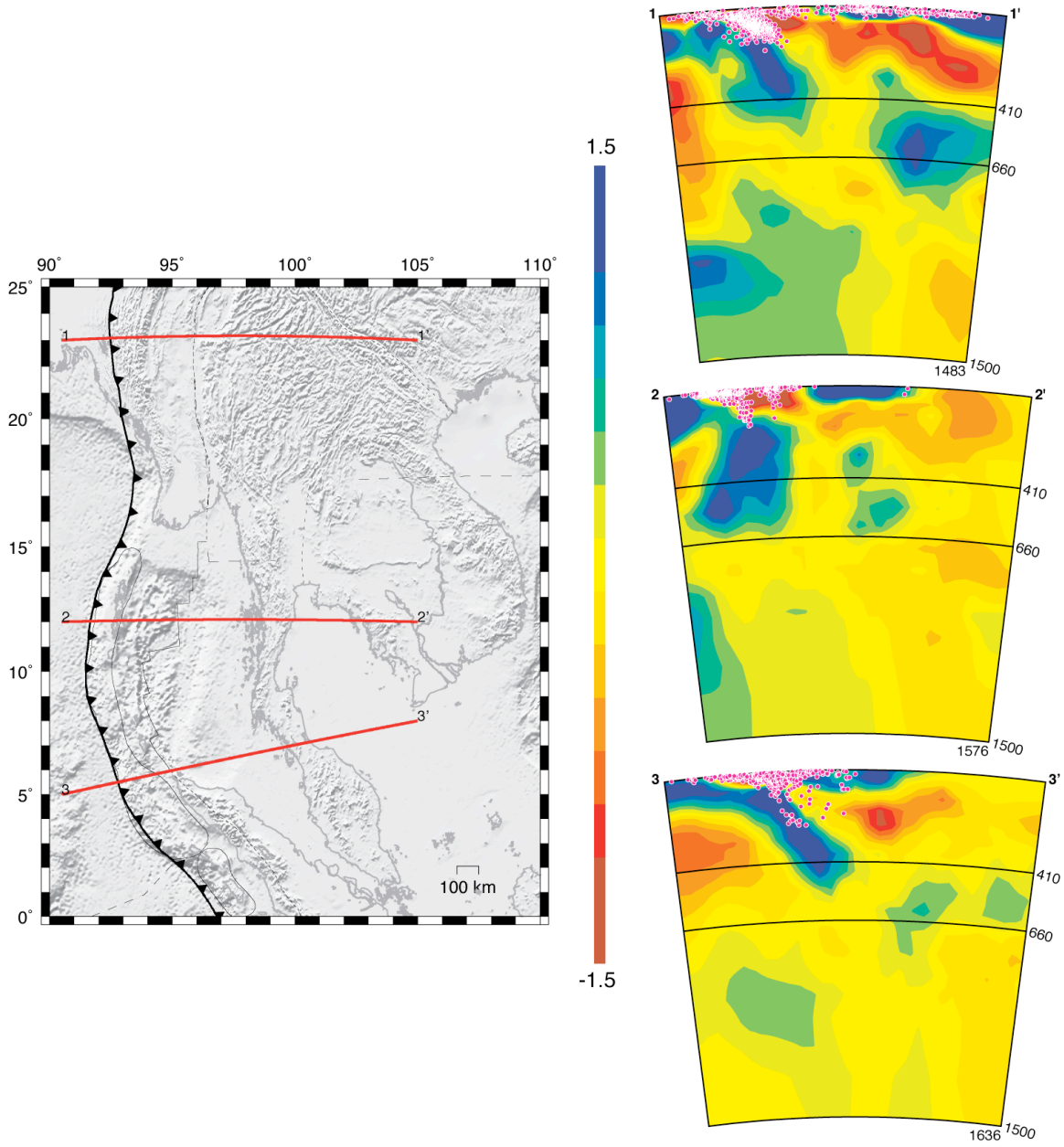

Figure 2.S9. Cross-sections showing clear separation between upper mantle and transition zone fast anomalies (cf. Figure 2.2a), suggesting the presence of a slab tear as discussed in text.

CHAPTER 3: Sharpening the Tomographic Image of the Subducting Slab below Sumatra, the Andaman Islands, and Burma

J.D. Pesicek, C.H. Thurber, S. Widiyantoro, H. Zhang, H.R. DeShon, and E.R. Engdahl

Abstract

Taking advantage of the increased ray coverage due to seismicity following the December 2004 and March 2005 great earthquakes, an improved iterative regional-global tomographic method was applied to the Sumatra-Andaman and adjacent regions to better constrain the 3-D mantle velocity heterogeneity in the region. Velocity and hypocentral parameters were iteratively perturbed to sharpen the image of the subducted slab. Several iterations were performed, and the effects of source mislocation were considered in the iterative process, an issue commonly neglected in teleseismic tomography. We find that source relocation between iterations increases the amplitudes of slab anomalies and sharpens the definition of slab geometry beyond what can be achieved by a fixed-source iterative inversion alone. In addition, extensive restoration tests of synthetic data were conducted that emphasize improvements obtained by our iterative process. These tests show significant increases in amplitude and decreased smearing of synthetic slab features. Thus, when applied to the real data, similar improvements are inferred in the

resulting model, which better illustrates the complex slab geometry in the upper mantle and transition zone regions along the Sumatra, Andaman, and Burma subduction zones.

3.1 Introduction

The 2004-2005 Sumatra-Andaman great earthquake sequences have provided a wealth of new seismic data from the region. These data have allowed us to obtain a detailed view of the complex structure of the subducting slab below Sumatra and the adjacent regions [*Pesicek et al.,* 2008]. In this paper, we present a sharpened tomographic image of the slab obtained from an improved iterative technique employing full three-dimensional (3-D) ray tracing, following the basic approach of Widiyantoro et al. [2000]. We have made several improvements to this methodology and have tested the solution extensively through restoration tests on synthetic data. In addition, we have included event relocation in the iterative procedure, an issue commonly neglected in teleseismic tomography. Below, we discuss our methodology improvements and their effects on our model for the *P*-wave velocity structure of the western Indochina subduction zones along the Sumatra and Andaman Islands, and Burma. In addition to an overall increase in slab amplitudes, our iterative solution shows higher amplitude fast anomalies in many areas that previously showed little or no velocity perturbation. Below Burma, our new higher resolution iterative model reveals that the subducting slab there, which had previously been interpreted as torn, may in fact be continuous.

3.2 Data

The data used in this study are travel times and earthquake locations reprocessed from global catalogs by the Engdahl, van der Hilst, and Buland (EHB) method of single

event relocation [*Engdahl et al.,* 1998]. The EHB catalog of data is commonly used in global and teleseismic tomography studies and is regarded as the most accurate global earthquake catalog available. In the Sumatra region, these data have been further groomed to provide more accurate depths [*Engdahl et al.,* 2007]. For those data for which waveforms are publicly available, more precise arrival times have been determined by cross-correlation techniques [*DeShon et al.,* 2007a].

We used global EHB data from 1964-2006 and regional Indonesian EHB data from 1964-2007 (Figure 3.1). We have also included data from a PASSCAL deployment in 1995 around Toba Caldera [*Fauzi et al.,* 1996; *Masturyono et al.,* 2001] to increase upper mantle sampling in this region. The combined available dataset is larger than that used by Pesicek et al. [2008]; however in this study we applied more stringent selection criteria. Specifically, we required a secondary azimuthal gap <180° and we only used events with sufficient depth control (e.g. located using later arriving phases in addition to first arrivals). This has resulted in fewer data but of higher quality being used in the inversion. The combined dataset consists of 957,262 compressional phases from events within the Indonesia region, including 10,640 *pP* and 4,239 *pwP* phases.

3.3 Methodology

Following Widiyantoro and van der Hilst [1997] and Widiyantoro et al. [2000], we set up the following system of tomographic equations

$$\begin{bmatrix} A_i \\ \alpha_i I_i \\ \gamma_i G_i \end{bmatrix} x_i = \begin{bmatrix} \delta t_i \\ -\alpha_{i-1} I_{i-1} x_{i-1} \\ 0 \end{bmatrix} \tag{3.1}$$

where for the *i*th iteration, x_i is the solution vector, A_i is the sensitivity matrix comprised of ray segment lengths in each model cell (regional and global) and event relocation derivatives and δt_i is the data vector of travel time residuals. Norm damping is applied through the identity matrix I (weighted by α) and biased toward the model used for ray tracing (x_{i-1}). Gradient smoothing (G_i) is also applied and weighted by γ. For $i > 1$, we modified (3.1) slightly to downweight the importance of large residual outliers using a technique known as iteratively reweighted least squares (IRLS), which approximates the 1-norm solution [*Scales et al.,* 1988; *Aster et al.,* 2005]. In applying IRLS, we also avoided the need for a residual cutoff threshold, a subjective choice common in linear tomographic inversions. We further modified (3.1) by adding a term that independently damps the crustal layer. The system of equations then becomes

$$\begin{bmatrix} W_i A_i \\ \alpha_i I_i \\ \gamma_i G_i \\ \beta_i I_i^c A_i^c \end{bmatrix} x_i = \begin{bmatrix} W_i \delta t_i \\ -\alpha_{i-1} I_{i-1} x_{i-1} \\ 0 \\ -\beta_{i-1} I_{i-1}^c x_{i-1}^c \end{bmatrix} \tag{3.2}$$

where W_i is a diagonal matrix with elements

$$W_i^k = \left(1 + \left(\frac{\delta t_{i-1}^k}{5} \right)^2 \right)^{-1} \qquad \text{for } \delta t_{i-1} > 1 \text{ ,} \tag{3.3}$$

β is the crustal damping coefficient and the superscript *c* denotes the crustal portion (0-35 km depth; Table 3.1) of the regional model. After choosing appropriate values for α, γ,

and β (discussed in detail below), we used the conjugate gradient least squares algorithm *LSQR* [*Paige and Saunders,* 1982] to solve (3.2) jointly for perturbations to the slowness of each model cell and to the hypocentral parameters.

Previous studies have damped the relocation perturbations heavily [e.g. *Widiyantoro and van der Hilst,* 1997; *Widiyantoro et al.,* 2000] or removed them from the inversion completely [*Weidle et al.,* 2005], fixing the event locations for each iteration. The arguments for neglecting or removing them are based on an analysis by Bijwaard and Spakman [2000] who found the relocation terms to be of little value for global tomography conducted with composite rays, event clusters, and large cell sizes. However, it has been demonstrated for local earthquake tomography (LET) that solving jointly for hypocenter and velocity perturbations is necessary to assure convergence [*Thurber,* 1992]. The coupled nature of the hypocenter-velocity structure problem argues for joint determination of these parameters. Furthermore, for our finely gridded regional model, the use of event clusters and composite rays is an unnecessary restriction that may limit our resolution. Tracing rays for each event allows for a more detailed investigation of the effects of source mislocation on teleseismic velocity determination. Accordingly, we included relocation perturbations in (3.2) for each event in the study region and have given them equal weight relative to the slowness perturbations. However, rather than applying them directly, we prefer to iteratively relocate events between tomography iterations, using a more precise double-difference technique (discussed below) [*DeShon et al.,* 2007b]. This approach is quite common in LET [e.g. *Thurber,* 1983].

3.3.1 Ray Tracing

We employed the pseudo-bending 3-D ray tracing method of Um and Thurber [1987] extended to spherical coordinates by Koketsu and Sekine [1998]. In the Indonesia region, we initially traced rays from stations to sources through the global spherically symmetric model *ak135* [*Kennett et al.,* 1995]. However, we replaced the shallowest layer with velocity values from the global crustal model CRUST 2.0 [*Bassin et al.,* 2000], converted to perturbations relative to *ak135*, and interpolated to fit our parameterization (0.5° x 0.5°; Table 3.1). Within the regional model, *pP* and *pwP* (corrected for water travel time) are traced to initial bounce points provided in the EHB catalog, and the bounce points are iteratively perturbed until the angle between the upgoing and downgoing ray segments are equivalent [*Zhao and Lei,* 2004]. Rays to bounce points and stations are traced to their true surface elevations in the newly modified crustal layer.

Within the coarser global model (5° x 5°), we traced rays through the global P-wave model *MITP08* [*Li et al.,* 2008]. Although the nested regional-global tomographic method we employed allowed us to solve for a coarse global P-wave velocity model in addition to finer regional structure in the Indonesia region, global velocity structure was not the focus of our study. The *MITP08* model was produced using several additional phases (*PKP, P_{diff}, PP*) and is thus likely better constrained. We interpolated the *MITP08* model to fit our global parameterization and applied twice as much damping and smoothing to the global solution as to the regional solution in our inversion.

3.3.2 Regularization

Our system of equations (3.2) includes 3 explicit and 2 implicit regularization coefficients (RCs). Minimum norm damping (α) and gradient smoothing (γ) operators were applied independently to both the regional and global models, and an additional damping term (β) was added to penalize changes to the *a priori* crustal model. We have tested these values extensively, first to determine the range of acceptable values and then to choose a preferred value. However, the choice of RCs remains subjective. Thus, we only interpret large-scale features that are evident regardless of the choice of RCs (within the acceptable range).

3.3.2.1 Crustal correction

The biased distribution of receivers in the study region (i.e. only on islands), the near vertical incidence angles of teleseisms at the surface, and the uneven distribution of large magnitude shallow events severely limits ray coverage at crustal depths, which in turn limits resolution in the top model layer. However, the presence of strong crustal heterogeneities relative to the reference model may cause smearing of crustal anomalies to greater depths [e.g. *Li et al.,* 2006]. In the Sumatra region, oceanic crustal velocities are faster than the global average, which led to a strong positive crustal anomaly in the Pesicek et al. [2008] model. To minimize smearing of crustal anomalies, we replaced the crustal layer with an *a priori* crustal model [*Bassin et al.,* 2000] and added the crustal correction term in (3.2). We tested a range of values for β and chose a value that

minimized most crustal perturbations, yet allowed the model to change in regions where sufficient ray coverage exists (Figure 3.2).

3.3.2.2 Restoration Tests

The most common way of choosing RCs in teleseismic tomography is by conducting restoration (a.k.a resolution or sensitivity) tests with synthetic data. This process involves 1) calculating travel times through synthetic velocity models with known anomalies, 2) forming travel time residuals relative to the reference model, 3) adding noise to the residuals, and 4) inverting these residuals, usually using a parameterization identical to the actual inversion. The degree to which the synthetic model anomalies are restored is then used to judge the resolution of the real inversion. Due to noise in the real data, RCs are required, and their values are typically chosen in order to best restore the shape and amplitude of the known anomalies.

Toward this end, we have conducted restoration tests using two checkerboard models (Figure 3.3) to assess the spatial resolution of the data and a synthetic subducting slab model (Figure 3.4) that attempts to mimic the shape of the slab imaged with the real data. We traced rays through these synthetic models and calculated residuals relative to *ak135* [*Kennett et al.,* 1995]. We then added noise to the residuals and repeated our actual iterative procedure. Typically, Gaussian errors are added for global tomography restoration tests [e.g. *Spakman and Nolet,* 1988]. However, it is well known that travel time residual distributions are not well matched by Gaussian functions due to outliers

with large residuals [e.g. *Buland,* 1986]. To simulate a more realistic distribution of noise, we randomized the actual residuals from the real inversion and added them to the synthetic residuals (Figure 3.5). When we compared the results of our synthetic slab model (Figure 3.4) using this strategy to results of a case where a Gaussian noise distribution (variance = 2.25 s^2) was added, and to results where no noise was added, we found that the addition of noise has little effect on the recovery of the large scale slab geometry [see also *Widiyantoro et al.,* 2000].

The results of the restoration tests demonstrate that our iterative procedure increases amplitude recovery of the synthetic anomalies significantly while reducing smearing and suppressing noise. Figures 3.6 and 3.7 show the improvements to the model from iteration 1 to iteration 2 (col. C) but also illustrate the limitations of our resolution (col. D), despite these improvements. For smaller features like the checkers (2.5°), improvement to recovery of any one checker is modest (Figure 3.6a, col. C; Figure 3.7a). However, good restoration of the anomaly pattern is achieved east of the subduction boundary in most areas, although amplitude recovery of slow checkers is smaller compared to fast ones. More importantly for our purposes, recovery of the large, fast slab is quite good (Figure 3.6b, col. B) and much improved relative to iteration 1 (Figure 3.6b, col C; Figure 3.7b). In fact, complete amplitude restoration of the synthetic slab is achieved in many areas (Figure 3.6b, col. D).

3.3.2.3 Trade Off Analysis

Choosing the right RCs involves a tradeoff between minimizing data misfit versus minimizing model perturbations (and roughness). Eberhart-Phillips [1986] introduced the so-called "trade-off curve" (TOC) to determine optimal RCs and it has commonly been used since in LET studies. However, we are unaware of any teleseismic study that has used TOCs to determine RCs. Checkerboard tests appear to be the standard.

We have examined the tradeoff between model size and data misfit for our regional RCs at several iterations. We found that the RCs that performed best in the restoration tests described above (i.e., by better restoring the shape and amplitude of the synthetic anomalies) are lower than the optimal values determined by our trade off analyses (Figure 3.8). Our analysis showed that the optimal RCs determined by synthetics alone give a *LSQR* solution that appears underdamped when applied to the real data; the resulting model seems oscillatory and noisy. This suggests to us that we are not adequately representing the population of noise in the data in our synthetic tests.

Recently, Koulakov [2009] questioned the validity of TOCs for LET, and used synthetic tests similar to ours to suggest that RCs determined by TOCs are overestimated. In our results, the opposite is true: resolution tests underestimate the appropriate values of RCs and produce a model that is too noisy. The limitations of synthetic tests are well known [e.g. *Léveque et al.,* 1993]. They are useful for assessing the ability of the sensitivity matrix to recover specific features, but should not be used as the sole basis for determining RCs for the whole system. Instead, our strategy is to conduct trade-off analyses to determine the range of acceptable RCs, and then evaluate how these values

recover the synthetic anomalies. Using a combination of TOCs and synthetics tests to choose RCs is preferable because it bases the decision on the real data in addition to the synthetic data. We used this strategy at several iterations and found that the range of optimal RCs suggested by the corner region of the TOCs does not change significantly for subsequent iterations. Thus, we have chosen our RCs based on the first iteration, and have kept them fixed for all iterations.

3.3.3. Earthquake Relocation

In order to determine how source mislocation affects our solution, we have relocated the initial EHB earthquake locations using a modified double-difference (DD) technique. The original DD method [*Waldhauser and Ellsworth,* 2000] has proven effective at determining precise relative local and regional earthquake locations within many seismic networks [e.g. *Prejean et al.,* 2002; *Schaff et al.,* 2002]. When adapted to determine velocity structure and absolute event locations in addition to relative locations [*Zhang and Thurber,* 2003], the DD method has provided high-resolution tomographic images and high-precision event locations at a variety of scales and in a variety of tectonic settings [*Zhang and Thurber,* 2006]. More recently, the DD method (using a 1-D model) has proven effective at teleseismic event relocation as well [*Waldhauser and Schaff,* 2007].

The DD tomography algorithm *tomoDD* of Zhang and Thurber [2003] has been extended to teleseismic distances [*DeShon et al.,* 2007b]. However, currently velocity

determination in the algorithm is limited to source regions where differential times are available. In this study we use the teleseismic version of *tomoDD*, (named *teletomoDD*) solely to relocate events in western Indochina using our 3-D model (iteration 2) and update the hypocentral parameters between subsequent velocity inversion iterations. We limit our discussion to the effects that event relocation have on our improved tomographic model. An analysis of the relocations is presented in Chapter 4.

3.4 Results & Discussion

3.4.1 Model Improvements with Fixed Sources

Iterative teleseismic tomography studies commonly neglect or ignore source mislocation for a variety of reasons [see *Bijwaard and Spakman,* 2000]. In Figure 3.9, we present our model at various depths for several iterations. In Figure 3.10, we present the differences between model iterations to illustrate the improvements due to the iterative process alone (Col. A and B). Our second iteration model shows a 3.4% misfit reduction (Table 3.2), comparable to reductions found for similar nonlinear studies without source relocation [*Widiyantoro et al.,* 2000; *Weidle et al.,* 2005]. The overall anomaly patterns are generally consistent with the first iteration model, also a conclusion of previous studies. Most of the observed changes are a result of increasing amplitudes at the centers of slab anomalies, although increases in the magnitude of negative mantle wedge anomalies are also common (Figure 3.10b). These changes are largest in the upper mantle and decrease with depth. Additional iterations with fixed sources were performed (e.g.

Figure 3.9, Col. B) and the resulting model changes were similar in pattern but decreased in magnitude (Figure 3.10, Col. B) with each subsequent iteration (Table 3.2).

3.4.2 The Effects of Source Relocation on Iteration

Relocation of sources between iterations is commonplace in LET studies, but quite uncommon in teleseismic tomography. Although hypocentral derivatives are usually included in nonlinear teleseismic inversions, they are often subjectively scaled either to damp the resulting perturbations [*Widiyantoro et al.,* 2000], or to give them expected magnitudes [*Bijwaard et al.,* 1998; *Bijwaard and Spakman*, 2000; *Amaru*, 2007]. Our experience with the hypocentral perturbations that result from the joint solution is that they are still erroneously small even when their derivatives are equally scaled or upweighted relative to the velocity terms. This is likely due to *LSQR* being unable to correctly determine the small singular values associated with the relocation terms. Thus, rather than subjectively scaling the relocation derivatives for use in the next iteration, we relocate the earthquakes independently using *teletomoDD*, which can iteratively determine accurate locations in the current velocity model. We note that Amaru [2007] also upweighted the relocation terms in the joint solution, but then relocated events using a separate grid search method. She found that velocity contrasts are enhanced across subduction zones when events were relocated in this way using a global 3-D model prior to inversion.

Figures 3.9 and 3.10 (Col. C and D) illustrate the improvements to our model (IT3r) due the DD relocation of sources using the previous iteration model (IT2). From these results, it is clear that source relocation through our 3-D model prior to further iteration is warranted. Significant changes in the amplitudes of the slab anomalies are seen in most layers of the model following source relocation. At upper mantle depths, amplitudes of the slab and mantle wedge increase, much more so than for iteration 2 (Figure 3.10, Col. C). Negative amplitude changes are likely a combination of focusing of the slab (decreased smearing of the slab, as seen in Figures 3.6, 3.7) and increased slow amplitudes in the mantle wedge.

Comparison of the data misfit for iterations with and without source relocation shows slight misfit increases (<2%) for those iterations with DD source relocation (cf. IT3 and IT3r; Table 3.2). However, this is not unexpected given that the input source data for the inversion have now changed. Models for iterations with source relocation (IT3r-IT5r) are being fit to a more accurate but different dataset. Our final model (IT5r) still has a slightly higher misfit than the model with the same number of iterations without source relocation (IT5). However, the misfit for the IT5 model was achieved from 5 iterations of the same EHB source data whereas our final model (IT5r) was achieved from only 3 iterations with the DD source data. Similarly, we expect that relocation through the IT5r model would cause another slight increase in misfit as the solution adjusts to the different data. This effect is often observed in nonlinear LET where data and/or data weighting are dynamically changed throughout the iterative process as the solution converges to the most accurate model with the most accurate

locations. Overall, the differences in misfit and model amplitudes for EHB versus DD source iterations are minor (Table 3.2), but the upper mantle slab anomalies are significantly enhanced when source relocation is included (e.g. Figure 3.10, Col. C and D). This misfit mismatch can only be resolved when the 3-D DD joint inversion can be applied to the full dataset, something that is not currently possible due to computational limitations.

3.4.3 Lithospheric Slab Folding below Sumatra

The final model resulting from our iterative method (Figure 3.11) provides an improved view of the subducting slab below the western Indochina subduction zones. The image of the lithospheric slab fold subducting below northern Sumatra presented in Chapter 2 is now more focused, but its origin remains subject to debate. The complexity of the regional tectonics makes it difficult to attribute the fold to any one feature or process. Subduction of the Investigator Fracture Zone (IFZ), the Wharton Fossil Ridge (WFR), and the diffuse deformational boundary between the Indian and Australian plates all occur in this region (Figure 3.1), any of which may influence this folding. Alternatively, the possibility that the fold is static and due only to trench curvature [*Fauzi et al.,* 1996] cannot be ruled out.

If we assume that the fold below Sumatra is a primary feature of the incoming plate, then the long-wavelength buckling or folding (100-300 km) of the Indian Ocean lithosphere that has been discussed by many authors [e.g. *Deplus et al.*,1998; *Deplus,*

2001; *Krishna et al.,* 2001] may be pertinent. These folds have been inferred from gravity undulations and seismic reflection data throughout the Central Indian and Wharton basins. The orientations of their axes are perpendicular to regional compression axes and they are interpreted as being caused by internal deformation of the Indian and Australian plates. Southwest of Sumatra, their axes are oriented NE-SW, parallel to the orientation of the axis of our imaged fold. Although similar in shape, orientation, and possibly causal mechanism, they cannot be *directly* related to the lithospheric fold below Sumatra due to the timing of their formation. The onset of diffuse deformation between the Indian and Australian plates that caused this buckling is thought to have begun at ~8 Ma [*Krishna et al.,* 2001], much more recently than the inferred timing of subduction of the folded slab (~17 Ma) that we have imaged well into the transition zone (Figure 3.11).

A more likely scenario is one that attributes the fold to extinction of the Wharton spreading ridge and subsequent compression of the WFR much earlier than 8 Ma. Subduction of the Wharton spreading ridge is thought to have formed a slab window beneath southern and central Sumatra at 45-35 Ma [*Whittaker et al.,* 2007]. Extinction of spreading at ~45 Ma [*Deplus et al.,* 1998] and the switch from an extensional to a compressional stress regime at ~35 Ma [*Whittaker et al.,* 2007] could have driven the change from slab window formation to slab fold formation along the thinned axis of the WFR. This timeline agrees with the longevity of the fold implied by our tomography results.

Although the mechanism for slab folding beneath northern Sumatra is as of yet unexplained, the existence of slab folding here is not unique. The Cascadia subduction

zone also shows broad slab curvature at depths up to ~100 km [*McCrory et al.,* 2006]. Here, bending of the Juan de Fuca plate as it subducts is thought to be due to solely to trench curvature [*Crosson and Owens,* 1987]. Similar changes in the slab strike are also observed beneath southern Central America and have been related to age differences (5-10 m.y.) between the subducting Cocos and Nazca plates, which are juxtaposed but separated by a relic fracture feature [*Protti et al.,* 1994]. This region may be analogous to either side of the folded slab beneath Sumatra, where similar age differences occur across the WFR [*Whittaker et al.,* 2007].

A final comparison comes from subduction beneath Japan, where the Japan and Izu-Bonin slabs differ in orientation, but meet to form a "cusp-like junction" in the upper mantle [*Obayashi et al.,* 2009]. Bending of these two slabs at their junction has been imaged throughout the upper mantle. Upon entry into the transition zone, the slabs tear apart as they flatten. This scenario may be correlative to northern Sumatra where our IT5r results show a gap in the slab anomalies along the fold axis at similar depths (Figure 3.11a; 450-530 km depth). Additionally, the slab fold beneath Sumatra may also be thought of as a junction (albeit diffuse) between two plates, the Indian and Australian plates.

3.4.4 A Tear in the Slab below Burma?

Pesicek et al. [2008] proposed a subhorizontal tear in the subducting slab below Burma at 340-490 km depth (Figure 2.2). The proposed tear was suggested to have

originated north of Burma and propagated southward toward Sumatra, where slab continuity was observed down through the transition zone. Our new model shows a significant increase in the amplitude of the slab anomalies below Indochina (Figure 3.11), further illuminating slab geometry here and calling into question the presence of a slab tear below Burma. Figure 3.11b shows a relatively continuous slab below Burma along the 21°N cross-section (A'), in contrast to the discontinuous slab in the same cross-section presented by Pesicek et al. [2008]. However, Figure 3.12 shows a discontinuous slab directly north of 21°N (along the 22°N, 23°N, and 24°N cross-sections) but a continuous slab again at 20°N. Results for our restoration tests of torn and continuous slabs below Burma (Figure 3.13) are ambiguous; recovery is diminished above the 440 km discontinuity (at ~300 km depth) (Figure 3.13a) but smearing of distinct anomalies (Figure 3.13b), which might also hinder discerning slab continuity, may connect torn slab segments if they are closely spaced. Thus, a localized slab tear or window, or a significantly thinned slab, below Burma may exist, but these slab gaps may also be resolution artifacts. If a slab tear does exist below Burma, it is most likely not extensive or continuous into the Andaman arc.

Images of the slab below Burma from independent tomographic studies differ considerably. Li et al. [2008] discuss subduction below Burma in their tomographic study of the Tibet and Burma regions. Cross-sections through their model, which lie at the edge and to the north of our 25°N model boundary, show no clear evidence of a tear below Burma. Although broad fast anomalies in this region at transition zone depths exist in their model, Li et al. [2008] suggest that these anomalies may actually be related

to subduction along a different arc, such as the late Mesozoic South China Trench [*Honza and Fujioka,* 2004]. In contrast, Huang and Zhao [2006] show good separation between the upper mantle slab below Burma and fast transition zone material along their 25°N cross-section, in agreement with our results. The latter anomaly is juxtaposed to the east by a large low velocity region, making it difficult to attribute this remnant slab to subduction from the east. Neither of these models extends far enough to the south to show the southward continuation of these transition zone anomalies into our study region and can neither confirm nor contradict our results. From our images, a completely continuous slab throughout the region is unlikely but the exact geometry of the slab below Burma remains unclear.

3.5 Summary & Conclusions

We have presented an improved *P*-wave velocity model of the Sumatra, Andaman, and Burma subduction zones (Figure 3.11) based on the nonlinear nested regional-global method of Widiyantoro et al. [2000]. We have added residual reweighting and source relocation to the iterative scheme, two processes common in LET studies but hitherto not commonly applied in teleseismic tomography studies. We have examined in detail the model improvements obtained by conducting additional iterations with and without source relocation. Although the majority of the resolved velocity structure is recovered after one iteration, significant increases in slab amplitude and slab sharpening occur in some regions of the upper mantle from subsequent iterations, particularly after source relocation. Source relocation through the 3-D model prior to

additional velocity iterations substantially focuses the image of the subducting slab in the study region, beyond what is achieved by fixed source iteration alone. Below Burma, improvements due to our iterative technique extend slab anomalies beyond the boundaries of single iteration results, revising interpretations of slab geometry. Thus, source relocation may be an important contributor to increasing accuracy of teleseismic tomography models, which in turn may help clarify interpretations of previously identified mantle structures or facilitate discovery of new ones.

References

Amaru, M. L. (2007), Global travel time tomography with 3-D reference models, PhD thesis, Utrecht University.

Aster, R. C., B. Borchers, and C. H. Thurber (2005), *Parameter Estimation and Inverse Problems*, Academic Press.

Bassin, C., G. Laske, and G. Masters (2000), The current limits of resolution for surface wave tomography in North America, *Eos Trans AGU, 81*, F897.

Bijwaard, H. and W. Spakman (2000), Non-linear global P-wave tomography by iterated linearized inversion, *Geophys.J.Int., 141*, 71-82.

Bijwaard, H., W. Spakman, and E. R. Engdahl (1998), Closing the gap between regional and global travel time tomography, *J. Geophys. Res.*, 103, 30,055-30,078.

Buland, R. (1986), Uniform reduction error analysis, *Bull. Seismol. Soc. Am., 76*, 217-230.

Crosson, R. S. and T. J. Owens (1987), Slab geometry of the Cascadia subduction zone beneath Washington from earthquake hypocenters and teleseismic converted waves, *Geophys. Res. Lett., 14*, 824-827.

Deplus, C. (2001), Indian Ocean actively deforms, *Science, 292*, 1850-1851.

Deplus, C., M. Diament, H. Hebert, G. Bertrand, S. Dominguez, J. Dubois, J. Malod, P. Patriat, B. Pontoise, and J. Sibilla (1998), Direct evidence of active deformation in the eastern Indian oceanic plate, *Geology, 26*, 131-134.

DeShon, H. R., C. H. Thurber, M. R. Brudzinski, and E. R. Engdahl (2007a), A semi-automated technique for waveform cross-correlation of teleseismically recorded depth phases, *Seismol. Res. Lett., 78*.

DeShon, H. R., H. Zhang, C. H. Thurber, and E. Engdahl (2007b), Imaging the Andaman and Sunda Subduction Zones Using Regional Double-Difference Tomography, *Eos Trans AGU*, abstract# S23D-03.

Eberhart-Phillips, D. (1986), Three-dimensional velocity structure in northern California Coast Ranges from inversion of local earthquake arrival times, *Bull. Seismol. Soc. Am., 76*, 1025-1052.

Engdahl, E. R., van der Hilst, R. D., and R. Buland (1998), Global teleseismic earthquake relocation with improved travel times and procedures for depth determination, *Bull. Seismol. Soc. Am., 88*, 722-743.

Engdahl, E. R., A. Villasenor, H. R. DeShon, and C. H. Thurber (2007), Teleseismic relocation and assessment of seismicity (1918-2005) in the region of the 2004 Mw 9.0

Sumatra-Andaman and 2005 Mw 8.6 Nias Island great earthquakes, *Bull. Seismol. Soc. Am., 97*, S43-61.

Fauzi, R. McCaffrey, D. A. Wark, Sunaryo, and P. Y. Prih Haryadi (1996), Lateral variation in slab orientation beneath Toba Caldera, northern Sumatra, *Geophys. Res. Lett., 23*, 443-446.

Honza, E. and K. Fujioka (2004), Formation of arcs and backarc basins inferred from the tectonic evolution of Southeast Asia since the Late Cretaceous, *Tectonophysics, 384*, 23-53.

Huang, J. and D. Zhao (2006), High-resolution mantle tomography of China and surrounding regions, *J. Geophys. Res., 111*, B09305.

Kennett, B. L. N., E. R. Engdahl, and R. Buland (1995), Constraints on seismic velocities in the Earth from traveltimes, *Geophys. J. Int., 122*, 108-124.

Koketsu, K. and S. Sekine (1998), Pseudo-bending method for three-dimensional seismic ray tracing in a spherical earth with discontinuities, *Geophys. J. Int., 132*, 339-346.

Koulakov, I. (2009), LOTOS Code for local earthquake tomographic inversion: benchmarks for testing tomographic algorithms, *Bull. Seismol. Soc. Am., 99*, 194-214.

Krishna, K. S., J. M. Bull, and R. A. Scrutton (2001), Evidence for multiphase folding of the central Indian Ocean lithosphere, *Geology, 29*, 715-718.

Léveque, J., L. Rivera, and G. Wittlinger (1993), On the use of the checker-board test to assess the resolution of tomographic inversions, *Geophys. J. Int., 115*, 313-318.

Li, C., R. D. van der Hilst, E. R. Engdahl, and S. Burdick (2008), A new global model for P wave speed variations in Earth's mantle, *Geochem. Geophys. Geosyst., 9*, 1-21.

Li, C., R. D. van der Hilst, and M. N. Toksoz (2006), Constraining P-wave velocity variations in the upper mantle beneath southeast Asia, *Phys. Earth Planet. Inter., 154*, 180-195.

Li, C., R. D. van der Hilst, A. S. Meltzer, and E. R. Engdahl (2008), Subduction of the Indian lithosphere beneath the Tibetan Plateau and Burma, *Earth Planet. Sci. Lett., 274*, 157-168.

Masturyono, R. McCaffrey, D. A. Wark, S. W. Roecker, Fauzi, G. Ibrahim, and Sukhyar (2001), Distribution of magma beneath the Toba caldera complex, north Sumatra, Indonesia, constrainted by three-dimensional P wave velocities, seismicity, and gravity data, *Geochem. Geophys. Geosyst., 2, paper no. 2000GC000096*.

McCrory, P.A., J.L. Blair, D.H. Oppenheimer and S.R. Walter, Depth to the Juan De Fuca slab beneath the Cascadia subduction margin-A 3-D model for sorting earthquakes, *U.S. Geological Survey, Data Series 91, Version 1.2* (2006).

Obayashi, M., J. Yoshimitsu, and Y. Fukao (2009), Tearing of Stagnant Slab, *Science, 324*, 1173-1175.

Paige, C. and M. A. Saunders (1982), LSQR: An algorithm for sparse linear equations and least squares problems, *ACM Trans. Math. Soft., 8*, 43-71.

Pesicek, J. D., C. H. Thurber, S. Widiyantoro, E. R. Engdahl, and H. R. DeShon (2008), Complex slab subduction beneath northern Sumatra, *Geophys. Res. Lett., 35*, L20303.

Prejean, S. G., W. L. Ellsworth, M. D. Zoback, and F. Waldhauser (2002), Fault structure and kinematics of the Long Valley Caldera region, California, revealed by high-accuracy earthquake hypocenters and focal mechanism stress inversions, *J. Geophys. Res., 107*, 19 pp.

Protti, M., F. Guendel, and K. McNally (1994), The geometry of the Wadati-Benioff zone under southern Central America and its tectonic significance; results from a high-resolution local seismographic network; 10 years of GEOSCOPE-broadband seismology, *Phys. Earth Planet. Inter., 84*, 271-287.

Scales, J. A., A. Gerztenkorn, and S. Treitel (1988), Fast 1p solution of large, sparse, linear systems: Application to seismic travel time tomography, *J. Comput. Phys., 75*, 314-333.

Schaff, D. P., G. H. R. Bokelmann, G. C. Beroza, F. Waldhauser, and W. L. Ellsworth (2002), High-resolution image of Calaveras Fault seismicity, *J. Geophys. Res, 107*, 16 pp.

Spakman, W. and G. Nolet (1988), Imaging algorithms, accuracy and resolution in delay time tomography, in *Mathematical Geophysics; a Survey of Recent Developments in Seismology and Geodynamics*, edited by N. J. Vlaar, G. Nolet, M. J. R. Wortel, and S. A. P. L. Cloetingh, D. Reidel Publ. Co., Dordrecht, Netherlands (NLD), Netherlands (NLD).

Thurber, C. H. (1983), Earthquake locations and three-dimensional crustal structure in the Coyote Lake area, central California, *J. Geophys. Res., 88*, 8226–8236.

Thurber, C. H. (1992), Hypocenter-velocity structure coupling in local earthquake tomography, *Phys. Earth Planet. Inter., 75, 55-62*.

Um, J. and C. H. Thurber (1987), A fast algorithm for two-point seismic ray tracing, *Bull. Seismol. Soc. Am., 77*, 972-986.

Waldhauser, F. and W. L. Ellsworth (2000), A double-difference earthquake location algorithm; method and application to the northern Hayward Fault, California, *Bull. Seismol. Soc. Am., 90*, 1353-1368.

Waldhauser, F. and D. Schaff (2007), Regional and teleseismic double-difference earthquake relocation using waveform cross-correlation and global bulletin data, *J. Geophys. Res., 112, B12301*.

Weidle, C., S. Widiyantoro, and CALIXTO Working Group, International (III) (2005), Improving depth resolution of teleseismic tomography by simultaneous inversion of teleseismic and global P-wave traveltime data; application to the Vrancea region in Southwestern Europe, *Geophys. J. Int., 162*, 811-823.

Whittaker, J. M., R. D. Müller, M. Sdrolias, and C. Heine (2007), Sunda-Java trench kinematics, slab window formation and overriding plate deformation since the Cretaceous, *Earth Planet. Sci. Lett., 255*, 445-457.

Widiyantoro, S., A. Gorbatov, B. L. N. Kennett, and Y. Fukao (2000), Improving global shear wave traveltime tomography using three-dimensional ray tracing and iterative inversion, *Geophys. J. Int., 141*, 747-758.

Widiyantoro, S. and van der Hilst, R. D. (1997), Mantle structure beneath Indonesia inferred from high-resolution tomographic imaging, *Geophys. J. Int., 130*, 167-182.

Zhang, H. and C. Thurber (2006), Development and applications of double-difference seismic tomography, *Pure Appl. Geophys., 163*, 373-403.

Zhang, H. and C. H. Thurber (2003), Double-difference tomography: the method and its application to the Hayward Fault, California, *Bull. Seismol. Soc. Am., 93*, 1875-1889.

Zhao, D. and J. Lei (2004), Seismic ray path variations in a 3D global velocity model, *Phys. Earth Planet. Inter., 141*, 153-166.

Table 3.1. Regional cell layer division [*Widiyantoro and van der Hilst*, 1997] and average layer velocity [*Kennett et al*., 1995].

Layer	Depth Range (km)	Layer Mid-point Depth (km)	Average Vp (km/s)
1	0-35	17.5	6.15
2	35-70	52.5	8.04
3	70-110	90	8.05
4	110-160	135	8.10
5	160-220	190	8.25
6	220-280	250	8.45
7	280-340	310	8.67
8	340-410	375	8.91
9	410-490	450	9.50
10	490-570	530	9.76
11	570-660	615	10.06
12	660-750	705	10.91
13	750-840	795	11.11
14	840-930	885	11.27
15	930-1020	975	11.42
16	1020-1130	1075	11.58
17	1130-1250	1190	11.75
18	1250-1400	1325	11.95
19	1400-1600	1500	12.19

Table 3.2. Iteration comparison for fixed location sources (1-5) and relocated sources (3r-5r).

Iteration	Source Locations	Average Positive Anomaly*	Average Negative Anomaly*	Maximum Anomaly*	Minimum Anomaly*	Weighted Data RMS (s)	Predicted Misfit (s)	Misfit Reduction (%)	Model RMS (s)	Average absolute residual (s)
IT1	EHB	0.4286	-0.1973	12.3217	-6.9108	1.6501	1.4794	19.6219	0.1631	0.3602
IT2	EHB	0.5057	-0.2647	15.1189	-8.6878	1.1503	1.1305	3.4087	0.0590	0.0698
IT3	EHB	0.5626	-0.3156	16.8416	-9.4806	1.1366	1.1256	1.9173	0.0447	0.0409
IT4	EHB	0.6063	-0.3577	18.0544	-10.5018	1.1294	1.1219	1.3212	0.0365	0.0282
IT5	EHB	0.6436	-0.3924	18.9342	-11.1564	1.1249	1.1192	1.0132	0.0311	0.0215
IT3r	DD	0.5576	-0.3196	17.0131	-9.4673	1.1559	1.1415	2.4764	0.0496	0.0555
IT4r	DD	0.6031	-0.3612	18.2908	-10.4492	1.1460	1.1377	1.4309	0.0387	0.0318
IT5r	DD	0.6423	-0.3952	19.1879	-11.1553	1.1409	1.1348	1.0613	0.0326	0.0230

*Within regional model only!

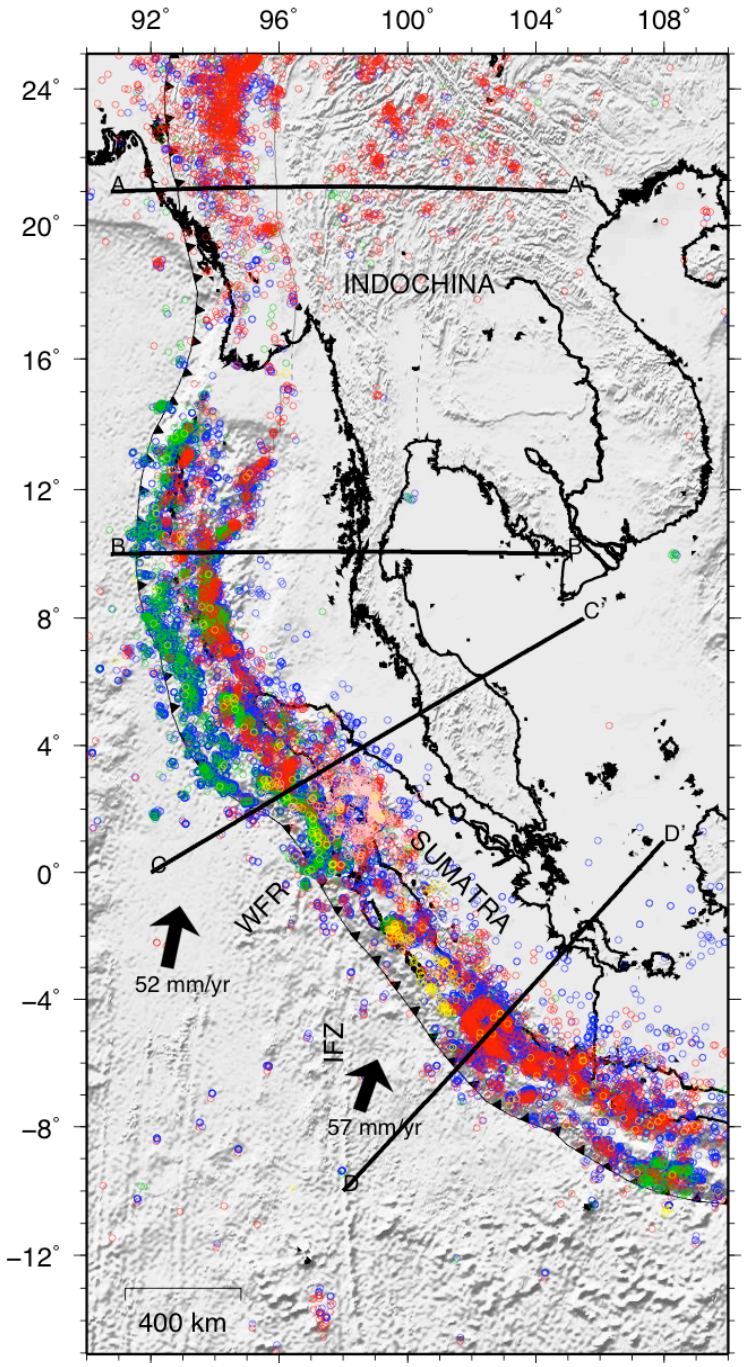

Figure 3.1. Data and regional tectonic setting. EHB bounce points (*pP*, *pwP*; blue), earthquake locations for events ocurring before 24 December 2004 (red) and after (green) through 2006 are plotted in that order. New Data not used by Pesicek et al. [2008] are also shown: EHB event locations for 2007 (yellow) and for the Toba Caldera local network (pink). Cross-section locations (A-D) for Figures 3.9b, 3.10b, and 3.11b, plate boundaries, bathymetric features (Wharton Fossil Ridge [WFR] and Investigator Fracture Zone [IFZ]), and convergence rates are also shown.

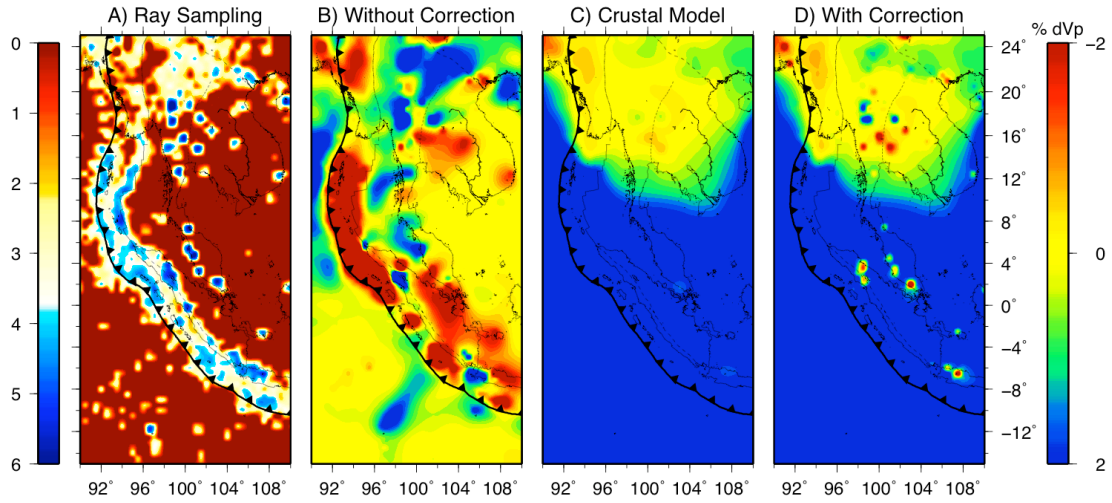

Figure 3.2. Crustal correction. A) Ray sampling of the crustal layer shown as the log of the total ray length (km) for each cell. B) Crustal layer from the model of Pesicek et al. [2008] showing strong spurious positive anomaly in the SW where there is essentially no ray coverage. C) Crustal layer used in starting model in this study from CRUST 2.0 [*Bassin et al*., 2000] and D) Iteration 2 crustal layer where perturbations are heavily damped by crustal correction. B-D are shown at 2% perturbation scale.

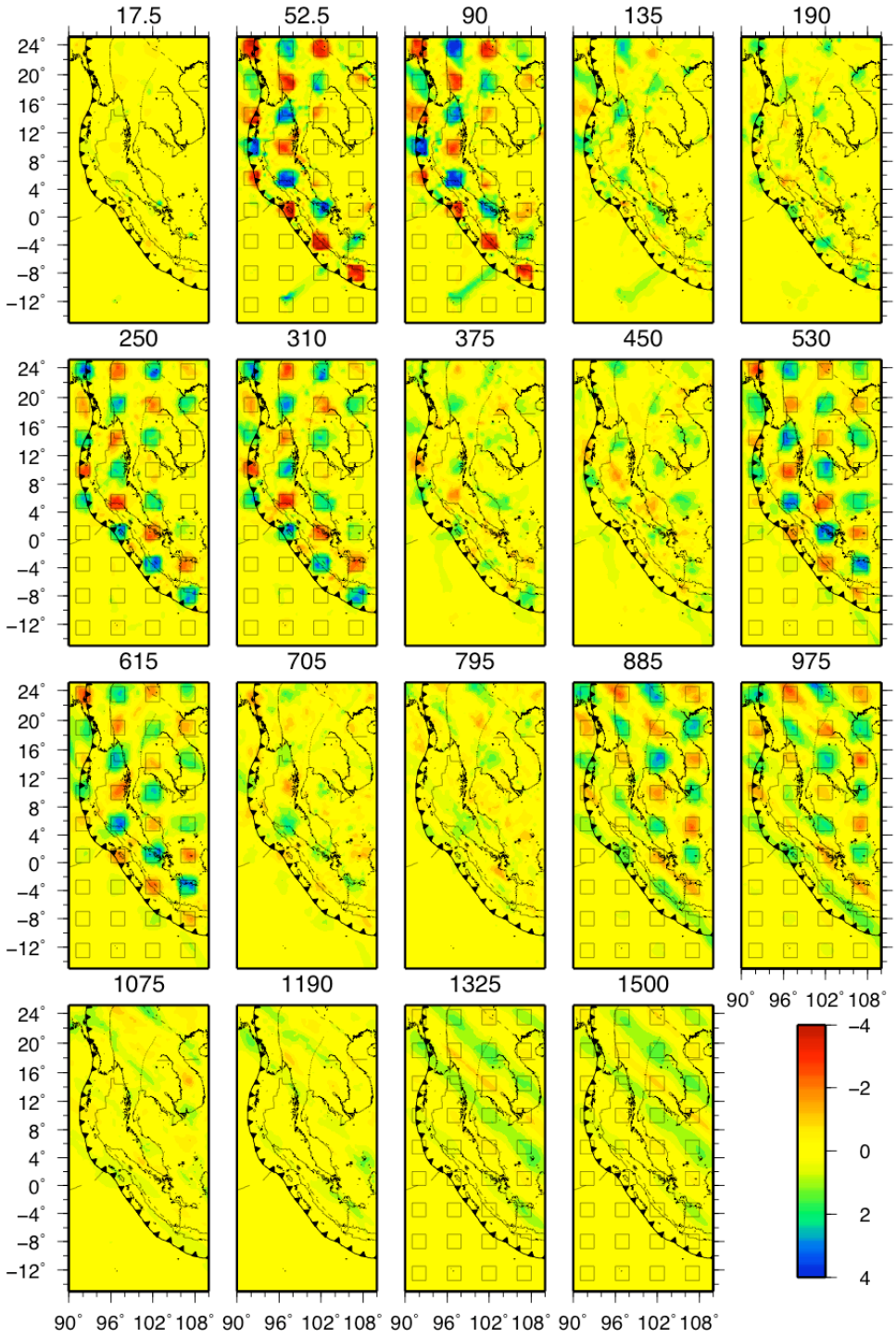

Figure 3.3a. Checkerboard restoration test after two iterations. Synthetic 4% velocity perturbation input anomalies (2.5° x 2.5°; black contours) are separated by 2.5° in latitude and longitude and by 2 layers in depth. Depths with no input anomalies are shown and the perturbations in these layers are an indication of vertical smearing.

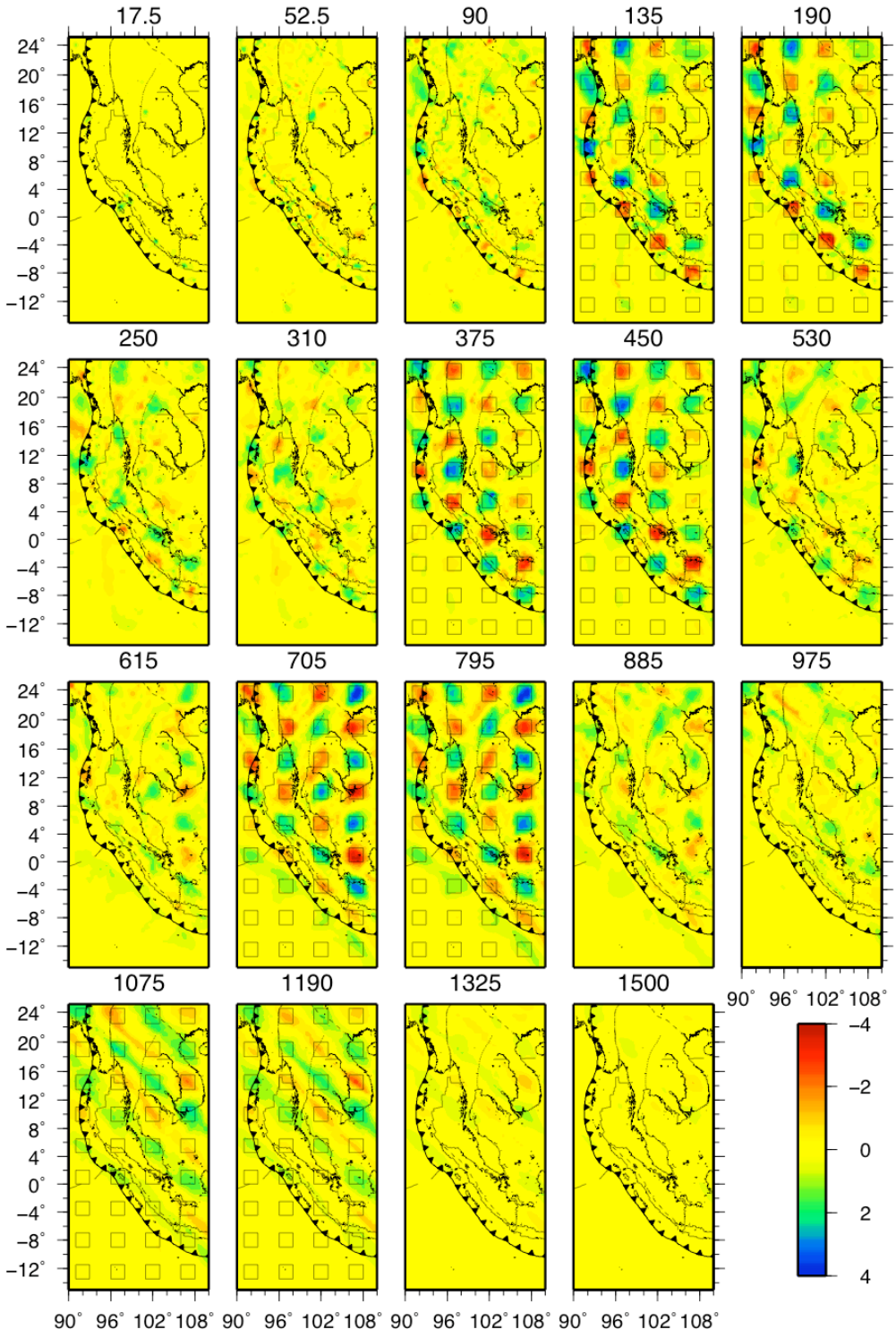

Figure 3.3b. Alternate checkerboard restoration test, the same as Figure 3.3a except the input pattern is shifted to be the opposite of Figure 3.3a, i.e. layers with (without) anomalies in Figure 3.3a now lack (have) them.

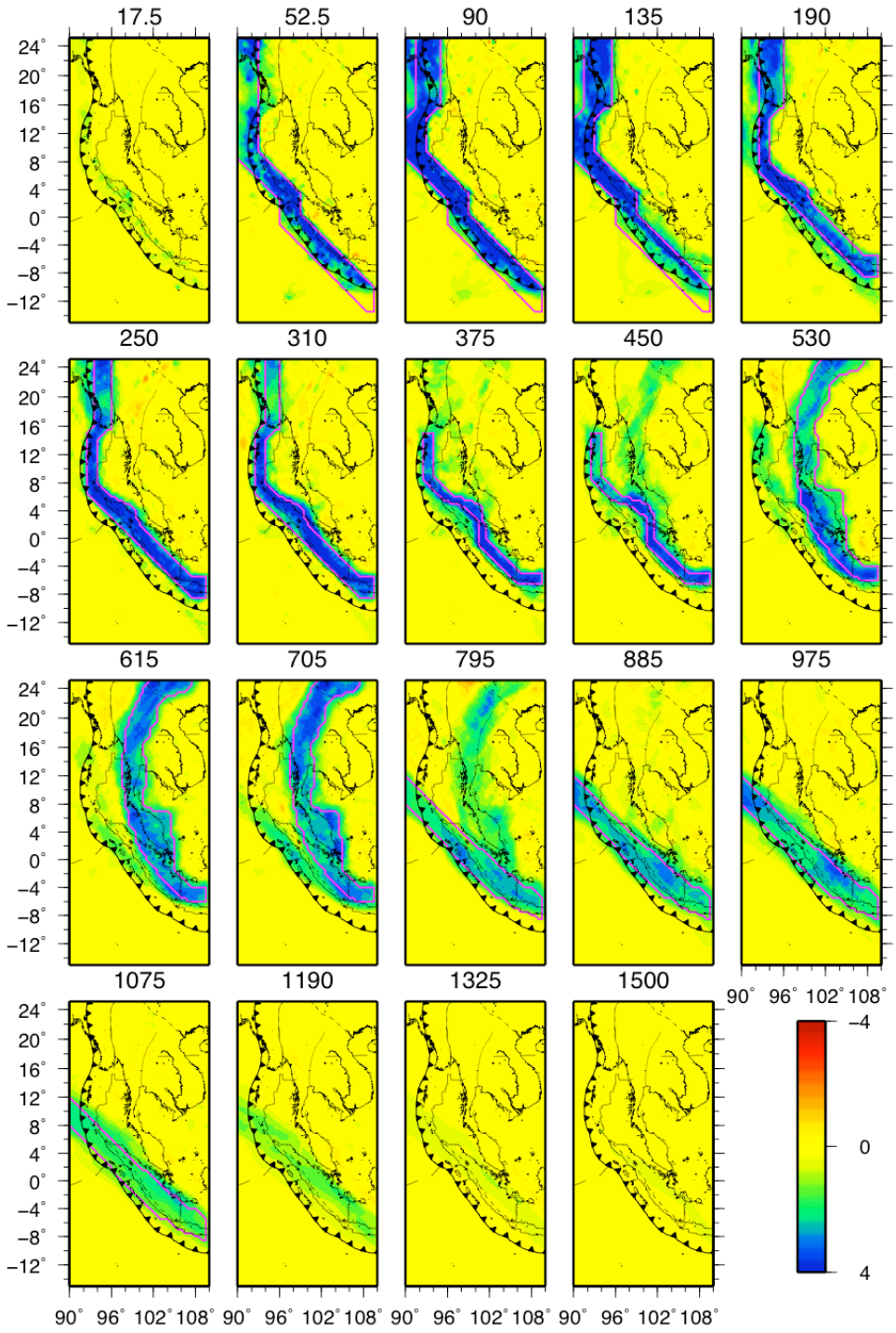

Figure 3.4. Synthetic slab restoration test after two iterations. A synthetic slab (4% velocity perturbation) broadly mimicking the geometry of the actual model (and the features we discuss) is well recovered by the data throughout the model space. The geometry of the synthetic slab is shown by magenta contours in each layer where it is present.

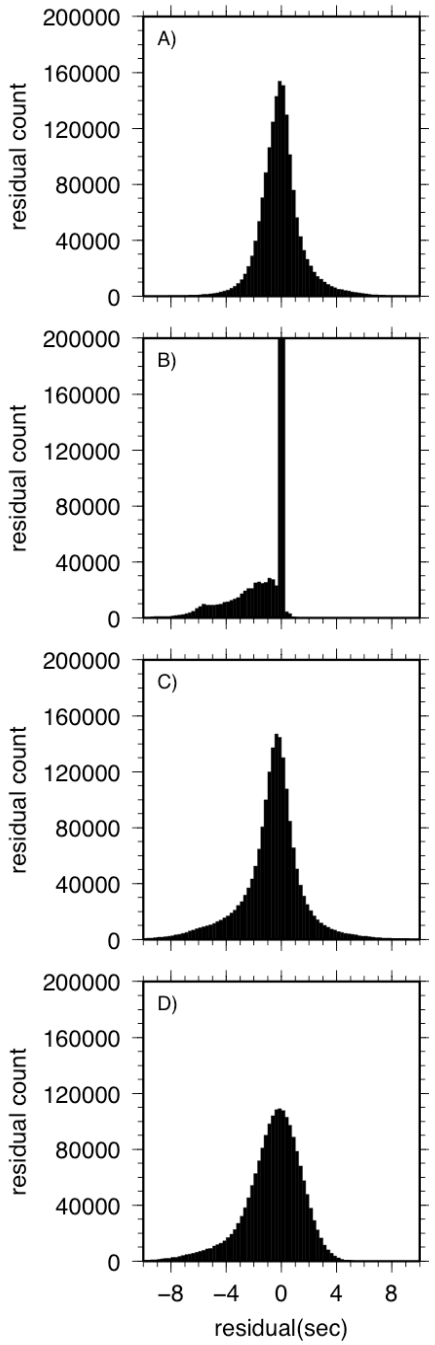

Figure 3.5. Residual distributions for the real iteration 2 inversion (A) and the synthetic slab restoration tests (B-D) (Figure 3.4). B) Synthetic slab residuals without noise, C) with the real residuals randomized and added, and D) with a Gaussian distribution of noise added (var = 2.25 sec). The actual residual distribution (A) is not well matched by a Gaussian function (D). We therefore perform our synthetic tests by randomizing the actual residuals and adding them to the synthetic residuals as noise (C).

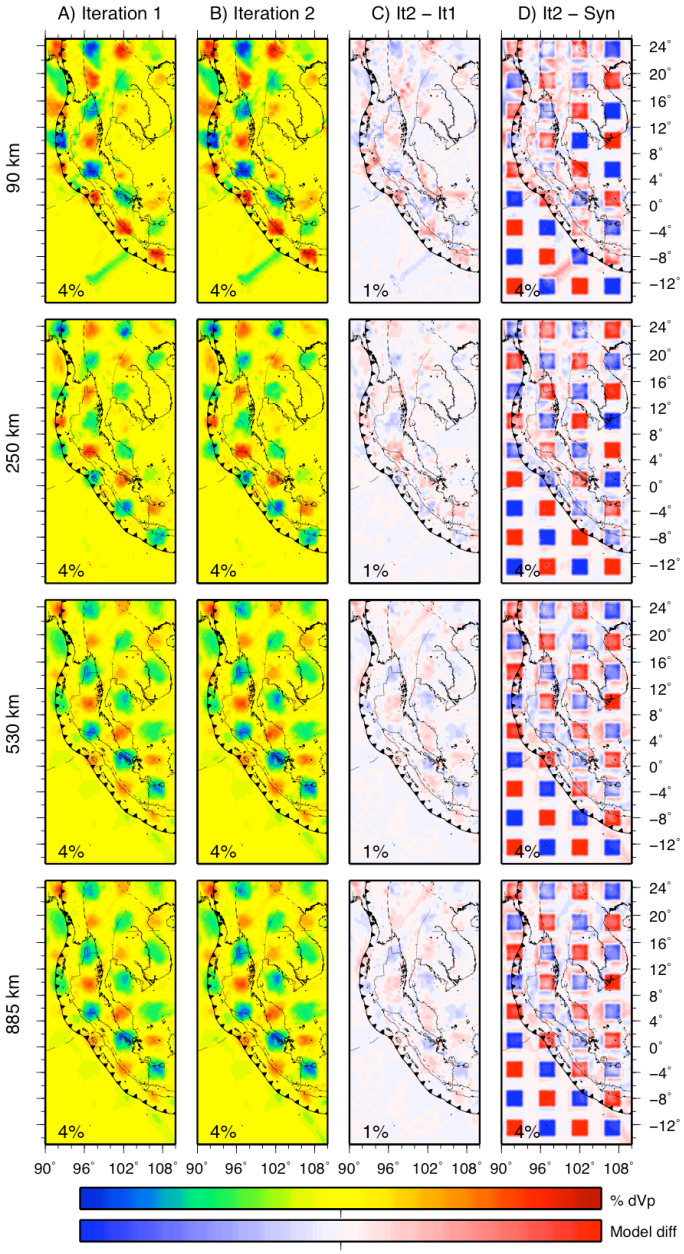

Figure 3.6a. Improvements to checkerboard restoration tests at several depths (synthetic model same as Figure 3.3a) due to iterative method. From left to right: iteration 1 results (Col. A), iteration 2 results (Col. B), the difference between iteration 2 and iteration 1 models (1% scale) (Col. C), and the difference between the synthetic input model and the recovered iteration 2 model (4% scale) (Col. D). Anomalies in Column C represent new perturbations to the recovered model due to iterative process. Column D illustrates the deficiencies of recovery of the synthetic anomalies; zero amplitude checkers in this column would represent perfect recovery. Checkers that are high (low) in amplitude represent poorly (well) recovered. Areas outside the checkers where anomaly polarity has reversed illustrate the degree of smearing of the checkers.

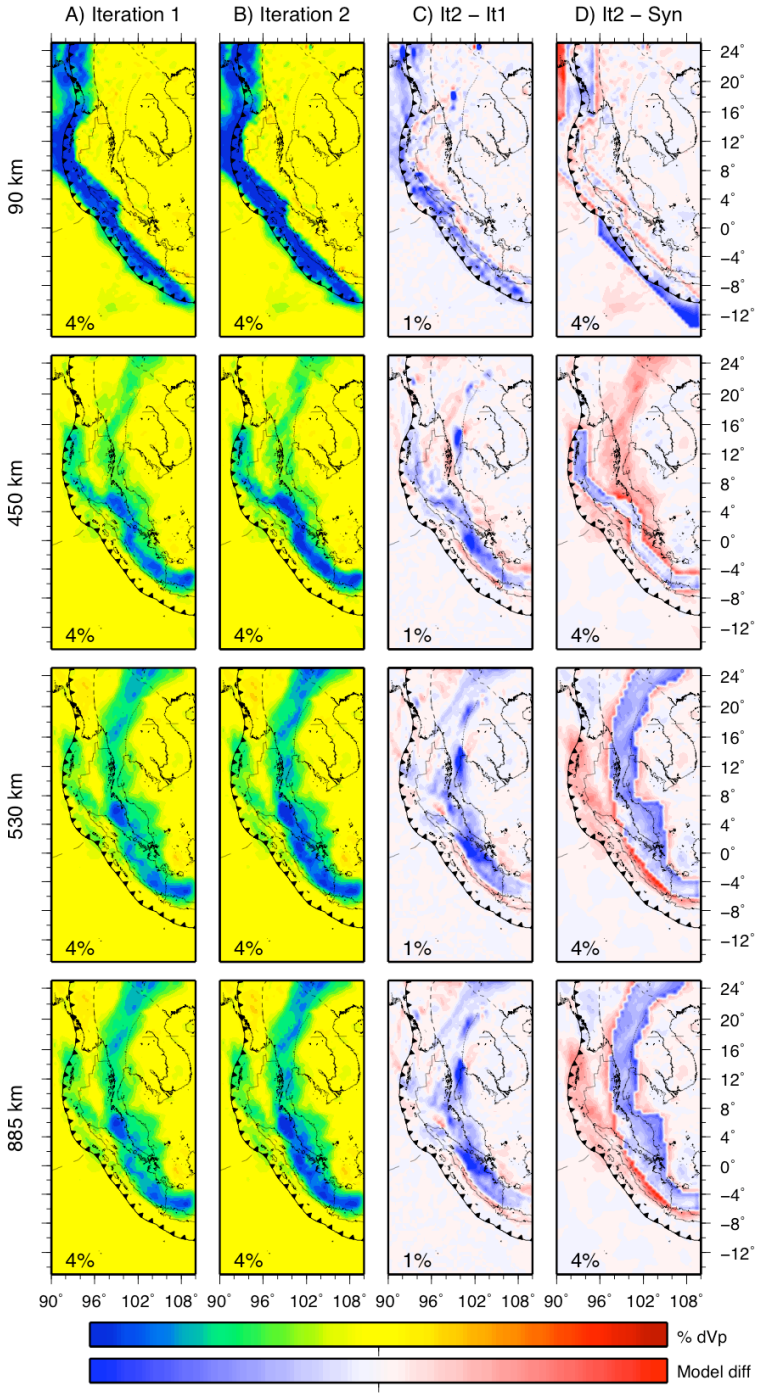

Figure 3.6b. Improvements to slab restoration tests (synthetic model same as Figure 3.4) due to iterative method, similar to Figure 3.6a. Column C illustrates the increasing amplitude at the center of the slab anomalies and the decrease in smearing at the edges of the slab anomalies through our iterative process. Column 4 shows that in the upper mantle, nearly complete recovery (zero model difference) of the synthetic slab is achieved in many areas, but that vertical smearing (red) is widespread.

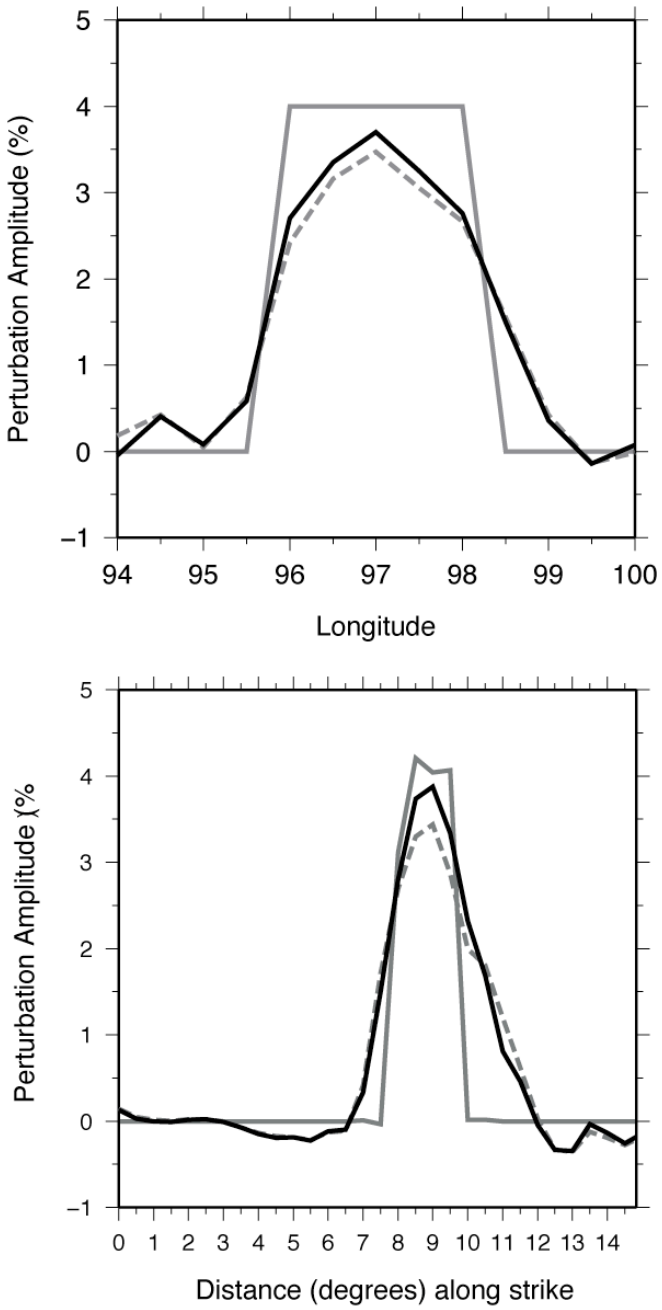

Figure 3.7. A) Restoration of the checker anomaly centered at 97°E, 5.5°N, and 90 km depth (northern Sumatra). The synthetic checker (black) is better recovered by iteration 2 (grey) than iteration 1 (grey dashed). Outside of the actual checker, smearing is slightly reduced by iteration 2. Amplitude is shown as the latitude average of the 2.5° checker. B) Restoration of synthetic slab along cross-section D (Figure 3.1) at 450 km depth showing the increase in slab amplitude and reduction of smearing outside the synthetic slab for iteration 2.

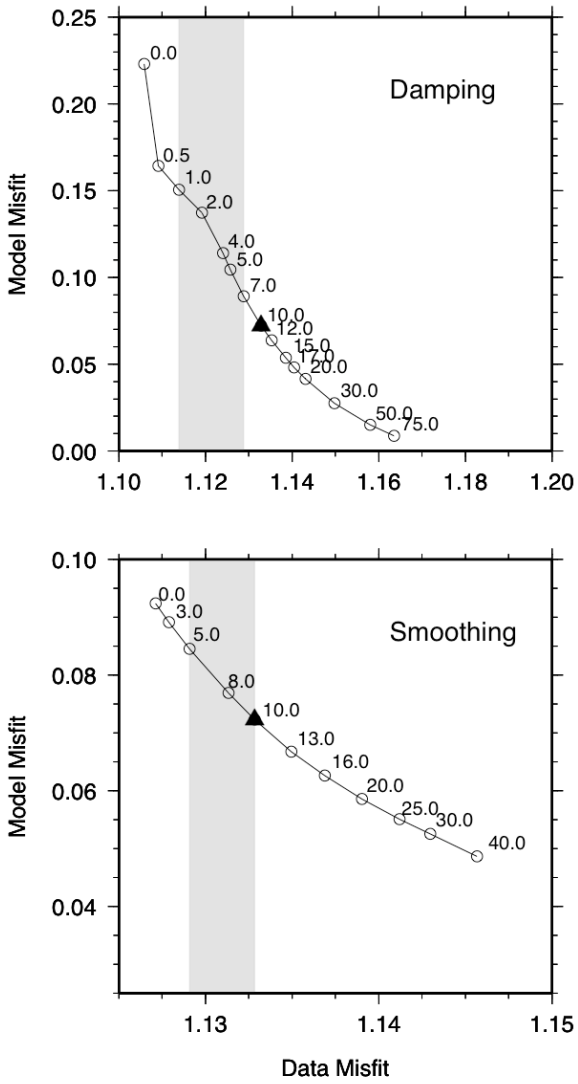

Figure 3.8. Trade off curves for damping and smoothing parameters. Our tests with synthetic data suggest optimal value ranges (gray areas) that are below the ranges suggested by the regions of maximum curvature. We chose values (triangles) that compromise between optimally recovered synthetic anomalies and optimizing the tradeoff between data misfit and model size.

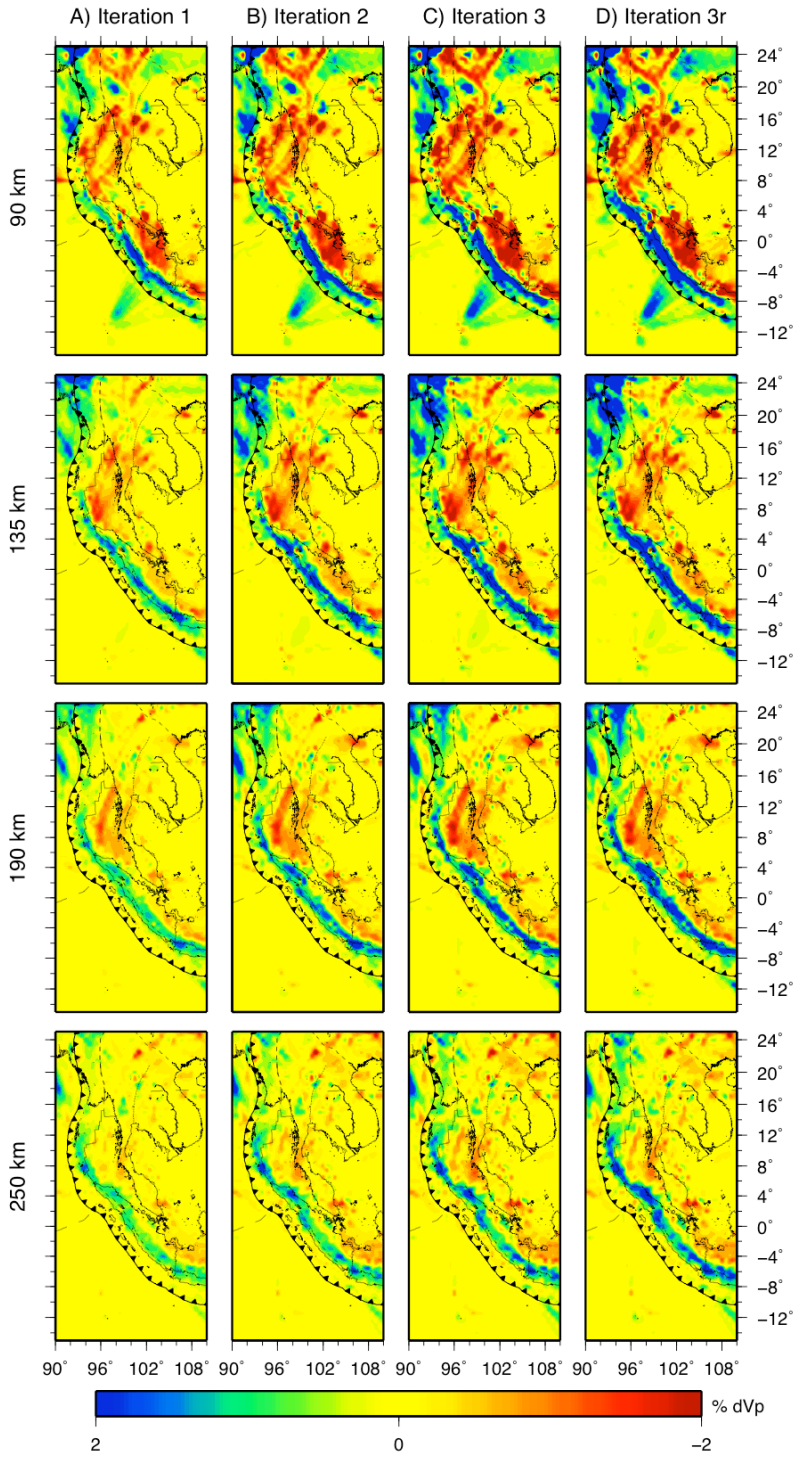

Figure 3.9a. Model results of our iterative process at several depths. Slab amplitudes increase consistently for subsequent iterations and are highest in Column D for iteration 3r, where the source locations were relocated through the iteration 2 model (Column B) prior to inversion.

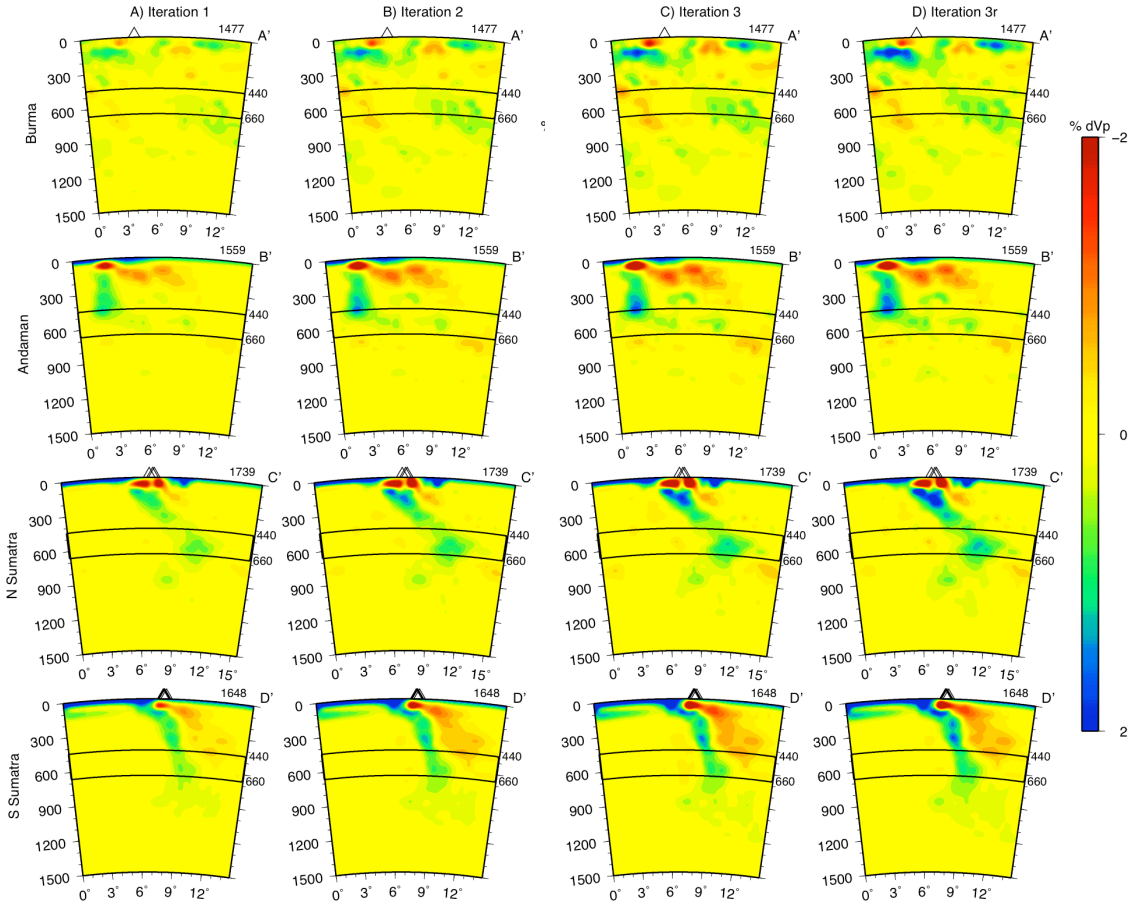

Figure 3.9b. Cross-sections (locations shown in Figure 3.1) through model results at different iterations, similar to Figure 3.9a. Slab amplitudes increase consistently for subsequent iterations and are highest in Column D for iteration 3r, where the source locations were relocated through the iteration 2 model (Column B) prior to inversion. Cross-section lengths (km) are listed at the top right of each figure. Volcano locations (triangles) are shown within 100 km on either side of each section.

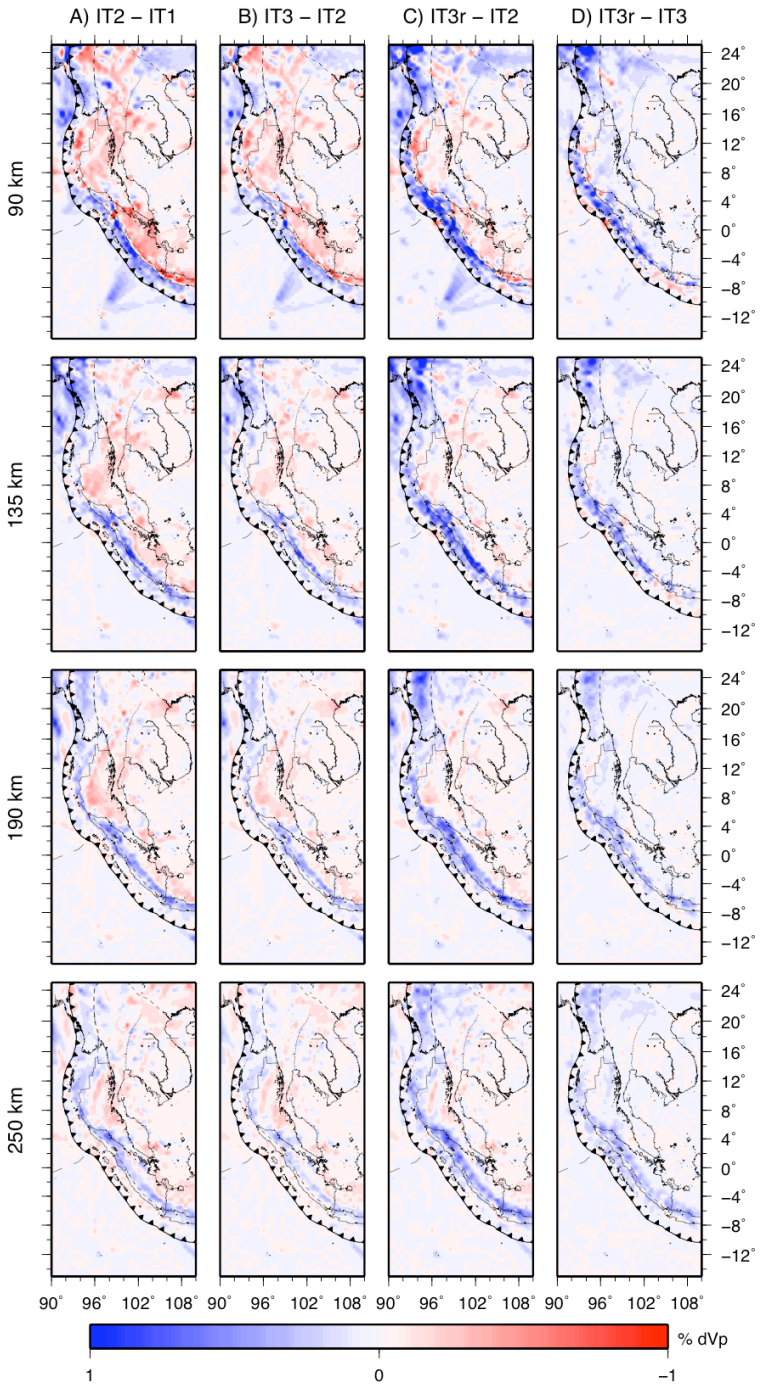

Figure 3.10a. Iteration differences for those models and depths shown in Figure 3.9. For fixed source iterations, changes in slab amplitudes lessen with further iteration (cf. Col. A and Col. B). Including source relocation increases slab amplitudes significantly (Col. C). Col. D best illustrates the improvements due to source relocation; it shows the difference between IT3 with EHB locations and IT3r with DD locations using the IT2 model. Slab anomaly differences in Col. D can be attributed solely to source relocation.

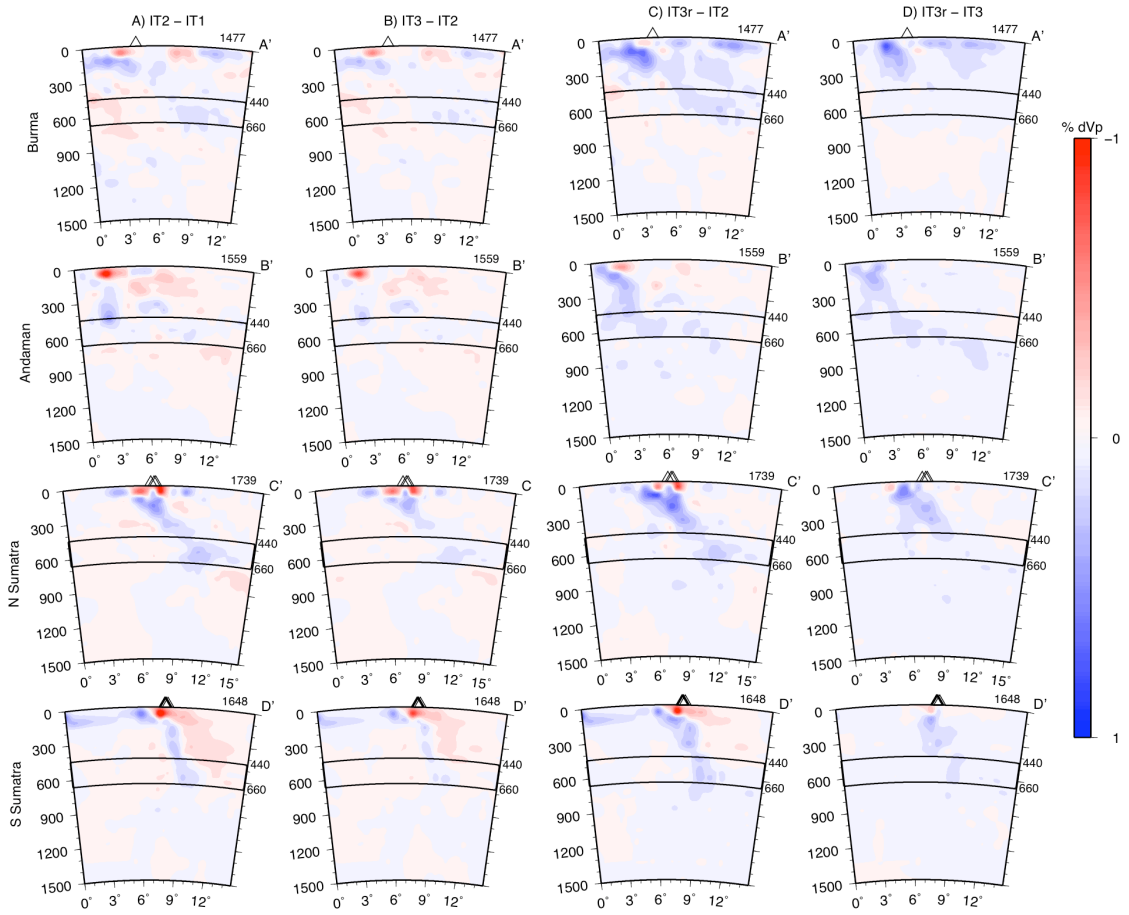

Figure 3.10b. Cross-sections (locations shown in Figure 3.1) through model differences shown in Figure 3.10a. See Figure 3.10a caption for discussion.

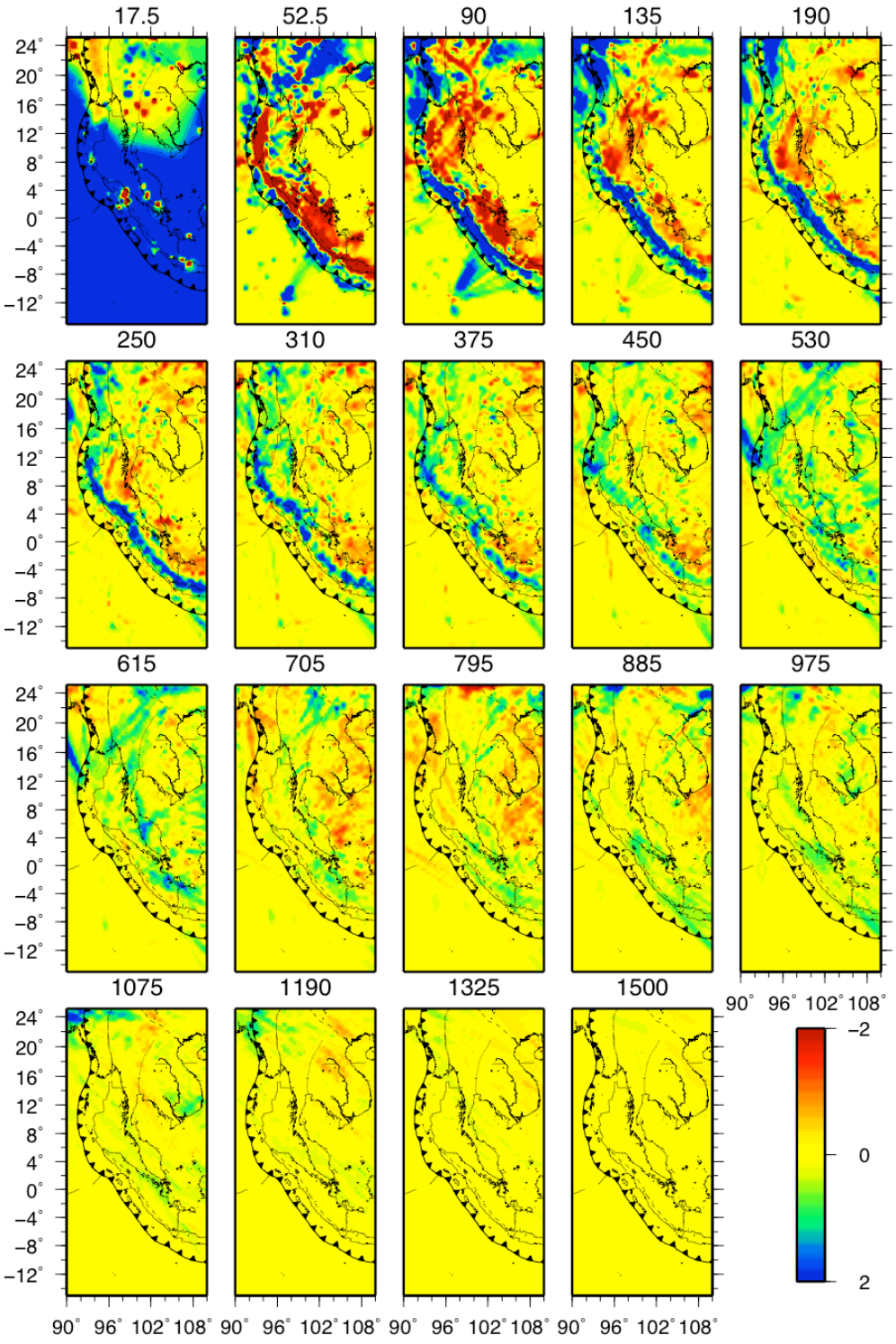

Figure 3.11a. Final model results (IT5r) for all depth layers achieved with 2 iterations with EHB source locations and 3 additional iterations with DD relocations using the IT2 model.

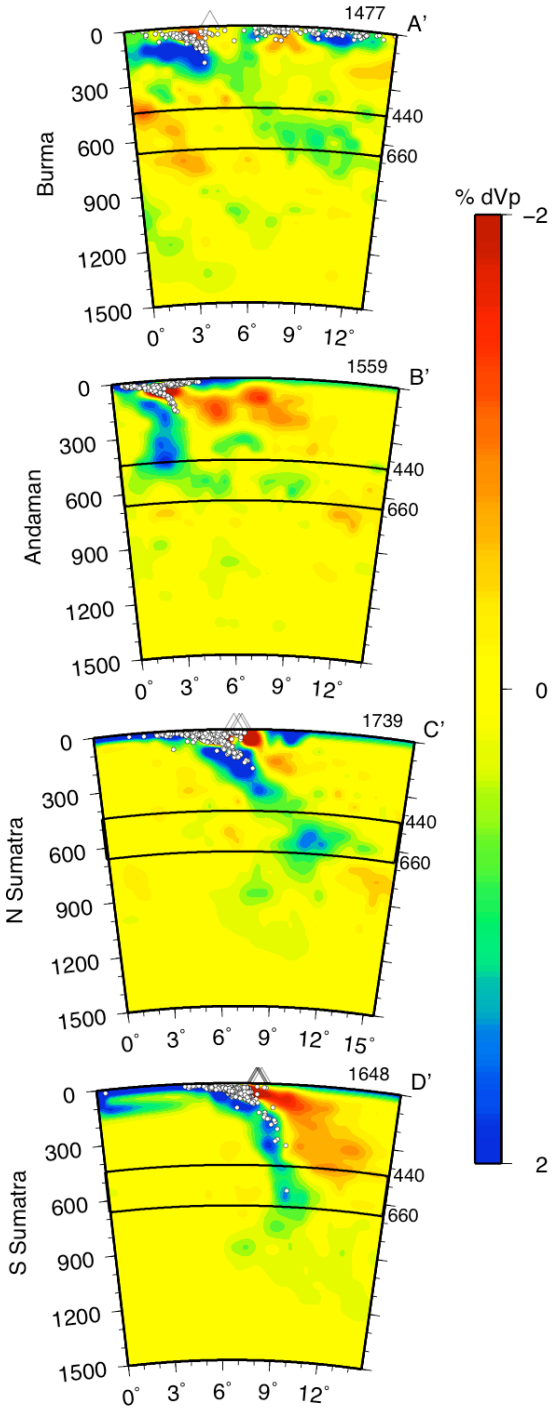

Figure 3.11b. Cross-sections (locations shown in Figure 3.1) of the final model results (IT5r). Cross-section lengths (km) are listed at the top right of each section. DD relocations (circles) and volcanoes (triangles) are shown within 100 km on either side of each section.

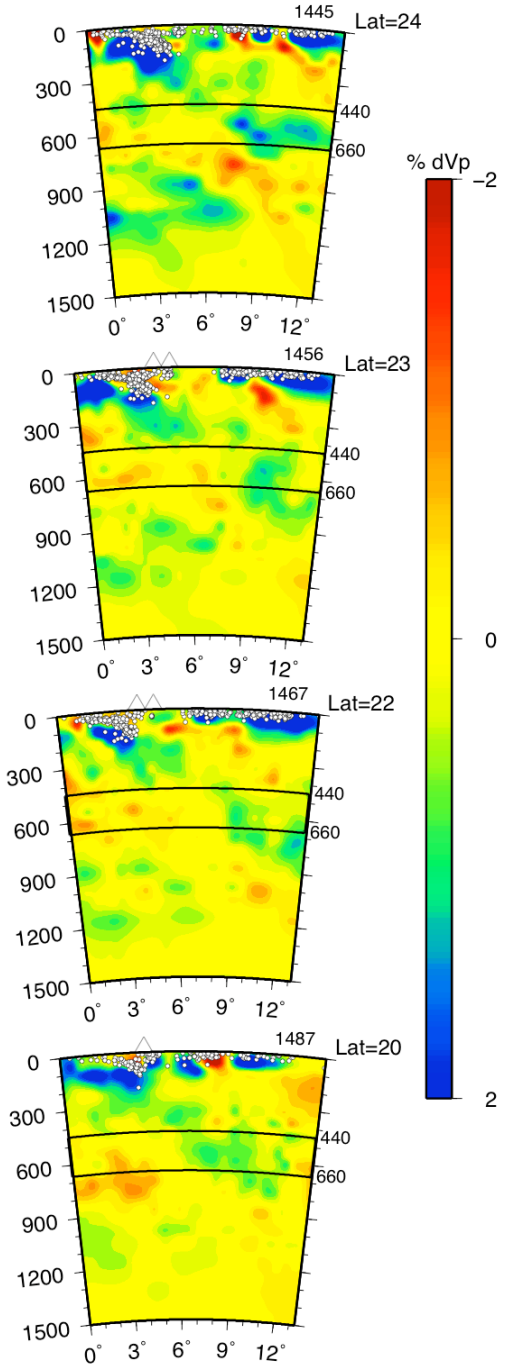

Figure 3.12. Longitude cross-sections along the Burma subduction zone that, along with Figure 3.11b-section A (at 21° Latitude), are spaced 1° apart in latitude from 24°N to 20°N. Cross-sections at 24°N, 23°N and 22°N show good separation of slab segments near the 440 km discontinuity, but at 21°N (Figure 3.11b) and 20°N, the slab appears more continuous.

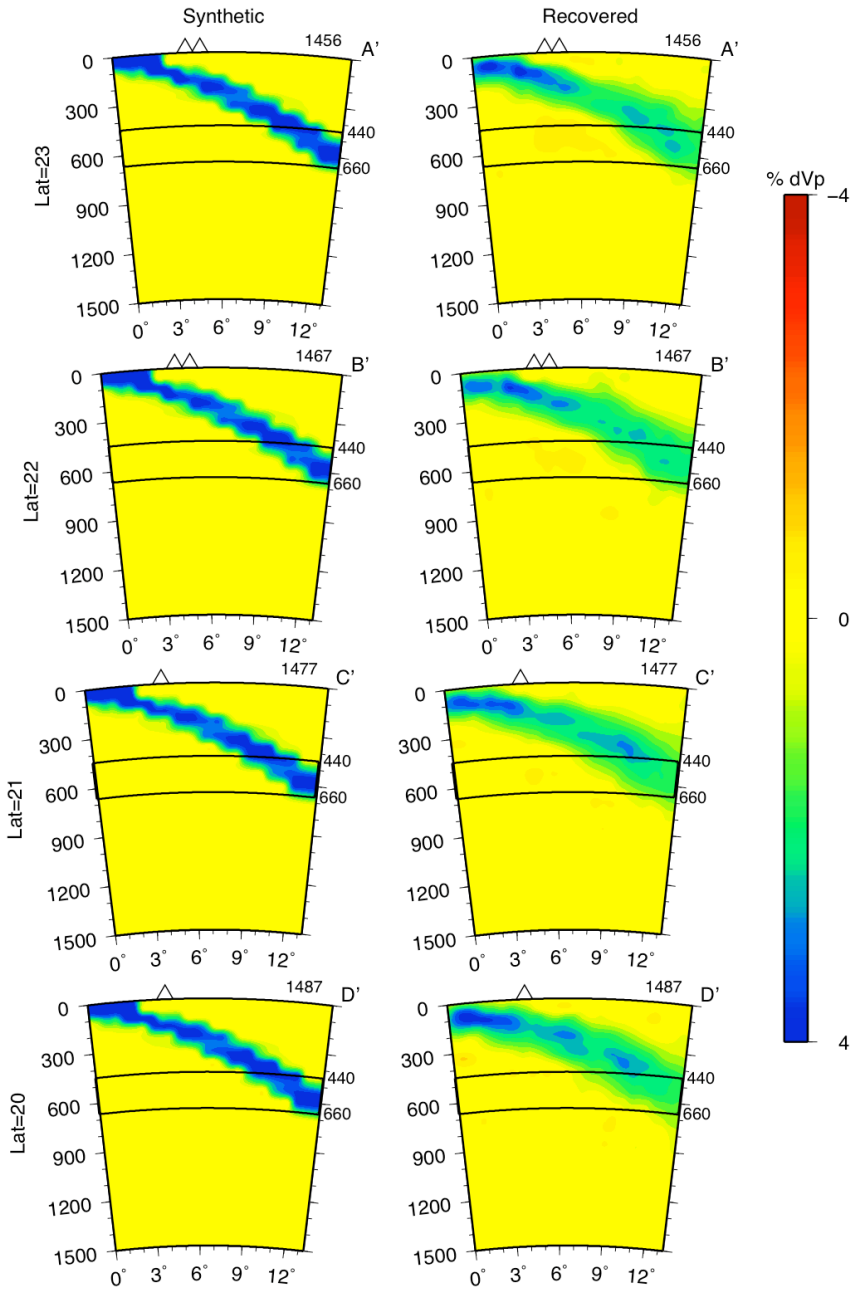

Figure 3.13a. Slab tear synthetic tests for cross-sections presented in Figures 3.11b (Lat = 21°) and 3.12 (Lat = 24° not shown). A synthetic slab (left) that is continuous through the upper mantle and into the transition zone is used in restoration tests (two iterations) similar to Figures 3.3 and 3.4 and described in the text. The results (right) suggest that ray coverage and resolution are diminished in the region where the tear was hypothesized by Pesicek et al. [2008], but may still be sufficient to distinguish a continuous slab from a torn slab.

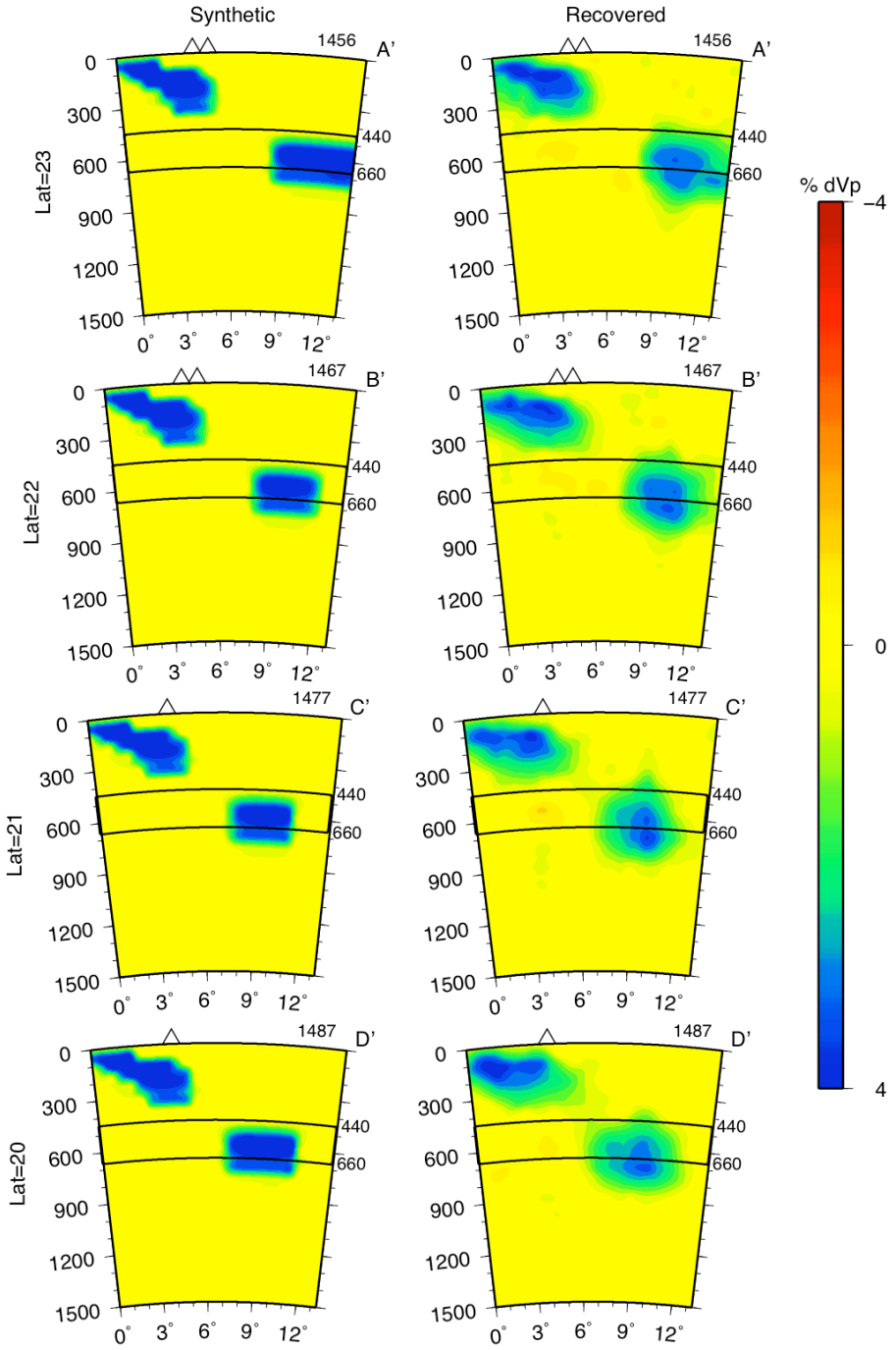

Figure 3.13b. Slab tear synthetic tests for cross-sections presented in Figures 3.11b and 3.12. A synthetic slab (left) that is discontinuous through the upper mantle and into the transition zone is used in restoration tests (two iterations) similar to Figures 3.3 and 3.4 and described in the text. The results (right) suggest that smearing of distinct anomalies is considerable. Thus a torn slab with minimal segment separation may appear continuous.

CHAPTER 4: Teleseismic Relocation of Earthquakes along the Sumatra-Andaman Subduction Zone

J.D. Pesicek, C.H. Thurber, H. Zhang, H.R. DeShon, and E.R. Engdahl

Abstract

We have extended the double-difference seismic tomography method to teleseismic distances with three-dimensional ray tracing conducted through nested regional-global models, and apply the method to relocate teleseismicity from the Sumatra-Andaman region before and after the great earthquakes of 2004 and 2005. We tested the algorithm's accuracy using independent local data and an alternate relocation method and found good agreement between the results. The use of depth phases, differential times, and realistic 3-D velocity models improves the accuracy and precision of epicenters and focal depths, systematically shifting them NE and shallower, respectively. The relocations refine the location of the megathrust and other faults, the patterns of aftershocks, and their relation to slip during the two great earthquakes. In addition, the relocations reveal several discrete features not previously discernible in the scatter of teleseismic catalogs.

4.1 Introduction

The Sumatra and Andaman Islands region is currently one of the most seismically active areas in the world. Oblique subduction of the Indo-Australian plate beneath the Eurasian plate resulted in the 26 December 2004 Mw 9.1 Sumatra-Andaman Islands and the 28 March 2005 Mw 8.7 Nias Island great earthquakes, two of the largest earthquakes ever recorded. These two events have spawned countless aftershocks in the region, including thousands of M>5 events (Figure 4.1). However, local seismic station coverage is quite limited along this archipelago. Although coverage from the few land-based seismic stations has been supplemented by several deployments of ocean bottom seismometers (OBS) following the 2004 great Sumatra-Andaman Islands earthquake [*Tilmann et al.,* 2006; *Araki et al.,* 2006; *Lin et al.,* 2009], these datasets are limited both spatially and temporally. The sum of these local data falls short of providing a comprehensive regional catalog for analysis. Thus, there is limited ability to carry out a comprehensive, high-precision investigation of the seismicity associated with these great earthquakes and their aftershock sequences.

Catalogs of arrivals at teleseismic stations therefore provide the most consistent and reliable datasets for analysis of seismicity prior to and following the 2004 and 2005 great earthquakes. Global catalogs of such data are produced and routinely updated by the International Seismic Center (ISC) and the National Earthquake Information Center (NEIC). Analyses of these data [*Dewey et al.,* 2007; *Engdahl et al.,* 2007] yield primary constraints on slab and fault geometries, regional spatio-temporal patterns of seismicity, and information on the extent of the seismogenic zone within the Sumatra-Andaman

subduction system. However, typical scatter in teleseismic locations limits delineation of the fine-scale structural features of the seismogenic zone and hinders efforts to gain further insight into the tectonic setting in which these two great earthquakes occurred.

Significant improvements to the resolution of teleseismic catalogs have been achieved by reprocessing of the ISC and NEIC global data using the Engdahl, van der Hilst, and Buland (EHB) method of single event relocation [*Engdahl et al.,* 1998]. The EHB method employs a variety of techniques to increase the accuracy of the teleseismic data, and the EHB catalog is commonly recognized as the most accurate catalog of event locations available for global seismic studies. In the Sumatra-Andaman region, teleseismic data prior to and following the 2004 and 2005 great earthquake sequences have been refined by the EHB method, reducing epicenter and focal depth uncertainties to 15 km and 10 km respectively [*Engdahl et al.,* 2007]. In this study, we attempt to further reduce the location uncertainties of the EHB catalog of ~8600 teleseismically-recorded events that occurred along the Burma, Andaman, and Sumatra subduction zones from 1964 through 2007. The improved precision of our relocations allows refinement of slab and megathrust geometry and improved characterization of the spatio-temporal seismicity patterns, the structural features of the plate boundary, and its seismogenic zone.

4.2 Teleseismic Double-Difference Earthquake Relocation

Double-difference (DD) techniques have been applied to a variety of earthquake relocation problems in recent years. The original DD method [*Waldhauser and Ellsworth,* 2000] has proven effective at determining precise relative local and regional earthquake locations within many seismic networks [e.g. *Prejean et al.,* 2002; *Schaff et al.,* 2002; *Waldhauser and Ellsworth,* 2002; *Fukuyama et al.,* 2003]. When adapted to determine velocity structure and absolute event locations in addition to relative locations [*Zhang and Thurber,* 2003], the DD method has provided high-resolution tomographic images and high-precision event locations at a variety of scales and in a variety of tectonic settings [*Zhang and Thurber,* 2006]. More recently, the DD relocation method has been successfully applied at teleseismic distances as well [*Waldhauser and Schaff,* 2007].

In order to relocate seismicity from the Sumatra-Andaman region, we have extended the DD tomography algorithm *tomoDD* of Zhang and Thurber [2003] to teleseismic distances (*teletomoDD*). The key modification of the algorithm required for teleseismic relocation was the addition of a spherical-Earth ray tracer. To determine ray paths and calculate travel times in a spherical earth, we have utilized the pseudo-bending (PB) method of Um and Thurber [1987], extended to spherical coordinates by Koketsu and Sekine [1998]. To account for heterogeneous velocity structure both inside and outside the region of interest, travel times are calculated through 3-D nested regional-global models represented as perturbations relative to the radially symmetric global model *ak135* [*Kennett et al.,* 1995]. In the Sumatra region, rays are traced through the

0.5° *P*-wave velocity model of Pesicek et al. [2008a], whereas outside the regional model, they are traced through the *MITP08* global *P*-wave perturbation model [*Li et al.*, 2008].

In addition to tracing rays for primary phases, we have modified the PB ray tracer to also trace rays for the depth phases *pP* and *pwP*. We trace depth phases initially to the EHB catalog bounce points, which are then iteratively perturbed until the angles between the upgoing and downgoing ray segments are equivalent [*Zhao and Lei,* 2004]. At teleseismic distances, these surface-reflected phases can be accurately picked and included in relocation procedures. Their inclusion is advantageous because their travel-time derivatives for depth are opposite in sign to that of direct *P* and thus they can help reduce the tradeoff between origin time and depth, thereby better constraining focal depth.

To improve the precision of the depth phase picks and to calculate precise relative arrival times for inclusion in the DD relocation, we have applied cross-correlation techniques to the publicly available waveform data from events in the region [*DeShon et al.*, 2007]. Correlation was calculated in both the second- and third-order spectral domains to maximize robustness of the correlation results and to reduce noise effects. Correlation was also performed between the noisier *pP* depth phase and the uncontaminated *P* arrival within an individual waveform to provide a high-precision differential time that directly constrains event depth. The adjusted picks were used both to recalculate initial hypocentral parameters using the EHB method and to form precise differential travel times for input into the DD relocation procedure.

With the addition of depth phase and CC data, we have included 5 different data types in the relocation procedure: primary and depth phase absolute data, primary and depth phase catalog differential times, and primary phase cross-correlation differential times. To form the catalog differential times, we followed Waldhauser and Schaff [2007] and linked each event with its 20 nearest neighbors within 300 km that had at least 15 commonly observed phases at stations within 90°, requiring a minimum of 10 differential time links per pair. Owing to the importance of the depth phase data for constraining focal depth despite their relative paucity, we relaxed these condition requirements and required only 2 links per neighbor and 2 links per pair to form depth phase differential times. In total, we have included nearly 6 million data (observed at ~2,400 stations) in the relocation procedure, including ~63,000 CC differential times and ~336,000 depth phase observations.

To properly account for the varying data quantities, types, and qualities, we applied a hierarchical dynamic weighting scheme to the data [e.g. *Waldhauser and Ellsworth,* 2000; *Zhang and Thurber,* 2003; *Waldhauser and Schaff,* 2007]. We initially gave the absolute data high weighting, because they control the absolute locations, then progressively lowered their weighting during subsequent iterations. Conversely, we progressively increased the weighting of the differential times during iterations. The final iterations were performed with the cross-correlation differential times weighted the highest to allow these more precise data to control the final locations. This type of weighting scheme allows for determination of accurate absolute locations using the 3-D

velocity model, and determination of more precise relative locations due to the use of differential times.

4.3 Results

We have successfully relocated 8605 earthquakes along the Sumatra, Andaman, and Burma subduction zones. However, for assessment of location quality, below we focus mainly on the ~1200 events for which CC data are available (Figure 4.2), due to the fact that these events are likely to show the most improvement. For these best-constrained events, we have obtained >95% reduction in data misfit compared to the initial EHB locations and significantly reduced uncertainties. We performed a jackknife uncertainty estimate for these events by re-computing their locations using 10 different subsets of recording stations, each with 10% of the stations omitted. Standard deviations of latitude, longitude, and depth from these 10 realizations assess the uncertainties, which are 1.7 km, 1.9 km, and 1.1 km, respectively. The mean shifts in epicenter (5.0 km) and depth (4.5 km) are thus significant. Although the shifts are within the original EHB uncertainties, they are systematic. Epicenter locations show a systematic shift landward, toward the NE, while depths are systematically shallower relative to the EHB locations (Figure 4.3). In the Andaman Sea region, these systematic shifts bring a large cluster of events closer to the surface and closer to the location of known faults (Figure 4.4), as might be expected given the tectonic environment.

4.3.1 Grid Search Relocation and Validation

Other than the reprocessed EHB results of Engdahl et al. [2007], there are no other comprehensive catalogs available for comparison. Thus, in order to assess the quality and accuracy of the teleseismic DD relocations, we have developed a grid search relocation technique to help validate our results. Using the same ray tracer, phase data, and 3-D velocity models as used in the DD relocation, we calculated travel times for each phase to each point in a grid area around the EHB location and computed an L1 weighted misfit at each grid point. We defined the origin time correction as the average residual of all phases at each point, and subtracted it from individual phase residuals prior to calculation of the misfit. The search for the minimum misfit computed in this way was carried out at 0.1° intervals within an initial 1° grid around the hypocenter. The grid was then redefined around the current minimum and refined to 0.1° and searched at 0.01° intervals. If the minimum-misfit point was located on a grid edge, the grid was moved and re-centered around that minimum and the search was repeated.

To compare the highest quality results, we relocated the ~1200 earthquakes that have waveforms available (Figure 4.2). These events have refined picks and CC data available for inclusion in the DD relocation and are thus most likely to have significant changes to their locations. Figure 4.3 shows a comparison of relocations of the EHB data obtained with the grid search versus *teletomoDD*. In general, there is good agreement in the pattern of shifts obtained using the two techniques. Both sets of relocations show the general NE migration of epicenters, and the shallowing of depths relative to the initial EHB locations. Overall, hypocenter shifts are small and comparable to shifts obtained by

the DD method, except for about a dozen large shifts seen in the grid search relocations, which we interpret as reflecting the differences between the L2 and L1 solutions. The agreement between the results of the two methods gives us confidence that the systematic relocation shifts we have obtained using *teletomoDD* are valid and significant, and are due in large part to the use of a realistic 3-D velocity model.

4.3.2 Comparison to OBS Determined Locations – "Ground Truth"

Although local data are absent for much of the region surrounding the rupture areas of the 2004 and 2005 great earthquakes, data from several temporary OBS deployments are or will become available for comparison with our teleseismic relocations. A set of 9 events that occurred near Simeulue Island was located using OBS stations in the vicinity of the epicenters [*Tilmann et al.,* 2006]. These events were then relocated by the EHB method with the addition of the OBS phases. From these local and teleseismic data, the depths of these 9 events are well constrained and are believed to lie on a fault at 21 km depth. We consider these locations, derived with the benefit of local data, as the most accurate locations available. They are the closest we can get to actual "ground truth" known locations. Thus, they can be used to calibrate and assess our teleseismic relocation procedure, in particular the ability of *teletomoDD* to determine focal depth.

In Figure 4.5, we show six sets of DD relocation results for these nine events without the local OBS phases included in the relocation procedure. For each of the six

sets of relocations, we have altered some part of the DD relocation procedure. For comparison, we have also relocated them using our L1 grid search method. The results show that epicentral changes to the EHB locations are relatively small despite exclusion of the OBS phases. In addition, the results are significant because they illustrate the importance of the various aspects of the relocation procedure for constraining focal depth. Assuming a known depth of 21 km, it is clear from the results that the inclusion of the depth phases, differential times, and an accurate crustal velocity structure are each necessary to properly constrain the depths of these events using only teleseismic data. Removing any one of these (Figure 4.5C, D, and E) causes the depths to locate consistently below 21 km depth. Relocation of these events using all available data and an appropriate 3-D velocity model properly constrains the depths (Figure 4.6a), even when the starting locations are significantly perturbed (Figure 4.6b). In addition, the relocations are well constrained despite the absence of CC data (only 2 CC differential times exist for all 9 events), although the level of uncertainty is greater than that calculated for the CC events (~2 km). Thus, when applied to the larger catalog of events, we can infer that our process will improve the accuracy of the locations. Other local datasets will help confirm our results when they become available [e.g. *Lin et al.,* 2009].

4.4 Discussion

Our results illustrate the advantages of teleseismic relocation using t*eletomoDD*, which combines advantages of absolute relocation using a realistic 3-D velocity model with the advantages of relative relocation using differential times. Not only have we

obtained more accurate absolute locations where systematic shifts have presumably reduced regional biases, but we have also obtained improvements to the relative locations of the events, visible in the decreased scatter in the new locations, which better define slab geometry (Figure 4.7). In addition, events whose depths were previously poorly constrained by the EHB method, and were thus assigned fixed depths, now have free depth solutions constrained by the differential times, eliminating the horizontal linear artifacts apparent in many cross-sections of EHB seismicity (e.g. Figure 4.7c, 13-16). When overlain on an accurate 3-D velocity model [*Pesicek et al.,* 2008a], the results provide the most comprehensive view of the large-scale structure of this subduction zone yet available (Figure 4.8).

At a smaller scale, our refined locations in the region of the bend in the trench and the area surrounding the rupture zones of the 2004 and 2005 great earthquakes (Figure 4.9) provide better constraints on the aftershock distribution and its relation to prior seismicity and coseismic slip. Events prior to the 2004 event mostly locate downdip of slip from the 2004 event and away from the trench (Figure 4.10) [see also *Engdahl et al.,* 2007]. In contrast, aftershocks mostly occur surrounding the areas of high coseismic slip [*Chlieh et al.,* 2007], including many events at or near the trench. In addition, the relocations show that several segments of the Sumatra and Andaman faults become inactive following the 2004 event.

In the region surrounding the rupture of the 2005 event, seismicity is again lacking in the rupture zone prior to the event and concentrated along its boundaries after the event (Figure 4.11). Our DD relocations of these aftershocks show a curvilinear trend

similar to the curve of the trench (Figure 4.11), suggesting that the fold in the slab, interpreted from local seismicity to exist from ~75-200 km depth [*Fauzi et al.,* 1996], and from tomography results to extend through the upper mantle and into the transition zone [*Pesicek et al.,* 2008b], also exists at more shallow depths and is thus a primary feature of the downgoing plate. These aftershocks locate at the updip limit of coseismic slip, at depths of ~15-25 km, across the entire rupture area. The locations of these events may be revealing a mechanical barrier to rupture on the megathrust. If such a barrier exists here, slip from the 2005 event would have concentrated stress along it. This stress was subsequently relaxed by the aftershocks (Figure 4.11) and by aseismic afterslip updip of the aftershocks that was observed all the way to the trench [*Hsu et al.*, 2006]. This barrier may also have contributed to the lack of a significant tsunami caused by the 2005 event. Unfortunately, existing local bathymetric and reflection data in the region [*Henstock et al.,* 2006; *Sibuet et al.,* 2007; *Singh et al.,* 2008; *Franke et al.*, 2008] do not extend far enough south to cover the area where these events occurred, so the nature of this feature remains uncertain.

North of this arcuate seismic feature and directly north of Simuelue Island, good local seismic and bathymetric coverage does exist. The epicenter of the 2004 event and the southern boundary of the Andaman microplate locate in this region [*DeShon et al.,* 2005]. Reflection and bathymetric studies of this area have revealed the locations of many splay and backthrust faults here [*Henstock et al.,* 2006; *Sibuet et al.,* 2007; *Singh et al.,* 2008]. Directly north of the cluster of seismicity revealed in Figure 4.11, relocations of a group of aftershocks following the 1976 M7 event, thought to have ruptured a

shallow subduction thrust fault above the main megathrust [*DeShon et al.,* 2005], now show a geometry indicative of a backthrust (Figure 4.12), which may be the deeper extension of a backthrust imaged landward of the West Andaman Fault in the same region by Singh et al. [2008].

Patterns of seismicity in this area (Figure 4.12) may be reflecting plate structures that influence rupture segmentation on the megathrust. There is good spatial correspondence of a gap in seismicity below the center of Simuelue Island (seen in Figure 4.12) with the saddle-shaped region of minimal uplift between the 2004 and 2005 ruptures discussed by Briggs et al. [2006]. Based on seismic refraction studies, Franke et al. [2008] propose a buried fracture zone below Simuelue as a cause for rupture segmentation between the 2004 and 2005 events. They cite EHB locations directly north of Simuelue as possibly supporting the presence of such a feature. Our relocations of these events show the same rough NNE trend but neither bolster nor deny their claim. If there is fracture zone subducting here, it seems to be aseismic beneath Simuelue but seismic directly north of it.

A fracture zone that is apparent in our relocations but not readily visible in the locations of Engdahl et al. [2007] is the Investigator Fracture Zone (IFZ). The IFZ subducts just south of the bend in the trench. This highly seismic bathymetric feature may have caused a small tear in the slab below Toba Caldera [*Fauzi et al.,* 1996; *Page et al.,* 1979]. Our relocations show this feature quite well, and are in excellent agreement with the local earthquake locations of Fauzi et al. [1996] (Figure 4.13). In addition, the location of the seismicity on the IFZ correlates with a change in the geometry of the slab

visible in tomography results [*Pesicek et al.,* 2008b]. Figure 4.13b shows an apparent vertical offset in the fast slab that correlates with the seismicity of the IFZ. This offset shows an east-side up sense of motion, as would be expected if the IFZ was accommodating arc parallel shear stress due to oblique convergence. However, the available fault plane solutions for these events indicate an east-side down sense of motion on a near vertical nodal plane parallel to the IFZ [*Fauzi et al.,* 1996].

Alternatively, the apparent offset in the slab (Figure 4.13b) could be a result of subduction of the Wharton fossil ridge (WFR), which would be low velocity relative to the slab. What, if any, interaction there is between the WFR and the IFZ on the downgoing plate below Sumatra and the broad slow anomalies we have imaged beneath Toba Caldera (also imaged by *Koulakov et al*. [2009]) is unknown. The WFR appears to be relatively aseismic. However, the existence of another linear trend in the seismicity (but with many fewer events) just west of the IFZ may correspond to a subducted extension of the WFR (e.g. in Figures 4.7a and 4.13a). It is possible that the IFZ and/or WFR, or the interaction of the two, causes a weakness in the slab visible as a low velocity feature in Figure 4.13b, which might also be related to volcanism at Toba Caldera.

The IFZ may also limit rupture propagation in the region, as suggested by Fauzi et al. [1996]. Although most coseismic slip from the 2005 event ceased just south of Nias Island [*Briggs et al.,* 2006] (Figure 4.11), significant afterslip occurred directly south of the coseismic slip [*Hsu et al.,* 2006], filling in the gap between Nias Isand and the Batu Islands, which lie directly above the inferred location of the IFZ on the megathrust. Slip in the region of the Batu Islands apparently did occur during a 1935 Mw 7.7 event, but it

does not seem to be laterally extensive, and no other historical event can be considered to have ruptured across the IFZ [*Briggs et al.,* 2006; *McCaffrey,* 2009]. In addition, the IFZ and the region directly south of it were relatively quiet seismically following the 2004 and 2005 events (Figures 4.11 and 4.13), suggesting that stress release from these two events did not affect the area directly south of the IFZ or that the coseismic stresses unloaded the adjacent faults.

4.5 Summary

We have successfully relocated >8000 earthquakes along the Sumatra, Andaman, and Burma subduction zones using a teleseismic DD method that improves both absolute locations and relative locations using absolute and differential times for primary and depth phases. For events for which CC data are available (~15%), location uncertainties are less than 2 km and average shifts relative to reprocessed EHB locations [*Engdahl et al.,* 2007] are ~5 km in epicenter and depth. Systematic epicenter shifts are landward and to the NW while depths are consistently shallower than the original locations. In addition to better defining slab and megathrust geometry by decreasing location scatter, several key structural features are well defined by the relocations, including the IFZ, warping of the megathrust, Andaman backarc faults and others in the region at shallow depths. These and other features of our relocations may refine previous interpretations in several studies where the conclusions were based in part on EHB locations in the region. Future work will focus on further refining locations and velocity structure jointly and at a finer

scale. In the process, we hope to incorporate other new local datasets to increase data coverage and provide further "ground truth" assessment of our results.

References

Araki, E., M. Shinohara, K. Obana, T. Yamada, Y. Kaneda, T. Kanazawa, and K. Suyehiro (2006), Aftershock distribution of the 26 December 2004 Sumatra-Andaman earthquake from ocean bottom seismographic observation; The 2004 Great Sumatra earthquake and tsunami, *Earth, Planets and Space, 58*, 113-119.

Briggs, R. W. et al. (2006), Deformation and slip along the Sunda Megathrust in the great 2005 Nias-Simeulue earthquake, *Science, 311*, 1897-1901.

Chlieh, M. et al. (2007), Coseismic slip and afterslip of the great Mw 9.15 Sumatra-Andaman earthquake of 2004, *Bull. Seismol. Soc. Am., 97*, S152-173.

Curray, J. R. (2005), Tectonics and history of the Andaman Sea region, *Journal of Asian Earth Sciences, 25*, 187-232.

DeShon, H. R., C. H. Thurber, M. R. Brudzinski, and E. R. Engdahl (2007), A semi-automated technique for waveform cross-correlation of teleseismically recorded depth phases, *Seismol. Res. Lett., 78*.

DeShon, H. R., E. R. Engdahl, C. H. Thurber, and M. Brudzinski (2005), Constraining the boundary between the Sunda and Andaman subduction systems: Evidence from the 2002 Mw 7.3 Northern Sumatra earthquake and aftershock relocations of the 2004 and 2005 great earthquakes, *Geophys. Res. Lett., 32*, 1-5.

Dewey, J. W., G. Choy, B. Presgrave, S. Sipkin, A. C. Tarr, H. Benz, P. Earle, and D. Wald (2007), Seismicity associated with the Sumatra-Andaman Islands earthquake of 26 December 2004, *Bull. Seismol. Soc. Am., 97*, 25-42.

Engdahl, E. R., van der Hilst, R. D., and R. Buland (1998), Global teleseismic earthquake relocation with improved travel times and procedures for depth determination, *Bull. Seismol. Soc. Am., 88*, 722-743.

Engdahl, E. R., A. Villasenor, H. R. DeShon, and C. H. Thurber (2007), Teleseismic Relocation and Assessment of Seismicity (1918-2005) in the Region of the 2004 Mw 9.0 Sumatra-Andaman and 2005 Mw 8.6 Nias Island Great Earthquakes, *Bull. Seismol. Soc. Am., 97*, S43-61.

Fauzi, R. McCaffrey, D. A. Wark, Sunaryo, and P. Y. Prih Haryadi (1996), Lateral variation in slab orientation beneath Toba Caldera, northern Sumatra, *Geophys. Res. Lett., 23*, 443-446.

Franke, D., M. Schnabel, S. Ladage, D. R. Tappin, S. Neben, Y. S. Djajadihardja, C. Müller, H. Kopp, and C. Gaedicke (2008), The great Sumatra–Andaman earthquakes—Imaging the boundary between the ruptures of the great 2004 and 2005 earthquakes, *Earth Planet. Sci. Lett., 269*, 118-130.

Fukuyama, E., W. L. Ellsworth, F. Waldhauser, and A. Kubo (2003), Detailed Fault Structure of the 2000 Western Tottori, Japan, Earthquake Sequence, *Bull. Seismol. Soc. Am., 93*, 1468-1478.

Henstock, T. J., L. C. McNeill, and D. R. Tappin (2006), Seafloor morphology of the Sumatran subduction zone: Surface rupture during megathrust earthquakes?, *Geology, 34*, 485-488.

Hsu, Y., M. Simons, J. Avouac, J. Galetzka, K. Sieh, M. Chlieh, D. Natawidjaja, L. Prawirodirdjo, and Y. Bock (2006), Frictional afterslip following the 2005 Nias-Simeulue earthquake, Sumatra, *Science, 312*, 1921-1926.

Kennett, B. L. N., E. R. Engdahl, and R. Buland (1995), Constraints on seismic velocities in the Earth from traveltimes, *Geophys. J. Int., 122*, 108-124.

Koketsu, K. and S. Sekine (1998), Pseudo-bending method for three-dimensional seismic ray tracing in a spherical earth with discontinuities, *Geophys. J. Int., 132*, 339-346.

Koulakov, I., T. Yudistira, B. Luehr, and Wandono (2009), *P*, *S* velocity and V_P/V_S ratio beneath the Toba caldera complex (Northern Sumatra) from local earthquake tomography, *Geophys. J. Int., 177*, 1121-1139.

Li, C., van der Hilst, R. D., E. R. Engdahl, and S. Burdick (2008), A new global model for P wave speed variations in Earth's mantle, *Geochem. Geophys. Geosyst., 9*, 1-21.

Lin, J., X. Le Pichon, C. Rangin, J. Sibuet, and T. Maury (2009), Spatial aftershock distribution of the 26 December 2004 great Sumatra-Andaman earthquake in the northern Sumatra area, *Geochem. Geophys. Geosyst., 10*.

McCaffrey, R. (2009), The Tectonic Framework of the Sumatran Subduction Zone, *Annu. Rev. Earth Planet. Sci., 37*, 345-366.

Page, B. G. N., J. D. Bennett, N. R. Cameron, D. M. Bridge, D. H. Jeffery, W. Keats, J. Thaib, J. V. Hepworth, M. G. (. Audley-Charles, and J. V. (. Hepworth (1979), A review of the main structural and magmatic features of northern Sumatra; Magmatism and tectonics in SE Asia, *Journal of the Geological Society of London, 136*, 569-579.

Pesicek, J., C. Thurber, H. Zhang, H. DeShon, S. Widiyantoro, and E. Engdahl (2008a), Sharpened tomographic image of the subducting slab beneath the Sumatra-Andaman region from 3-D ray tracing and earthquake relocation, American Geophysical Union, Fall Meeting 2008, abstract# S14A-07.

Pesicek, J. D., C. H. Thurber, S. Widiyantoro, E. R. Engdahl, and H. R. DeShon (2008b), Complex slab subduction beneath northern Sumatra, *Geophys. Res. Lett., 35*, L20303.

Prejean, S. G., W. L. Ellsworth, M. D. Zoback, and F. Waldhauser (2002), Fault structure and kinematics of the Long Valley Caldera region, California, revealed by high-

accuracy earthquake hypocenters and focal mechanism stress inversions, *J. Geophys. Res., 107*, 19.

Pubellier, M., F. Ego, N. Chamot-Rooke, and C. Rangin (2003), The building of pericratonic mountain ranges: structural and kinematic constraints applied to GIS-based reconstructions of SE Asia, *Bull. Soc. Geol. Fr., 174*, 561-584.

Schaff, D. P., G. H. R. Bokelmann, G. C. Beroza, F. Waldhauser, and W. L. Ellsworth (2002), High-resolution image of Calaveras Fault seismicity, *J.Geophys.Res, 107*, 2186.

Sibuet, J. et al. (2007), 26th December 2004 great Sumatra–Andaman earthquake: Co-seismic and post-seismic motions in northern Sumatra, *Earth Planet. Sci. Lett., 263*, 88-103.

Singh, S. C., H. Carton, P. Tapponnier, N. D. Hananto, A. P. S. Chauhan, D. Hartoyo, M. Bayly, S. Moeljopranoto, T. Bunting, and P. Christie (2008), Seismic evidence for broken oceanic crust in the 2004 Sumatra earthquake epicentral region, *Nature Geoscience, 1*, 777-781.

Tilmann, F., E. Flueh, I. Grevemeyer, L. Handayani, H. Kopp, B. Suwargadi, W. Triyoso, and M. Heintz (2006), First results from a combined marine and land passive seismic network near Simeulue Island, Eos Trans. AGU, Fall Meeting supplement.

Um, J. and C. H. Thurber (1987), A fast algorithm for two-point seismic ray tracing, *Bull. Seismol. Soc. Am., 77*, 972-986.

Waldhauser, F. and W. L. Ellsworth (2002), Fault structure and mechanics of the Hayward Fault, California, from double-difference earthquake locations, *J. Geophys. Res, 107*, 1-15.

Waldhauser, F. and W. L. Ellsworth (2000), A double-difference earthquake location algorithm; method and application to the northern Hayward Fault, California, *Bull. Seismol. Soc. Am., 90*, 1353-1368.

Waldhauser, F. and D. Schaff (2007), Regional and teleseismic double-difference earthquake relocation using waveform cross-correlation and global bulletin data, *J. Geophys. Res., 112*.

Zhang, H. and C. Thurber (2006), Development and applications of double-difference seismic tomography, *Pure Appl. Geophys., 163*, 373-403.

Zhang, H. and C. H. Thurber (2003), Double-difference tomography: the method and its application to the Hayward Fault, California, *Bull. Seismol. Soc. Am., 93*, 1875-1889.

Zhao, D. and J. Lei (2004), Seismic ray path variations in a 3D global velocity model, *Phys. Earth Planet. Inter., 141*, 153-166.

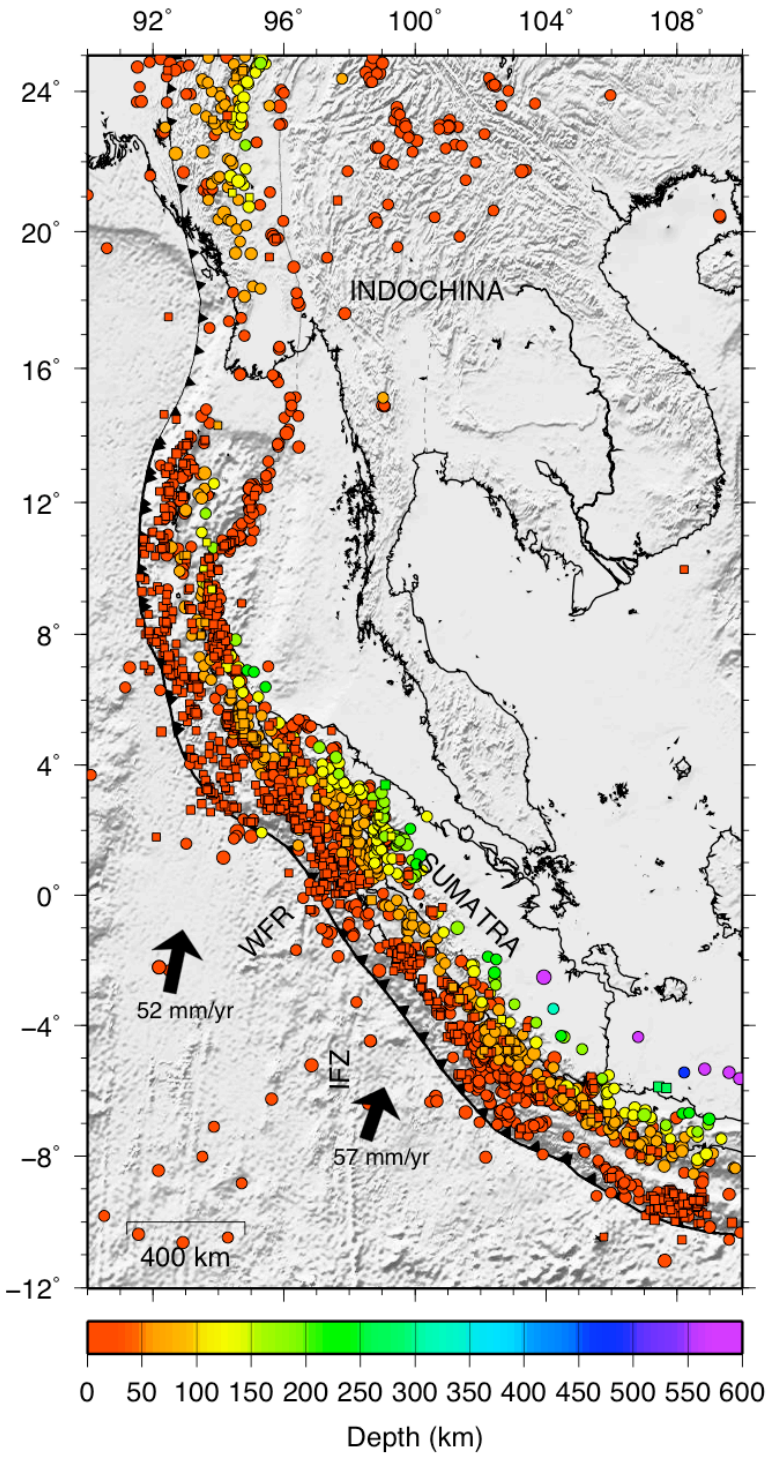

Figure 4.1. Distribution of EHB M5+ earthquakes (1964-2007) relocated in this study. Circles are events prior to the 2004 great earthquake and squares are events that occurred after it. Also shown are the Investigator Fracture Zone (IFZ) and Wharton Fossil Rift (WFR).

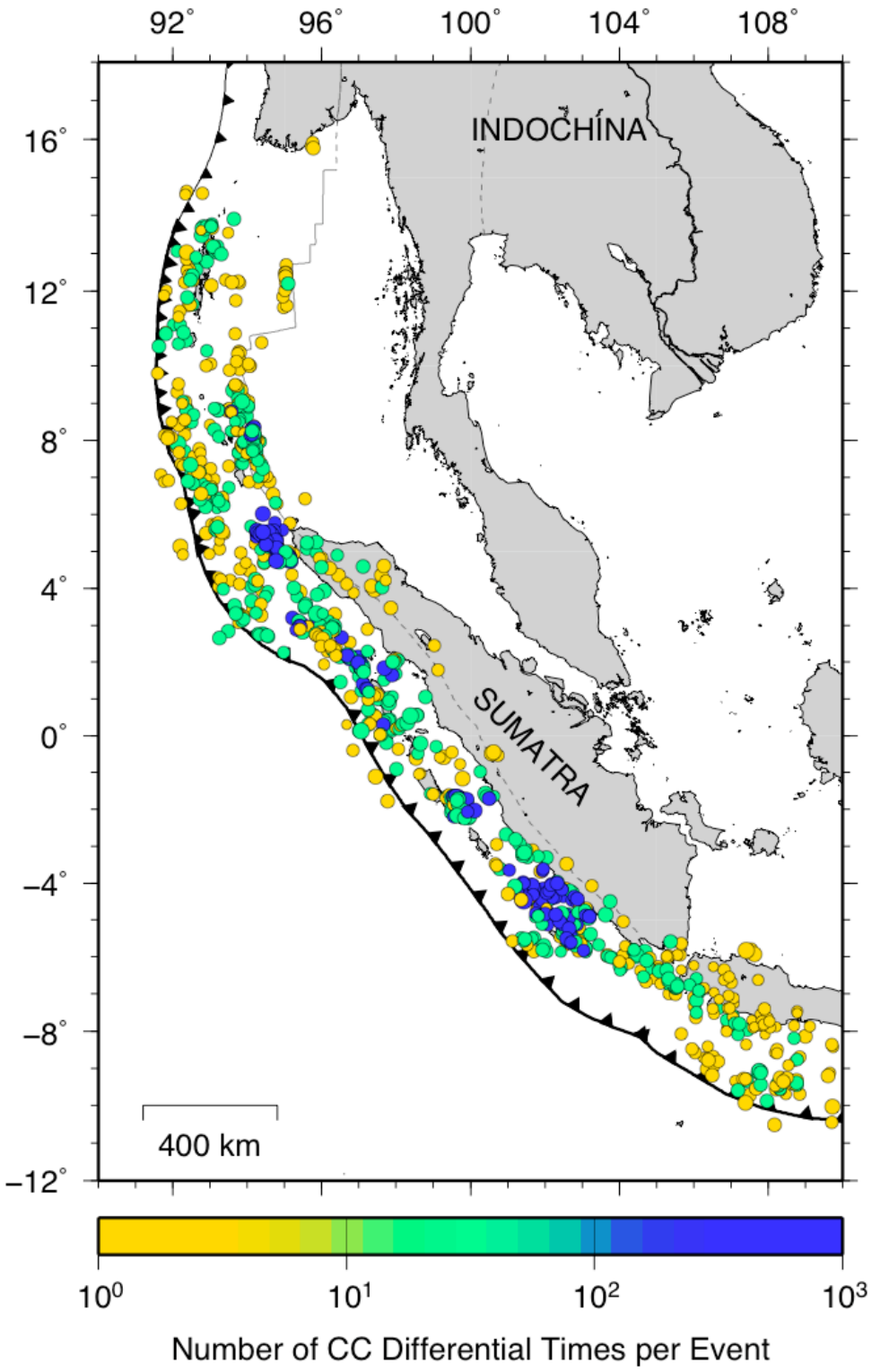

Figure 4.2. Distribution of ~1200 events for which Cross-correlation (CC) data are available.

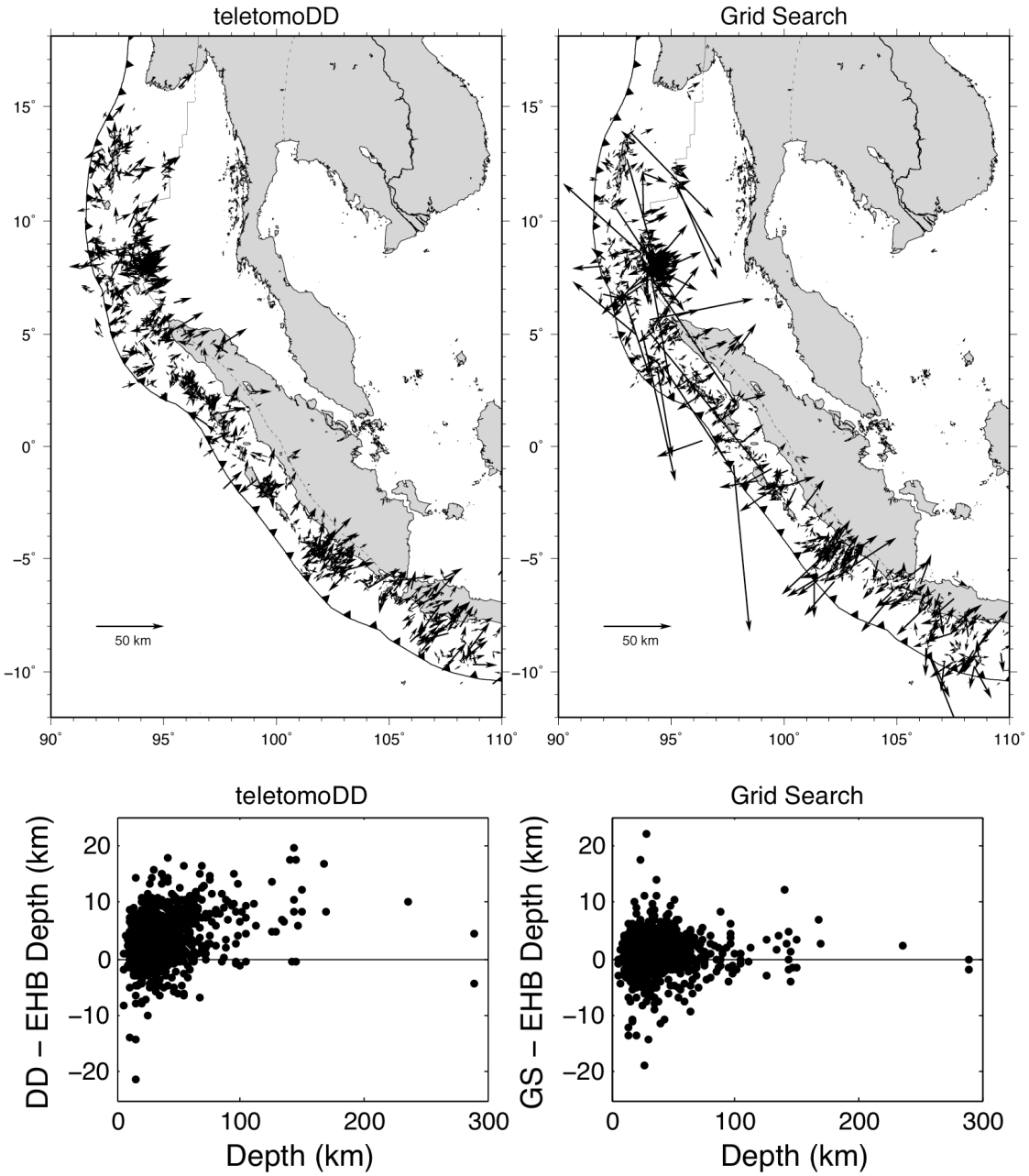

Figure 4.3. Epicenter shifts and depth comparisons relative to EHB locations for the events in Figure 4.2, determined by our DD method (left) and our grid search (GS) method (right). For both sets of relocations, epicenters show a trend of NW migration. The changes in depth, plotted as the difference between the relocated depth and the EHB depth at various depths, indicate that our relocated hypocenters are consistently shallower than the EHB depths. Note the scaling of the location difference vectors, which are ~8x magnified.

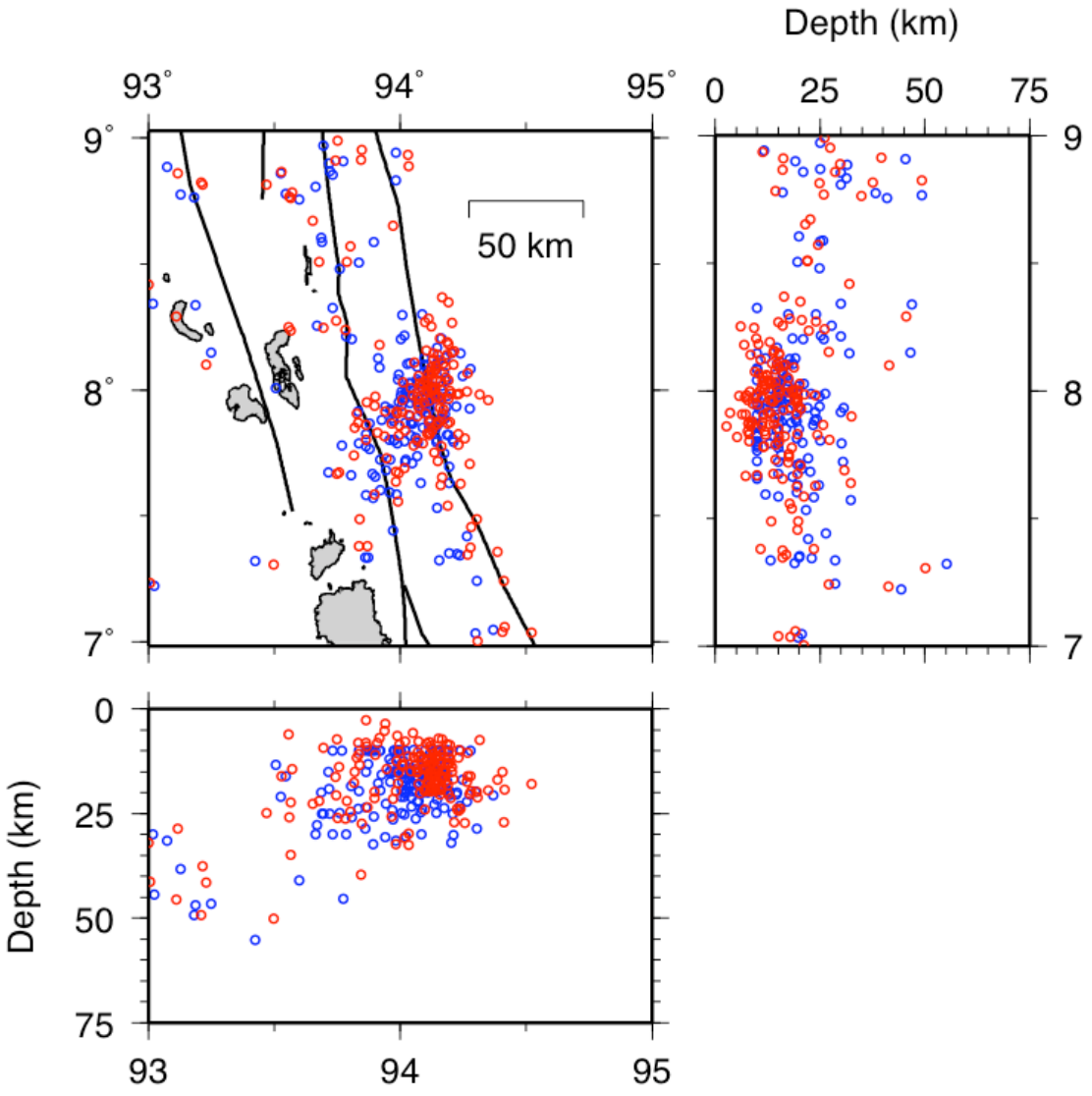

Figure 4.4. Comparison of EHB (blue) and DD (red) locations for a large cluster of events beneath the Andaman Sea illustrating the NW epicenter migration and the shallower depths of the DD relocations. Fault locations (black lines) are from Curray [2005].

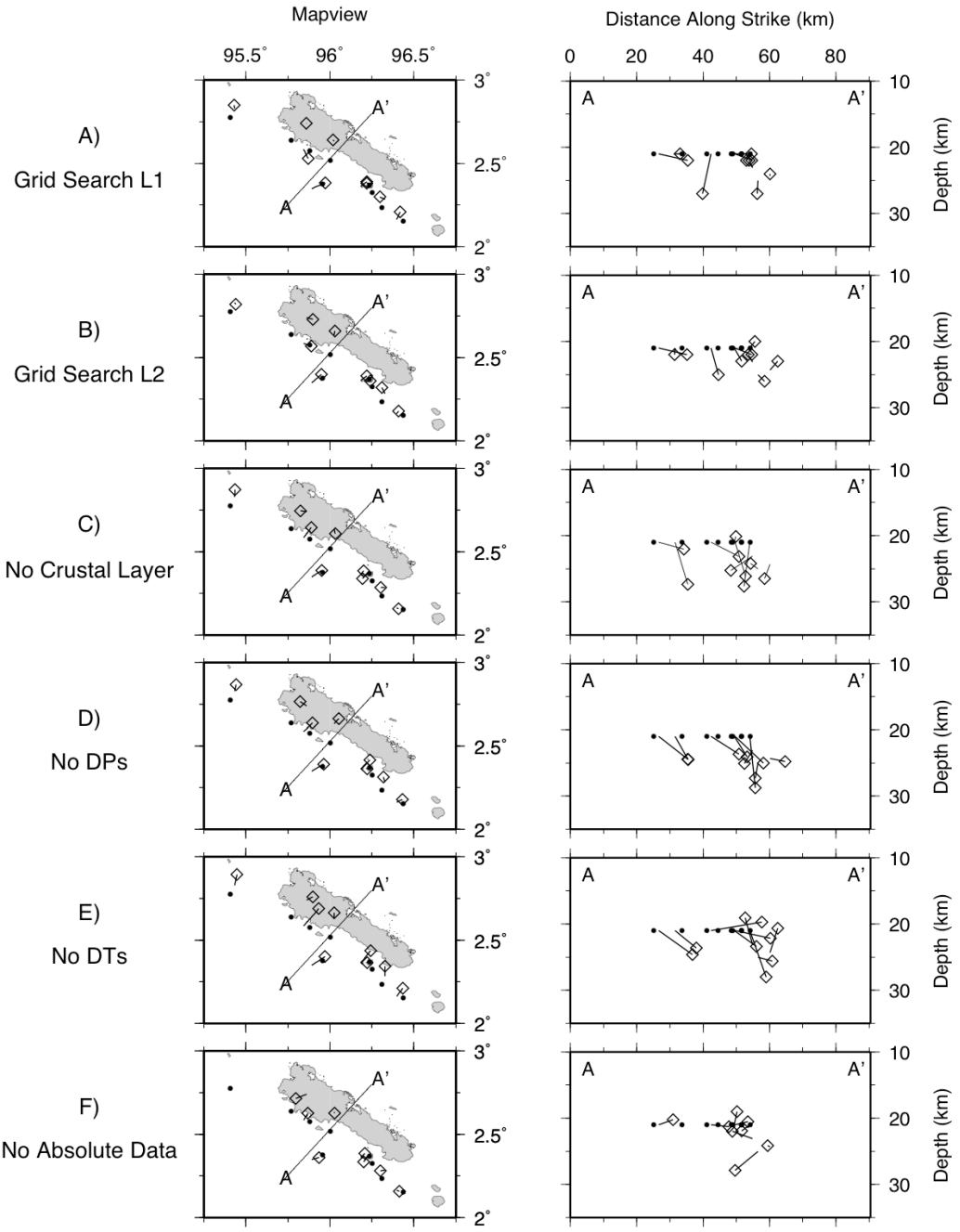

Figure 4.5. Comparison of DD relocation results for 9 events that were also located by OBS stations (circles) [Tilmann et al., 2006]. Lines from the EHB locations to the new DD relocations (diamonds) show the changes in locations for various methods and data types. A) grid search relocations where the L1-norm was minimized and B) where the L2-norm was minimized. C) DD relocations when the crustal layer (CRUST 2.0; Bassin et al. 2000) is excluded from the 3-D model used for ray tracing, D) when relocation is performed excluding all depth phase data, E) when all differential times are excluded, and F) when all absolute data are excluded.

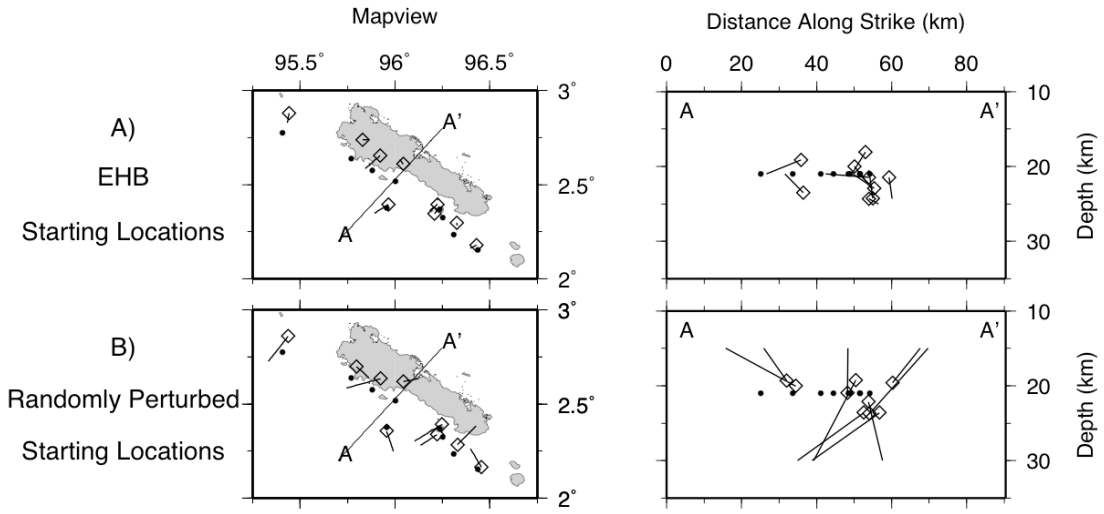

Figure 4.6. DD relocations for 9 events in Figure 4.5 when all data types except the OBS phases are included, for A) the EHB locations determined with OBS data, and B) randomly perturbed EHB locations. The results demonstrate the stability of the relocations, and the ability of *teletomoDD* to properly constrain focal depth (see discussion in text).

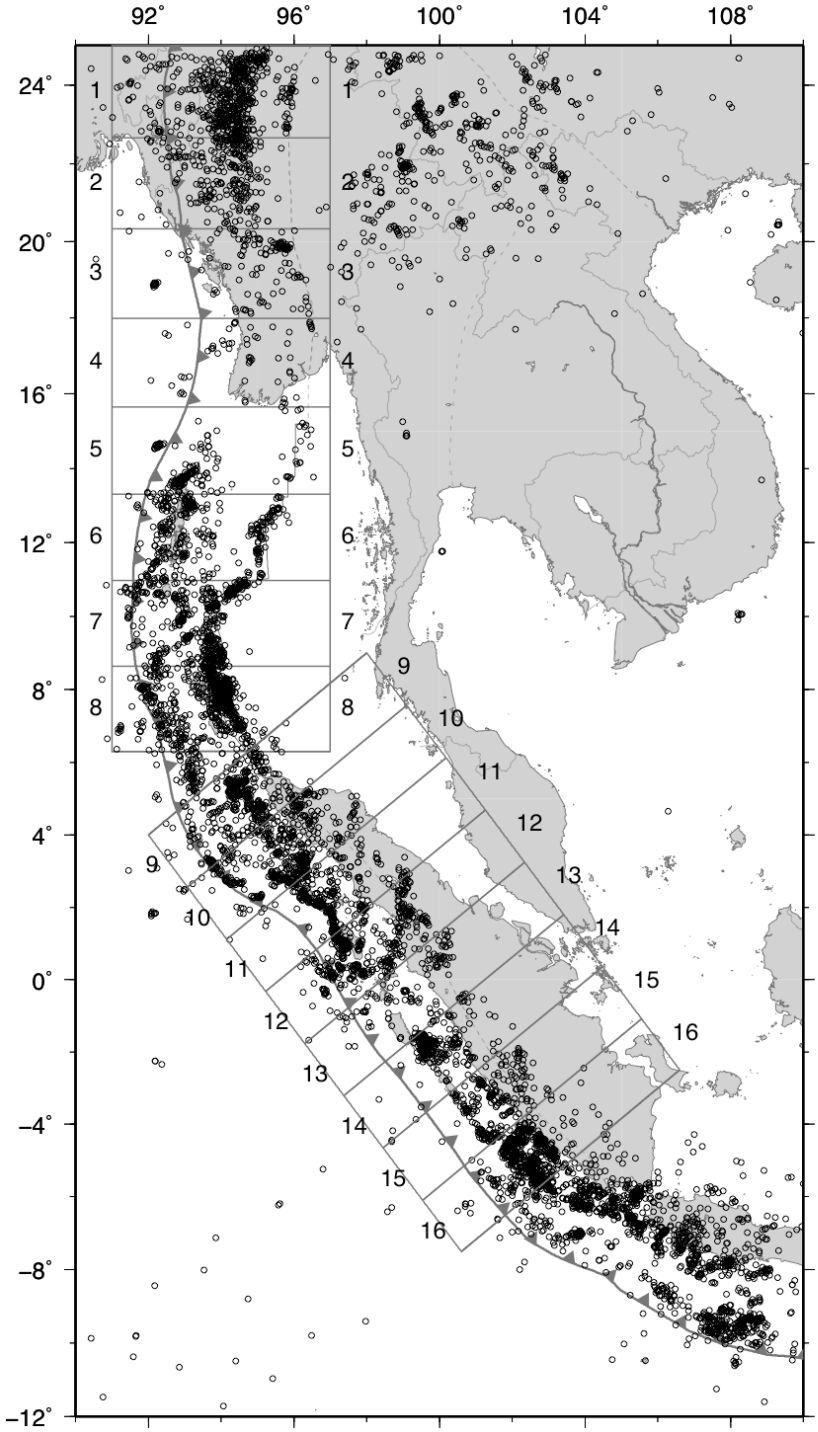

Figure 4.7a. Map view of DD relocations for the entire EHB catalog of ~8600 events. Cross-section locations for Figures 4.7b, 4.7c, and 4.8 are also shown.

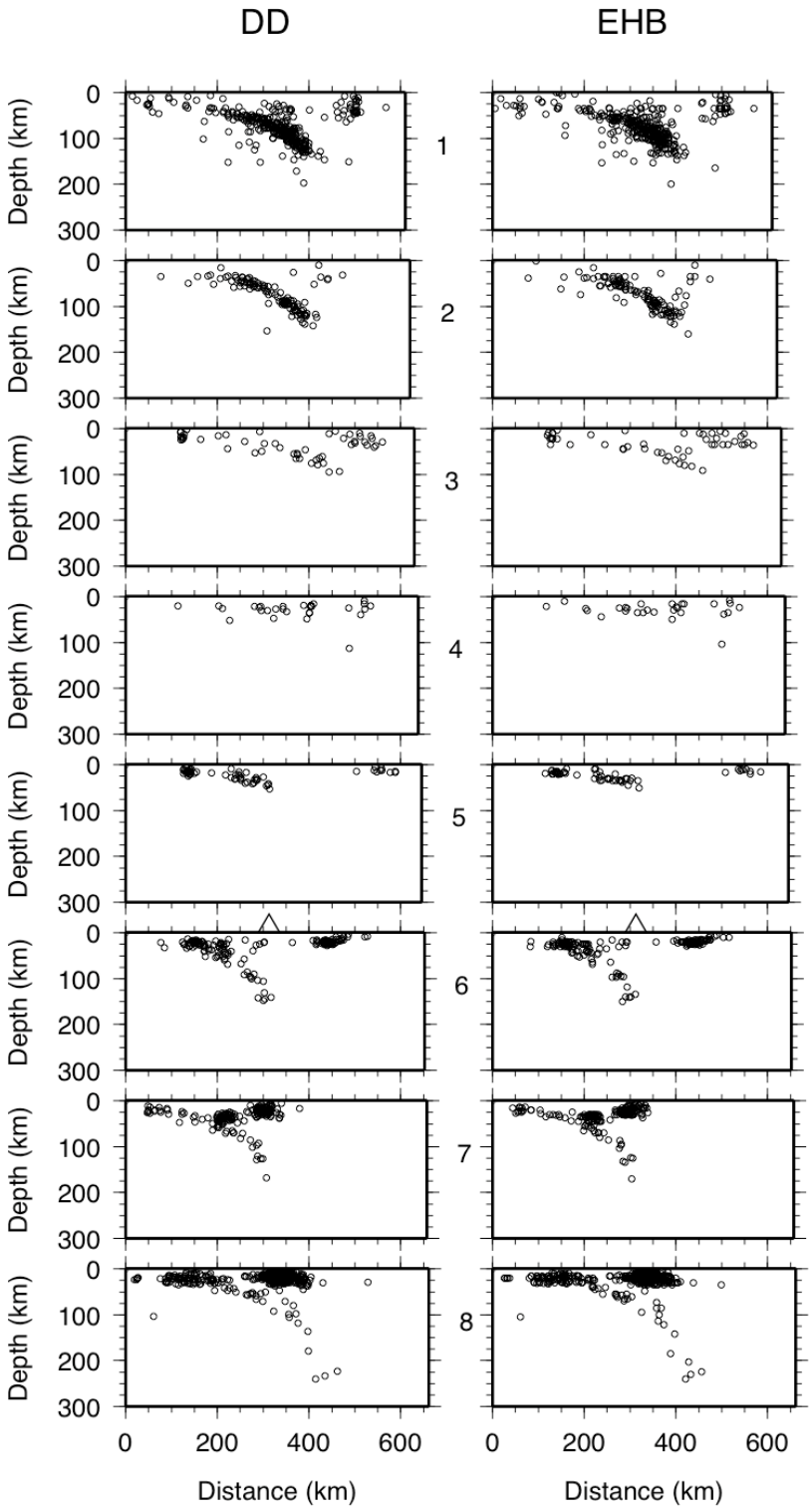

Figure 4.7b. Comparison of DD and EHB locations for cross-sections 1-8 shown in Figure 4.7a.

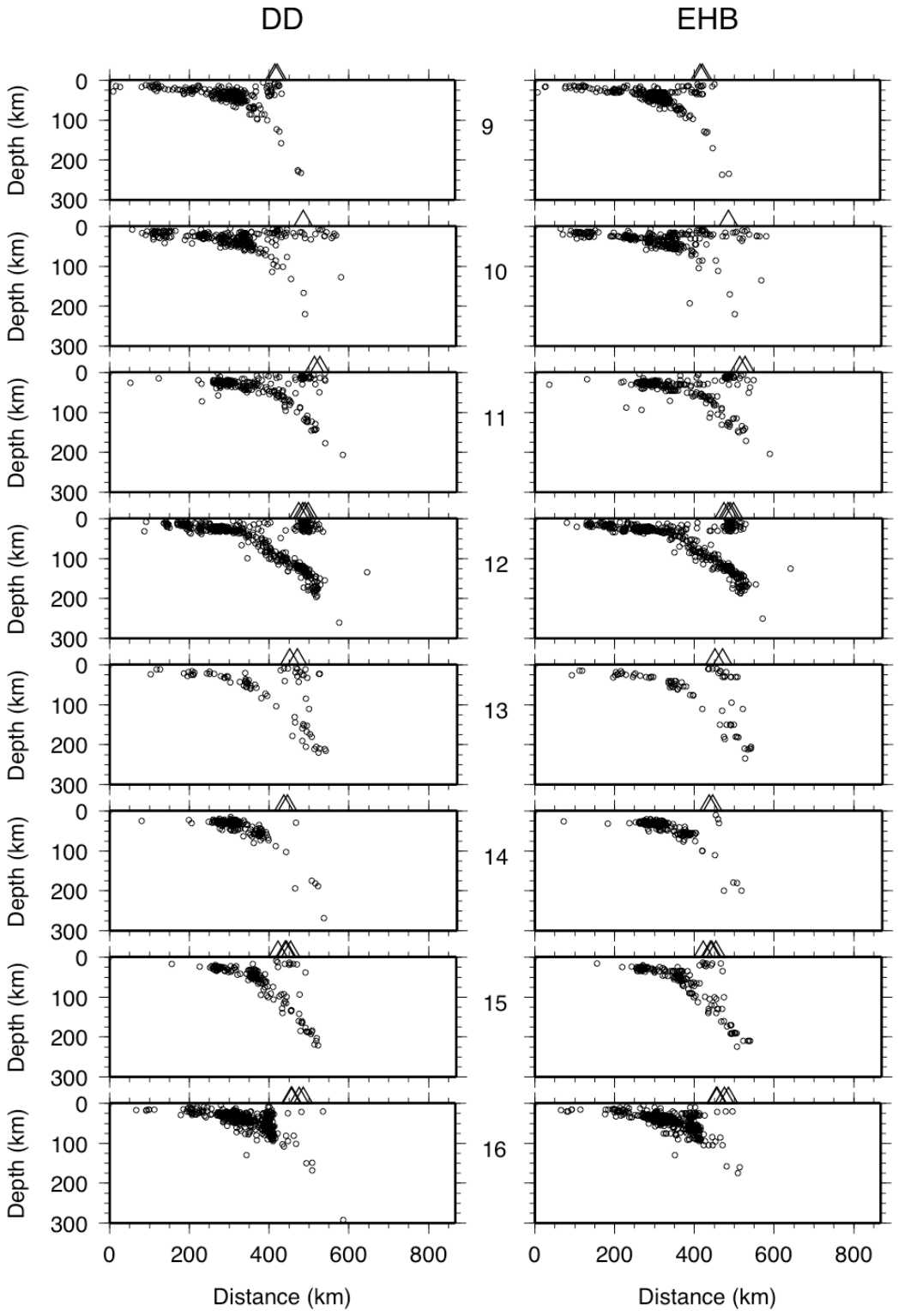

Figure 4.7c. Comparison of DD and EHB locations for cross-sections 9-16 shown in Figure 4.7a.

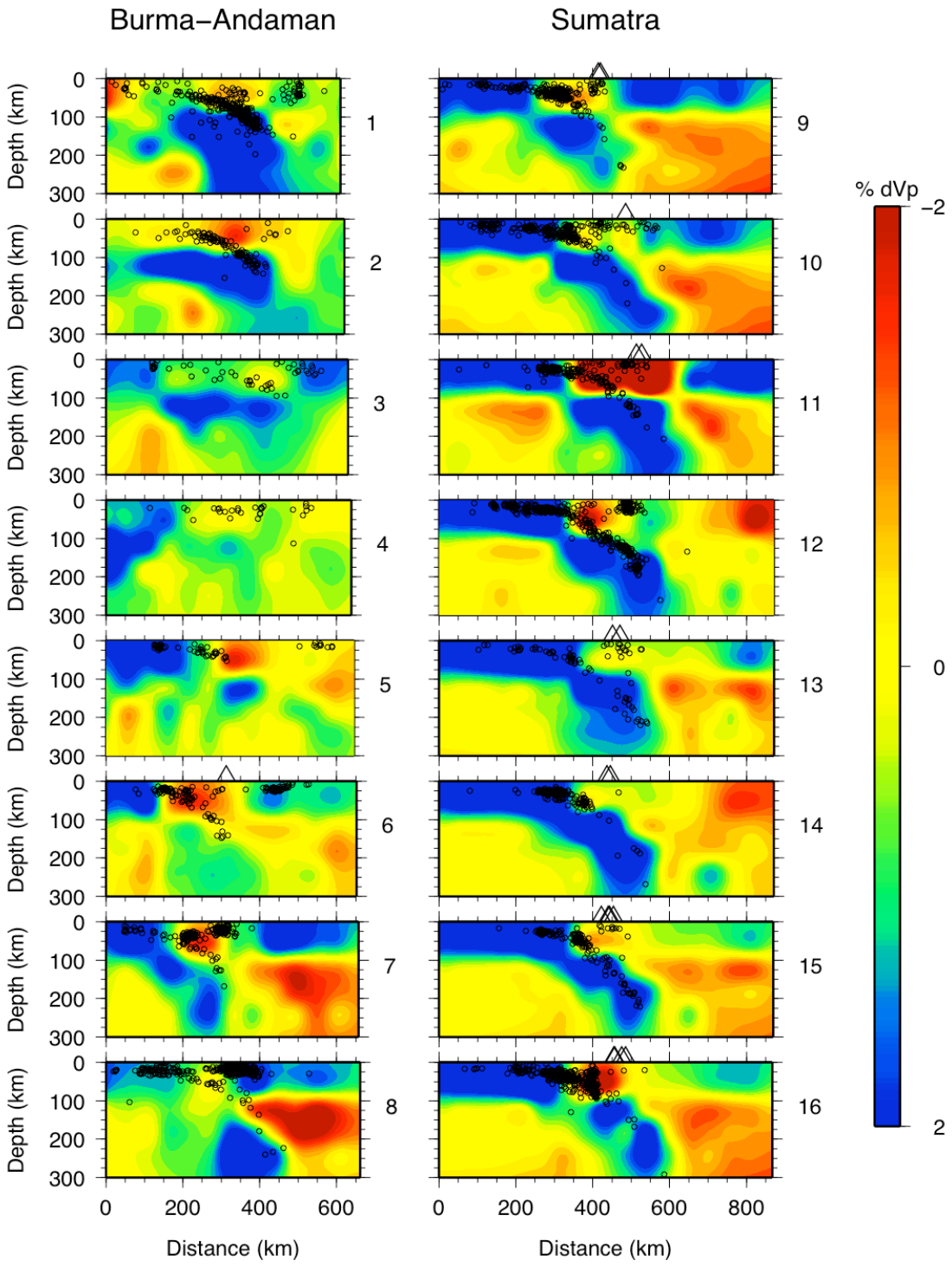

Figure 4.8. DD relocations for all sections shown in Figure 4.7a overlain on the Vp model of Pesicek et al. [2008], shown as velocity perturbation relative to the reference model. Volcano positions within each box are shown as black triangles.

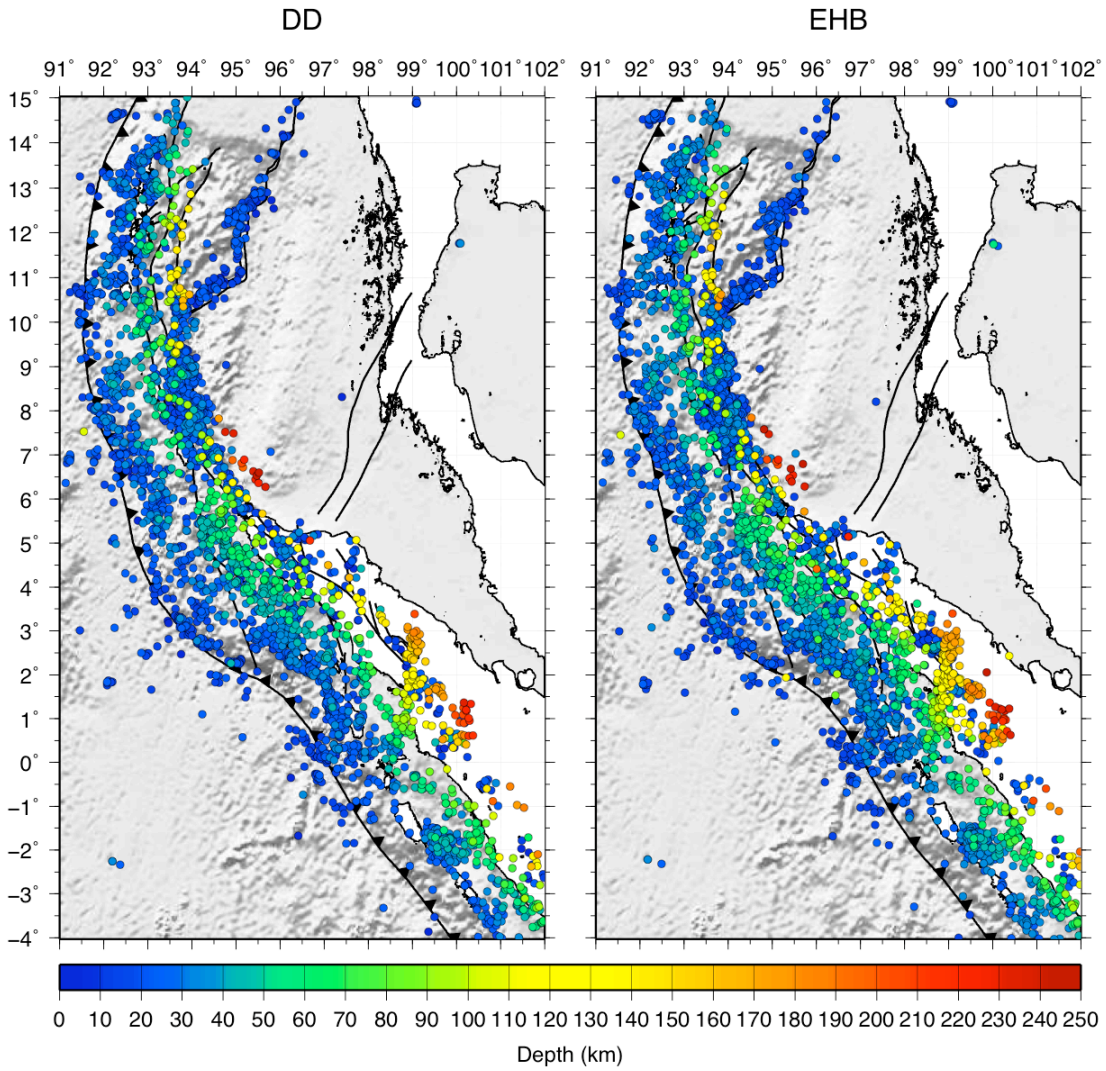

Figure 4.9. DD and EHB locations for the region surrounding the bend in the trench and the rupture areas of the 2004 and 2005 great earthquakes. Fault locations (black) are from Curray [2005].

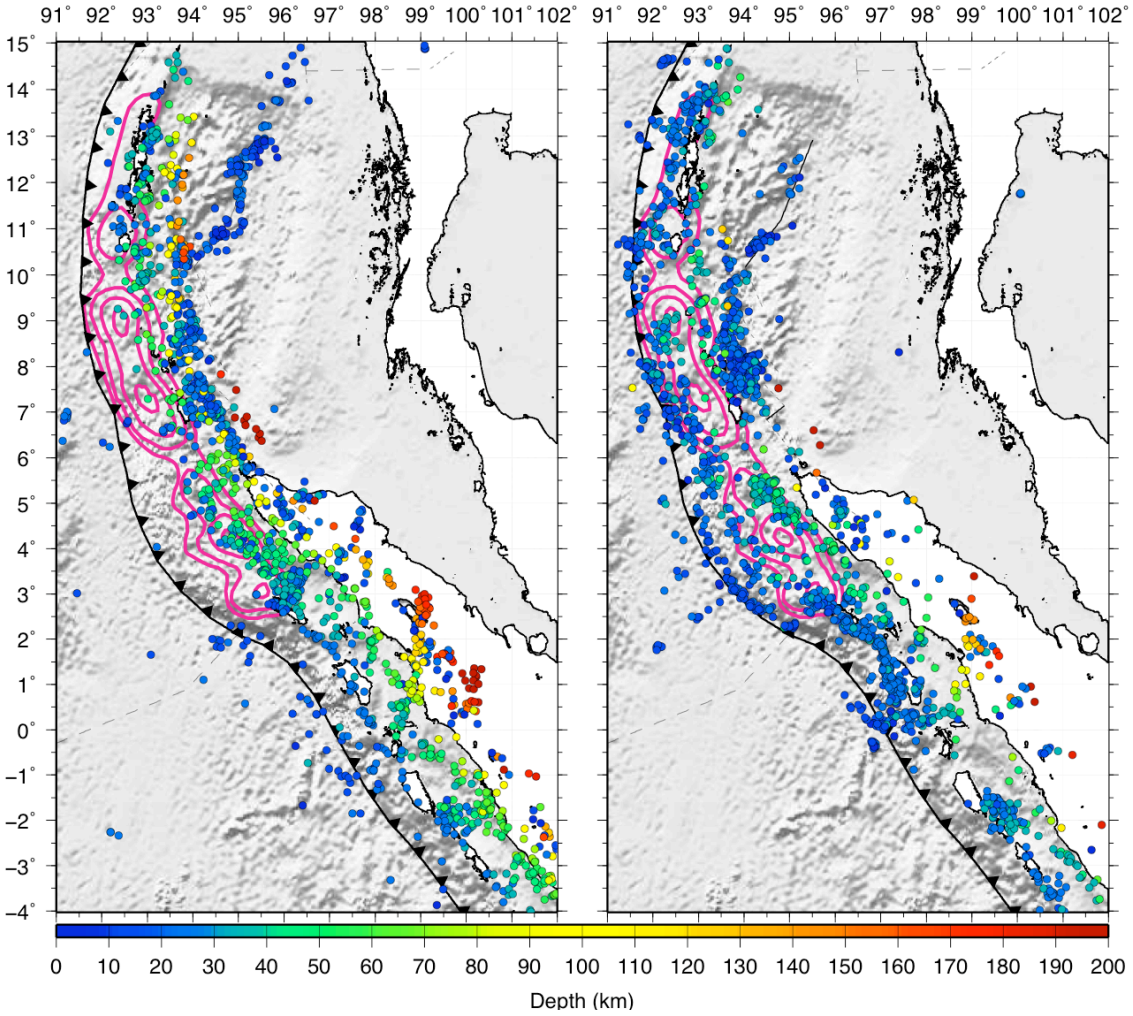

Figure 4.10. Map of event locations prior to the 2004 M9 event (left) and after (right) relative to coseismic slip from the event [Chlieh et al., 2007], plotted at 5 m contours (magenta). Aftershocks of the 2004 event show good correlation with regions of low coseismic slip while seismicity prior to the event occurs mostly downdip of the coseismic slip.

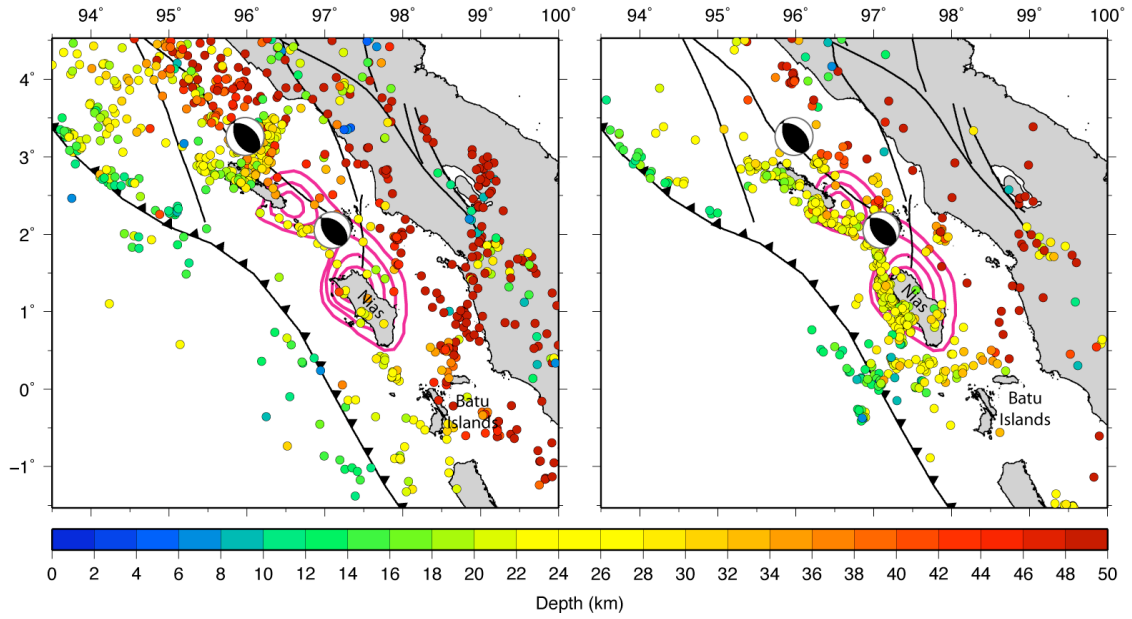

Figure 4.11. Map of megathrust events occurring before (left) the 28 March 2005 M8.7 Nias Island Earthquake and after (right). The relocations reveal a curvilinear feature on the megathrust that became seismically active after the 2005 event and shows an orientation similar to that of the trench; in addition it is highly correlated with the boundaries of coseismic slip (magenta; 2 m contour interval) of the 2005 event [Hsu et al., 2006]. CMTs for the 2004 and 2005 events are also shown. Faults positions (black) are modified from Curray [2005].

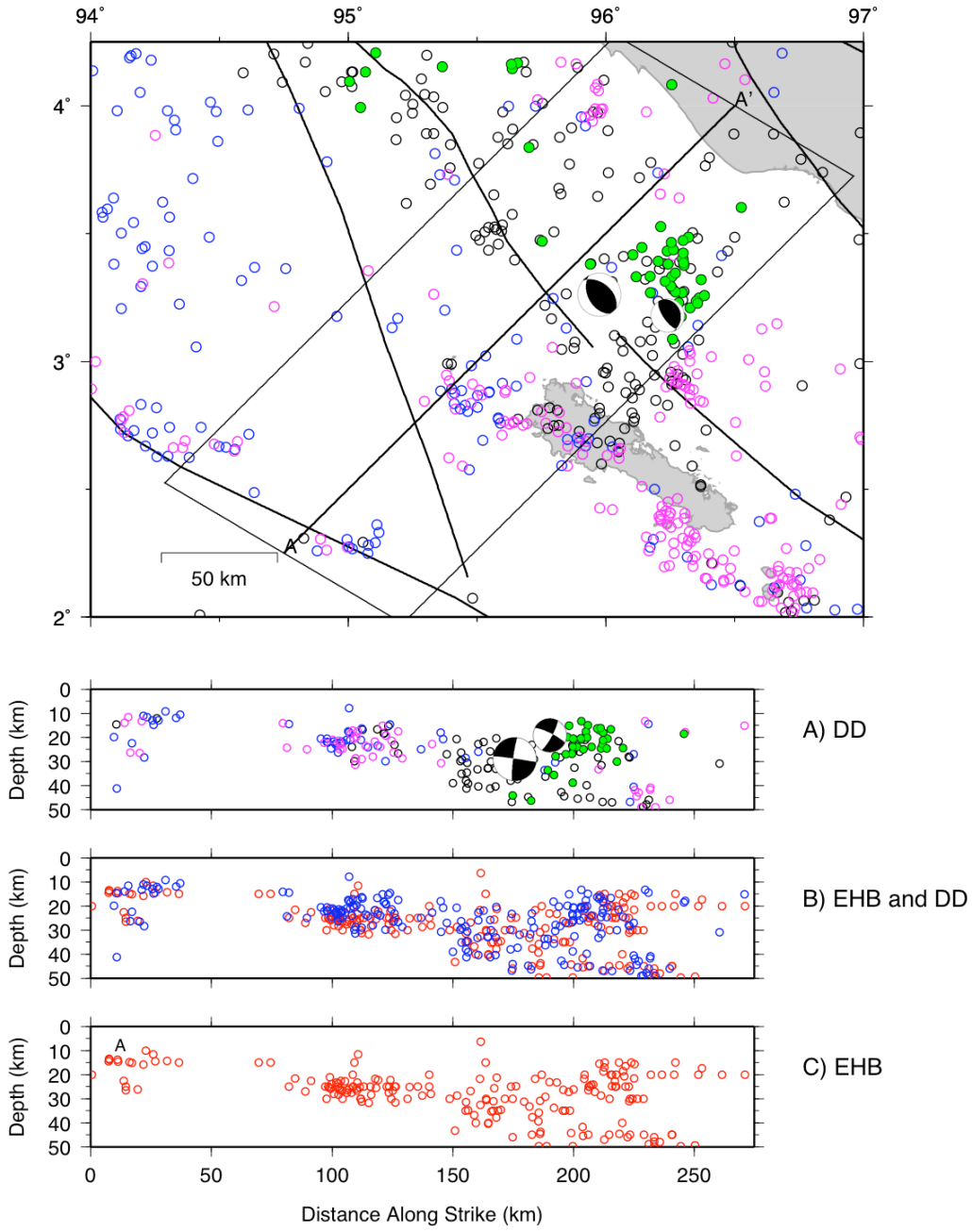

Figure 4.12. Relocations of events near Simeulue Island and the 2004 great earthquake. Top) mapview relocations for events before the 2004 event (black), after the 2004 event but before the 2005 event (blue), and after the 2005 event (magenta). CMT solutions for the 2004 M9 and the 1976 M7 events are also shown. Aftershocks of the 1976 event are shown in green. Events within the box are projected onto line A-A' and shown in cross-section A. Fault locations (black) are from Curray [2005]. Cross-sections B) and C) show depth comparisons of DD (blue) and EHB (red) locations. The DD relocations generally show shallower depths. Relocations of the 1976 M7 event and its aftershocks (top; green) indicate that they may locate on a backthrust in the region.

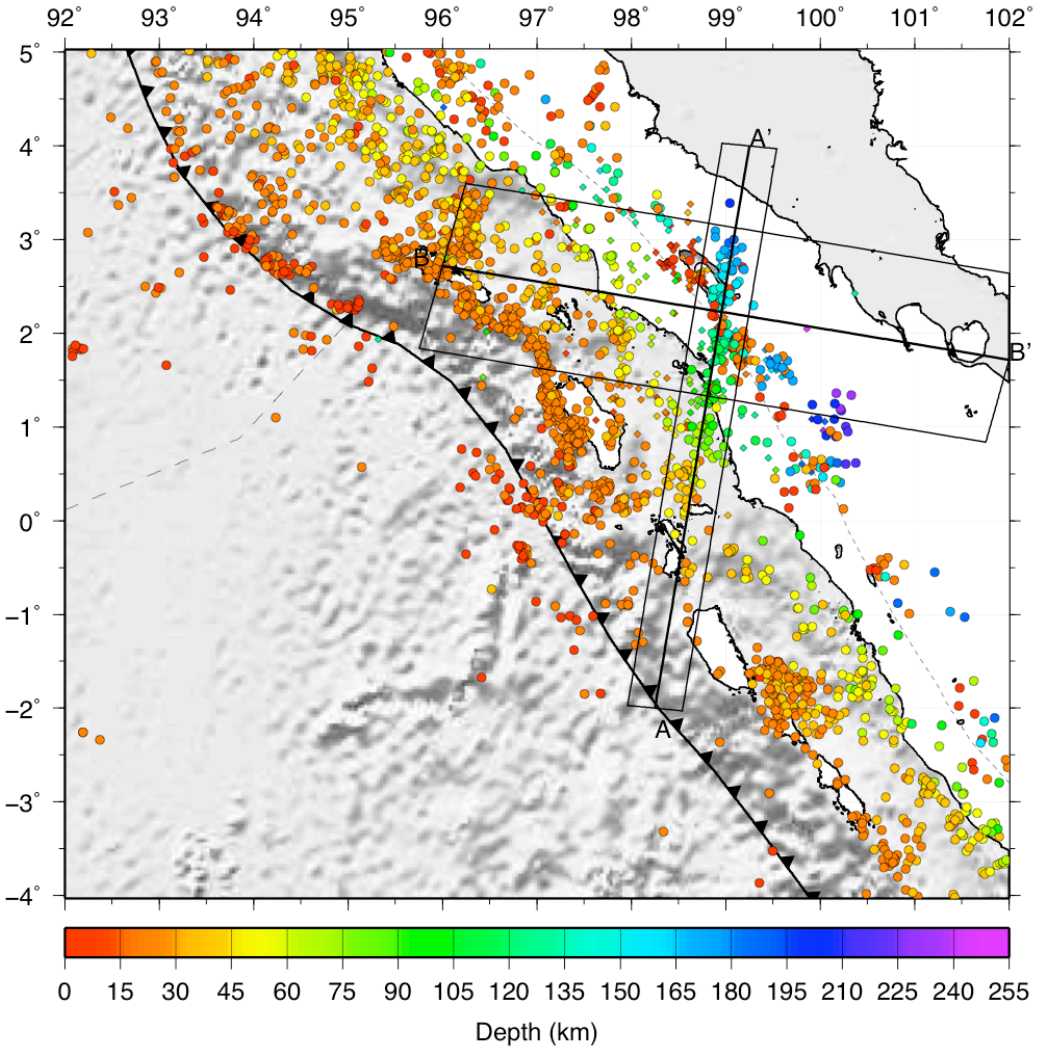

Figure 4.13a. Locations for cross-sections (Figure 4.13b) parallel and perpendicular to the seismicity associated with the location of the IFZ. In addition to the DD relocations also shown in Figure 4.9, smaller diamonds are plotted for local earthquakes recorded and located by Fauzi et al. [1996].

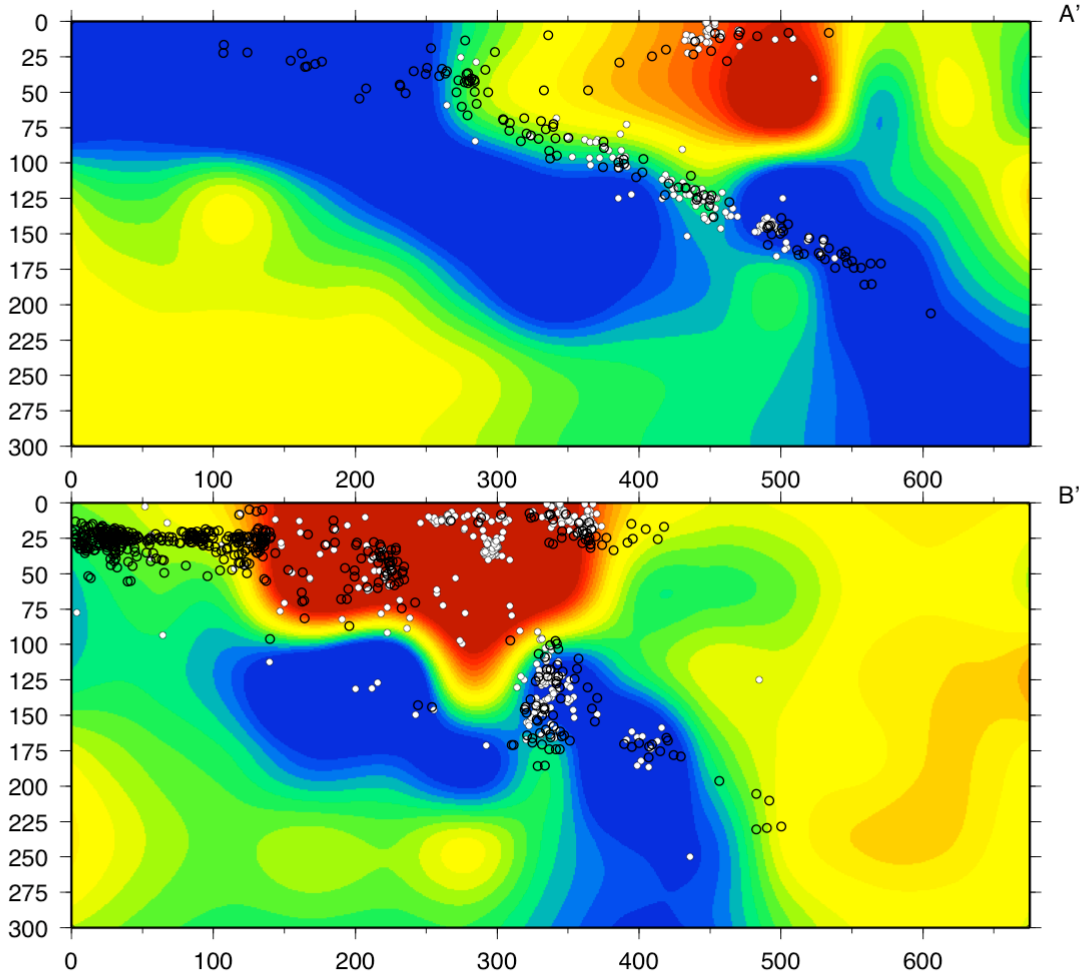

Figure 4.13b. Cross-sections (locations shown in Figure 4.13a) parallel (top; A) and perpendicular (bottom; B) to the location of the IFZ, showing teleseismic DD locations (black open circles) and local seismicity recorded by Fauzi et al. [1996] (white circles) overlain of the tomography model of Pesicek et al. [2008b] (Velocity scale shown in Figure 4.8). The bottom cross-section (B-B') shows an apparent offset in the slab that correlates with seismicity on the IFZ.

CHAPTER 5: Constraining the Shallow Density Structure of the Sumatra-Andaman Region using Satellite-Derived Gravity Data

J.D. Pesicek, C.H. Thurber, T.L. Masterlark, and M.F. Asgharzadeh

Abstract

Spherical prism gravity modeling of the region surrounding the rupture area of the 2004 Sumatra-Andaman great earthquake has been conducted to better constrain the regional three-dimensional (3-D) density structure for Finite Element Modeling (FEM) of deformation due to this event. A starting density model is constructed based on previous 1-D FEM designs and its gravity effects are computed and compared to GRACE-derived satellite gravity data. Iterative forward modeling and inverse factor analysis of the starting density model are conducted in attempts to better fit the observed gravity. By incorporating known regional geologic features not included in previous FEM configurations, we are able to sufficiently match the long-wavelength features of the observed gravity and significantly reduce the misfit relative to the starting model. This improvement exceeds that obtained in the factor analysis by nearly a factor of 2. Adjustments to the original FEM design for these features, which include thinned crust associated with the Andaman backarc-spreading center, low-density sediments of the

Bengal fan, and thickened crustal roots below Burma and the Malay Peninsula, should improve the accuracy of future FEM designs.

5.1 Introduction

The 26 December 2004 Mw 9.1 and the 28 March 2005 Mw 8.7 Sumatra-Andaman earthquakes are among the largest ever recorded in the instrumental era, providing a unique opportunity to investigate subduction megathrust and seismogenic zone processes using modern techniques. The location of these events and their aftershocks along a remote and sparsely instrumented archipelago (Figure 5.1), however, limits the amount of local data available for precise geophysical studies. Consequently, analyses of remotely sensed data are the primary means of investigating the tectonic environment where these two great earthquakes occurred. Several recent studies have taken advantage of satellite-derived gravity data obtained by NASA's Gravity Recovery and Climate Experiment (GRACE) to successfully measure the time-dependent gravity response of the 2004 great Sumatra earthquake [*Han et al.,* 2006; *Ogawa and Heki,* 2007; *Panet et al.,* 2007]. In this study, we use a static gravity model constructed from GRACE gravity measurements to constrain the density structure of the region surrounding the rupture of the 2004 megathrust event.

Although three-dimensional (3-D) density models by themselves are quite useful for better understanding subduction zone structures, our density constraints are also directly applicable to Finite Element Modeling (FEM) of the region [*Masterlark and Hughes,* 2008] that seeks to match surface displacement fields and better explain deformation caused by the 2004 great earthquake. We have constructed a 3-D density model whose calculated gravity effects agree well with a recent model of the observed mean gravity determined from GRACE measurements. Our results can be transferred

and integrated into the FEM mesh, thus providing more accurate density constraints on which to base future generations of FEMs of the Sumatra-Andaman subduction zone.

5.2 Gravity Data

The gravity model that we have used in this study is the GRACE derived model GGM02c [*Tapley et al.,* 2005]. GGM02c is a freely available, global mean Earth gravity model that was generated from 363 days of GRACE measurements from April 2002 to December 2003. The satellite-derived model (GGM02), complete to spherical harmonic degree and order 160, was combined with terrestrial gravity data to degree and order 200, and extended to degree and order 360 using coefficients from the EGM96 model [*Lemoine et al.,* 1998]. In addition to the spherical harmonic coefficients, global gravity anomaly values are conveniently available in grid format at 30-minute resolution. Gravity anomalies in GGM02c are computed as the difference between the gravity on the geoid and normal gravity on the ellipsoid and are presented in Figure 5.2, as the region's free air gravity anomaly map.

Free air anomalies in Figure 5.2 are well correlated with topographic and bathymetric features (Figure 5.1). The mass distribution due to these features reveals very little about the density structure at megathrust depths and thus is of little interest to us. We therefore applied a Bouguer correction to the data as $g_B = 2\pi G\rho h$, where G is the universal gravitational constant, ρ is the density, and h is the height relative to mean sea

level (MSL). The density that is most commonly applied in a Bouguer correction is 2670 kg/m^3, representing average continental granitic rock. We applied this density to 0.5ºx0.5º elevation grid points [*Smith and Sandwell,* 1997] throughout the region, a resolution consistent with that of GGM02c.

The Bouguer correction is common in gravity analysis of onshore data. After applying this correction to topographic features, we obtained a Bouguer anomaly map onshore, while leaving offshore data as free air anomalies (Figure 5.3). Anomalies in this map are very similar to a previously published gravity map of Sumatra based on onshore surveys and older satellite data offshore for the areas that overlap [*Milsom and Walker,* 2005]. This comparison provides an independent check on our processing and the general agreement between maps testifies to the quality of the new GRACE derived model. In addition, this consistency between maps shows that the freely available global GRACE data are a good substitute for more regional terrestrial gravity data, which are privately held and thus not readily accessible.

Gravity analyses in subduction zone settings are commonly performed using a Bouguer anomaly map onshore and a free air anomaly map offshore (Figure 5.3) [e.g. *Tasarova,* 2007]. However, strong correlations with bathymetry remain in Figure 5.3, masking the deeper crustal signal that is our primary interest. We therefore applied the Bouguer correction to the offshore data as well, effectively replacing the water column with an equivalently sized rock column of average crustal density (Figure 5.4). We tested using higher densities in areas offshore to better represent oceanic crustal density but found the difference in the resulting anomaly pattern to be negligible. We therefore

applied a density of 2670 kg/m^3 in the Bouguer correction uniformly throughout the study area. The application of the Bouguer correction to areas on and offshore essentially eliminated contributions from surface topography and bathymetry and produced a gravity signal due only to density variations within a uniform volume whose surface starts at MSL. Displaying the observed gravity in this way greatly simplifies our construction of a density model to match it without compromising our goal of constraining density variations surrounding the rupture zone on the megathrust.

Figure 5.4 shows the Bouguer anomaly map (onshore and offshore) for the region surrounding the 2004 great earthquake rupture area. In the Andaman Sea region, the anomalies correlate quite well with the mantle Bouguer anomalies calculated by Radhakrishna et al. [2008]. These gravity anomalies and the anomalous mass that they represent are our primary interest; they are the features that we seek to match by forward calculation of the gravity due to our density model. Figure 5.4 still shows some correlations with the topography and bathymetry (Figure 5.1) despite these corrections; some areas of high topography have relatively low gravity anomalies while some areas of low bathymetry have relative high gravity anomalies. However, this correlation is not unexpected [e.g. *Blakely,* 1996]. Onshore, the topography-correlated anomalies are likely indicative of the low-density crustal roots that support these topographic structures. Offshore, deep bathymetric features may represent areas of thinned oceanic crust balanced by more dense material beneath. Thus, the remaining correlation gives insight into the subsurface density structure, and a density model that fits the pattern of Bouguer anomalies in the region must account for these types of features.

5.3 Forward Gravity Calculation

Potential field theory defines the contribution to the gravitational potential dP_{OS} at point *O* of a differential mass dm_S located at a point *S* a distance R_{OS} away from *O* as

$$dP_{OS} = G\frac{dm_S}{R_{OS}} = G\frac{\rho_S dv_S}{R_{OS}} \tag{5.1}$$

where *G* is the universal gravitational constant, ρ_S is the density and dv_S is an element of volume. The vector gravity field is obtained by taking the spatial vector gradient of (5.1). For an extended body of mass in a volume, the potential becomes

$$P_O = G\int_V \frac{\rho_S dv_S}{R_{OS}} \tag{5.2}$$

and the gravity field components can be obtained by

$$g_O = G\int_V \nabla\left(\frac{\rho_S dv_S}{R_{OS}}\right) \tag{5.3}$$

[*Asgharzadeh et al*., 2007]. In geophysical studies, arbitrarily shaped bodies are approximated in various ways for computation of their gravity field components. One such way is to approximate an extended body by a distribution of equivalent point sources (EPS) [e.g. *Ku,* 1977; *von Frese et al*., 1981a]. Another common approach is to divide the body into many polygonal pieces whose gravity effects are straightforward to compute directly [e.g. *Talwani and Ewing,* 1960]. Often, irregular bodies of mass are

approximated by a distribution of rectangular prisms [e.g. *Nagy,* 1966; *Banerjee and Das Gupta,* 1977]. If the prisms are small enough, then the gravity field can be accurately calculated for any arbitrarily shaped 3-D model.

Although rectangular prisms are commonly used to approximate regional model volumes [e.g. *Maceira and Ammon,* 2009], satellite-derived gravity data are more properly analyzed in terms of spherical coordinates. Thus, spherical prisms are more appropriate for gravity analyses of regional swaths of the earth. One method of determining the scalar potential (5.2) and vector gravity field (5.3) due to a spherical prism is to represent it by a set of EPS optimally distributed within the prism and use Gauss-Legendre quadrature (GLQ) integration to compute an approximate solution [*Asgharzadeh et al.,* 2007]. This method is advantageous because it avoids the difficulties of solving (5.2) and (5.3) analytically in spherical coordinates and forgoes the formidable book-keeping tasks that arise when transferring analytic solutions for the gravity effects of a rectangular prism [e.g., *Talwani and Ewing,* 1960; *Nagy,* 1966] to spherical coordinates [*von Frese et al.,* 1981b]. The EPS approximation and the GLQ formulation have been shown to work well as long as the distance between nodes is smaller than the distance to the observation point [*Ku,* 1977; *von Frese et al.,* 1981a; *Asgharzadeh et al.,* 2007]. The result is a more accurate representation of the gravity field due to a given regional mass distribution. In this study, we apply GLQ integration to compute the radial component of the gravity field caused by our regional density model.

5.4 Density Model Construction and Adjustment

The primary goal of our gravity modeling is to better constrain the 3-D density structure of the region so that deformation models of the 2004 great Sumatra earthquake can be based on a more accurate 3-D material property distribution. The geometry of recent FEM models of the region surrounding the rupture area (Figure 5.5) [*Masterlark and Hughes,* 2008] are based on interpretations of 2D cross-sections of gravity and seismic models [*Kieckhefer et al*., 1980; *Kieckhefer et al*., 1981; *Kopp et al*., 2002; *Kopp and Kukowski,* 2003] and the local geology of northern Sumatra [*Barber et al*., 2005]. The FEM is based on seven different rock types representing the various geologic units of an oceanic island arc setting (Table 5.1). Average densities for representative rock types [*Wang,* 2000; *Turcotte and Schubert,* 2002] have been propagated along strike throughout a much larger region to fill the elements of the FEM. Thus, the FEM mesh does not currently match 3-D structural complexity along strike throughout the region, most notably the Andaman Sea back arc spreading center.

We have used the FEM density distribution of Masterlark and Hughes [2008] to construct a starting density model. The FEM is comprised of 339,810 elements of various sizes with an average volume of 13,225 km^3. In order to compute the gravity effects of this irregular FEM using the GLQ spherical prism method, some alteration of the FEM mesh was necessary. We interpolated the element centroids of the FEM to a regular grid of density nodes whose values were computed as a weighted average of the densities of the elements closest to that node, with a weight proportional to the volume of the elements. We then computed density anomalies relative to the Preliminary Earth

Reference Model (PREM) [*Dziewonski and Anderson,* 1981], and constructed constant density spherical prisms with dimensions 0.5º x 0.5º horizontally and 10 km thick, centered on the new grid nodes. This process created smooth density gradients where sharp unit boundaries exist in the FEM, but this effect is unavoidable and does not significantly affect the overall consistency of the two models. The resulting density model and its gravity effects provide both a good starting point for gravity analysis and allow a first order assessment of the accuracy the FEM density distribution (Figure 5.6b).

5.4.1 Factor Analysis

Masterlark and Hughes [2008] adapted density values for the seven geologic units included in the FEM (Table 5.1) based on average densities of representative rock types. In order to test the sensitivity of the forward gravity calculation to changes in these densities, we conducted a factor analysis [*Menke,* 1989] of the unit densities in the starting model. The observed gravity can be thought of as a linear combination of the gravity effects of each of the different geologic units. The misfit (Δg) between the observed gravity and the gravity calculated from the starting model at any observation point j can be expressed in terms of density perturbation of each rock unit at that point plus an offset term (μ) that accounts for the average misfit between the two models

$$\Delta g^j = \sum_{i=1}^{7} \delta_i^j \Delta\rho_i + \mu \ . \tag{5.4}$$

Each of the seven terms in the summation in (5.4) is composed of the density perturbation $\Delta\rho$ of rock unit i multiplied by a term δ that represents the change in the calculated gravity at j for a corresponding change in the density of unit i. For a unit change to the density, δ represents the derivative of the gravity with respect to rock unit density. We formed δ for each rock unit at every point by reducing the unit's density by 100 kg/m^3, forward calculating the gravity from this perturbed model, subtracting off the gravity calculated from the starting model, and then rescaling by 100 kg/m^3. We repeated this for each rock type to obtain seven vectors composed of the partial derivatives of the gravity with respect to the seven rock densities at each observation point in the model.

To solve for the optimal adjustment to the densities of the seven rock types and the average model misfit, we applied (5.4) throughout the region to form a set of equations

$$\Delta g = D\Delta\rho \tag{5.5}$$

where D is the matrix comprised of the seven δ column vectors plus an eighth column of ones and $\Delta\rho$ represents an 8-element solution vector of seven rock unit density changes plus the average offset (μ). We applied damping to (5.5) as

$$\begin{bmatrix}\Delta g\\ 0\end{bmatrix} = \begin{bmatrix}D\\ \lambda I\end{bmatrix}\Delta\rho \tag{5.6}$$

where I is the identity matrix and λ is the damping parameter whose value was determined via a trade off analysis. We set λ=3 and solved the system of equations (5.6) by least squares.

The solution to our factor analysis (Table 5.1) suggests that a significant portion of the misfit between the gravity observations and those calculated from our starting model can be accounted for by relative inaccuracies in the densities of the seven geologic units. After obtaining $\Delta\rho$, we computed $D\Delta\rho$ to obtain a forward prediction of the misfit due to the determined density perturbations. This calculation suggests that our solution should produce a misfit reduction of 40%. Thus, by modifying the seven starting geologic unit densities by the results of this factor analysis (i.e. applying the density perturbations from Table 5.1) prior to further refinement of the model, we should be able to obtain an improved starting model with a significantly reduced misfit. However, our solution (Table 5.1) yields unrealistically large perturbations to the rock densities. For example, the solution suggests unreasonably extreme densities of 3515 kg/m^3 for the continental mantle unit and 2163 kg/m^3 for the backarc basement. Thus, despite yielding a misfit reduction of 34% compared to the original FEM-based model, we have chosen not to adopt the factor analysis solution and instead prefer to make manual, geologically based adjustments to the density model.

5.4.2 Manual Model Adjustment

Comparison of the starting density model and its gravity effects (Figure 5.6) with the observed Bouguer gravity (Figures 5.4, 5.6b) reveals several salient discrepancies. First, Figure 5.6b is rather smooth with low gradients relative to Figure 5.4. This can be attributed to the interpolation and gridding of the FEM that was required to produce the regular grid of density nodes. To correct this, we manually adjusted the densities west of

the trench, where this effect is largest, to be more uniform and representative of average oceanic crust, and to create a sharper density contrast at the trench. Secondly, the ranges and means of the gravity values for the observed and calculated gravity are inconsistent. This suggests that we are not accurately modeling the absolute gravity signal in the region. One possible reason for this is that the model only extends to 50 km depth. Thus, density variations below this depth are neglected. However, limiting our model to 50 km depth decreases computation time while still encompassing all of the variations in the density structure near the megathrust that are likely to affect the FEM deformation calculations. In addition, we have tested the use of seismic tomography results [*Pesicek et al.,* 2008] and empirical velocity-density relations to extend our density model to mantle depths and found the effects of deep density anomalies to be negligible in the resulting gravity calculation and thus not worth the computational expense. Therefore, we have elected not to extend our model to greater depths.

Another possible reason for the offset between observed and calculated mean gravity is that the GLQ gravity calculation was formulated to compute absolute gravity at satellite altitudes, but we have used it to compute gravity anomalies at MSL (0 km altitude) relative to PREM. In contrast, GGM02c gravity anomalies are referenced to the geoid, not MSL. Either of these issues may partly be responsible for the discrepancy between the mean gravity of the two maps (Figure 5.4, 5.6a). In the factor analysis, we accounted for this discrepancy by solving for the average misfit directly. Here, we have simply removed the mean gravity from the model for comparison (Figure 5.7). Because

we are only interested in the relative distribution of densities and their resulting gravity anomalies, this difference in mean gravity is of little importance.

The remaining differences between the calculated (Figure 5.6b) and observed (Figure 5.4) gravity can be attributed to the simple FEM rock model inadequately simulating 3-D density variations in the region. We have shown above that adjustment of the FEM rock densities alone does not sufficiently reduce the misfit to the gravity observations without requiring unrealistic densities. However, a more formal inversion for density at each model node would be completely nonunique. Therefore, we prefer to make direct, geologically based adjustments to the starting model to better match the 3-D distribution of anomalies seen in Figure 5.4. In keeping with the goal of producing a realistic density model for use in future versions of the FEM, our strategy was to make only large-scale adjustments that address long-wavelength features of the observed gravity. Such adjustments can be based on *a priori* geologic knowledge of the region and can be confidently applied to the FEM configuration. Matching short wavelength features of the gravity observations would require ad hoc adjustment to the density model, which may actually decrease model accuracy. By limiting our adjustments to well known regional geologic features, we can limit model non-uniqueness while still greatly reducing the gravity misfit and improving the accuracy of the FEM density distribution.

Several simple first order adjustments to the starting density model have been made to create a model that matches the long wavelength features of the observed gravity (Figure 5.7) relatively well without introducing unnecessary complexity. The most

significant gravity anomaly discrepancy is that associated with the Andaman backarc spreading center. To better represent this feature of the gravity signal, we have inserted a high-density region in the model that roughly mimics the shape of the high gravity anomaly in the Andaman Sea (Figure 5.4). This anomaly can be explained by crustal thinning and/or underplating due to backarc spreading. Crustal material in the Andaman Basin has been thinned and replaced by denser mantle material from beneath. Radhakrishna et al. [2008] also included thinned crust in their density model of the Andaman region.

In addition to the thinned Andaman crust, other lesser changes to the starting density model were necessary. To better fit the gravity data in the NE part of the study region, we thickened the crust below Burma and the Malay Peninsula by introducing a low-density root. This root compensates for the topographic load in this continental area. Another adjustment was necessary to account for sediments of the Bengal Fan [e.g. *Curray et al.,* 2002]. In the NW portion of the study area, we lowered the density west of the trench to account for the density contrast of these sediments relative to oceanic crust farther south. These three adjustments were sufficient to match long-wavelength features of the gravity and reduce the misfit by 63% (Figure 5.8). In addition, linear regressions of the observed gravity versus the gravity calculated for both the original FEM-based starting model and our new density model show an increase in the correlation coefficient from 0.55 to 0.74. Other minor adjustments were made to better place geologic rock units relative to tectonic features, but these changes are not due to any feature unaccounted for in the FEM configuration. Rather, these minor inconsistencies are

probably due either to distortions of the geologic unit geometry from conversion of the FEM mesh to the node-based density model, or to inaccurate position of the geologic units in the original FEM.

5.5 Summary

We have created a density model of the region surrounding the rupture area of the 2004 great Sumatra-Andaman earthquake that adequately matches the long wavelength features of the GGM02c gravity model. Our starting density model, based on a current FEM representation of the region, required only 3 regional adjustments to correct for 3-D structural complexity not accounted for in the 2D-based FEM design. The addition of 1) thinned crust in the Andaman Sea, 2) thicker crust below Burma and the Malay Peninsula, and 3) lower density Bengal fan sediments accounted for the majority of misfit between the starting model and the Bouguer gravity signal. Our new density model incorporating these three changes has a misfit reduction of 63% compared to the FEM-based starting model and a significantly increase correlation coefficient. Thus, by modifying the density structure of the areas of the FEM corresponding to the locations of these three features, future generations of the FEM can better honor 3-D geologic complexity and more accurately model the slip caused by the 2004 megathrust event.

References

Asgharzadeh, M. F., R. R. B. von Frese, H. R. Kim, T. E. Leftwich, and J. W. Kim (2007), Spherical prism gravity effects by Gauss-Legendre quadrature integration, *Geophys. J. Int., 169*, 1-11.

Banerjee, B. and S. P. Das Gupta (1977), Gravitational attraction of a rectangular parallelepiped, *Geophysics, 42*, 1053-1055.

Barber, A. J., M. J. Crow, and J. S. Milsom (2005), *Sumatra; Geology, Resources and Tectonic Evolution*, vol. 31, 290 pp., United Kingdom (GBR).

Blakely, R. J. (1996), *Potential Theory in Gravity and Magnetic Applications*, 441 pp., Cambridge University Press, Cambridge, United Kingdom (GBR), United Kingdom (GBR).

Coffin, M.F., L.M. Gahagan and L.A. Lawver, (1998), Present-day plate boundary digital data compilation. *University of Texas Institute for Geophysics Technical Report No. 174*, pp. 5.

Curray, J. R., F. J. Emmel, and D. G. Moore (2002), The Bengal Fan: morphology, geometry, stratigraphy, history and processes, *Mar. Pet. Geol., 19*, 1191-1223.

Dziewonski, A. M. and D. L. Anderson (1981), Preliminary reference Earth model, *Phys. Earth Planet. Inter., 25*, 297-356.

Han, S., C. K. Shum, M. Bevis, C. Ji, and C. Kuo (2006), Crustal dilatation observed by GRACE after the 2004 Sumatra-Andaman earthquake, *Science, 313*, 658-662.

Kieckhefer, R. M., G. F. Moore, and F. J. Emmel (1981), Crustal structure of the Sunda forearc region west of central Sumatra from gravity data, *J. Geophys. Res., 86*, 7003-7012.

Kieckhefer, R. M., G. G. Shor Jr, J. R. Curray, W. Sugiarta, and F. Hehuwat (1980), Seismic refraction studies of the Sunda Trench and forearc basin, *J. Geophys. Res., 85*, 863-889.

Kopp, H., D. Klaeschen, E. R. Flueh, J. Bialas, and C. Reichert (2002), Crustal structure of the Java margin from seismic wide-angle and multichannel reflection data, *J. Geophys. Res., 107*, 24.

Kopp, H. and N. Kubowski (2003), Backstop geometry and accretionary mechanics of the Sunda margin, *Tectonics, 22*, 16.

Ku, C. C. (1977), A direct computation of gravity and magnetic anomalies caused by 2- and 3-dimensional bodies of arbitrary shape and arbitrary magnetic polarization by equivalent-point method and a simplified cubic spline, *Geophysics, 42*, 610-622.

Lemoine, F. G., S. C. Kenyon, J. K. Factor, R. G. Trimmer, N. K. Pavlis, D. S. Chinn, C. M. Cox, S. M. Klosko, S. B. Luthcke, and M. H. Torrence (1998), The Development of the Joint NASA GSFC and the National Imagery and Mapping Agency(NIMA) Geopotential Model EGM 96, *NASA*.

Maceira, M. and C. J. Ammon (2009), Joint inversion of surface wave velocity and gravity observations and its application to central Asian basins shear velocity structure, *J. Geophys. Res., 114*, B02314.

Masterlark, T. and K. L. H. Hughes (2008), Next generation of deformation models for the 2004 M9 Sumatra-Andaman earthquake, *Geophys. Res. Lett., 35*, L19310.

Menke, W. (1989), *Geophysical Data Analysis: Discrete Inverse Theory*, Academic Press.

Milsom, J. S. and A. Walker (2005), The gravity field; Sumatra; geology, resources and tectonic evolution, *Memoirs of the Geological Society of London, 31*, 16-23.

Nagy, D. (1966), The gravitational attraction of a right rectangular prism, *Geophysics, 31*, 362-371.

Ogawa, R. and K. Heki (2007), Slow postseismic recovery of geoid depression formed by the 2004 Sumatra-Andaman Earthquake by mantle water diffusion, *Geophys. Res. Lett., 34*, L06313.

Panet, I., V. Mikhailov, M. Diament, F. Pollitz, G. King, O. de Viron, M. Holschneider, R. Biancale, and J. M. Lemoine (2007), Coseismic and post-seismic signatures of the Sumatra 2004 December and 2005 March earthquakes in GRACE satellite gravity, *Geophys. J. Int., 171*, 177-190.

Pesicek, J. D., C. H. Thurber, S. Widiyantoro, E. R. Engdahl, and H. R. DeShon (2008), Complex slab subduction beneath northern Sumatra, *Geophys. Res. Lett., 35*, L20303.

Radhakrishna, M., S. Lasitha, and M. Mukhopadhyay (2008), Seismicity, gravity anomalies and lithospheric structure of the Andaman arc, NE Indian Ocean, *Tectonophysics, 460*, 248-262.

Smith, W. H. F. and D. T. Sandwell (1997), Global sea floor topography from satellite altimetry and ship depth soundings, *Science, 277*, 1956-1962.

Talwani, M. and W. M. Ewing (1960), Rapid computation of gravitational attraction of three-dimensional bodies of arbitrary shape, *Geophysics, 25*, 203-225.

Tapley, B. et al. (2005), GGM02 - An improved Earth gravity field model from GRACE, *Journal of Geodesy, 79*, 467-478.

Tasarova, Z. A. (2007), Towards understanding the lithospheric structure of the southern Chilean subduction zone (36° S-42° S) and its role in the gravity field, *Geophys. J. Int., 170*, 995-1014.

Turcotte, D. L. and G. Schubert (2002), *Geodynamics*, 450 pp., Cambridge University Press, Cambridge, United Kingdom (GBR), United Kingdom (GBR).

von Frese, R. R. B., W. J. Hinze, L. W. Braile, and A. J. Luca (1981), Spherical-Earth gravity and magnetic anomaly modeling by Gauss-Legendre quadrature integration, *Journal of Geophysics = Zeitschrift fuer Geophysik, 49*, 234-242.

von Frese, R. R. B., W. J. Hinze, and L. W. Braile (1981), Spherical Earth gravity and magnetic anomaly analysis by equivalent point source inversion, *Earth Planet. Sci. Lett., 53*, 69-83.

Wang, H. F. (2000), *Theory of Linear Poroelasticity with Applications to Geomechanics and Hydrogeology*, Princeton Series in Geophysics, vol. 3, Princeton University Press, Princeton, NJ, United States (USA), United States (USA).

Table 5.1. Starting Density Values and Factor Analysis Solution

Geologic Unit	**Starting Density (kg/m^3)**	**Perturbation ($\Delta\rho$) (kg/m^3)**
Backarc Basement	2800	-637
Backarc Sediments	2450	-94
Continental Mantle	3250	265
Oceanic Mantle	3250	122
Forearc Sediments	2450	-105
Oceanic Crust	2950	-53
Volcanic Arc	2650	72

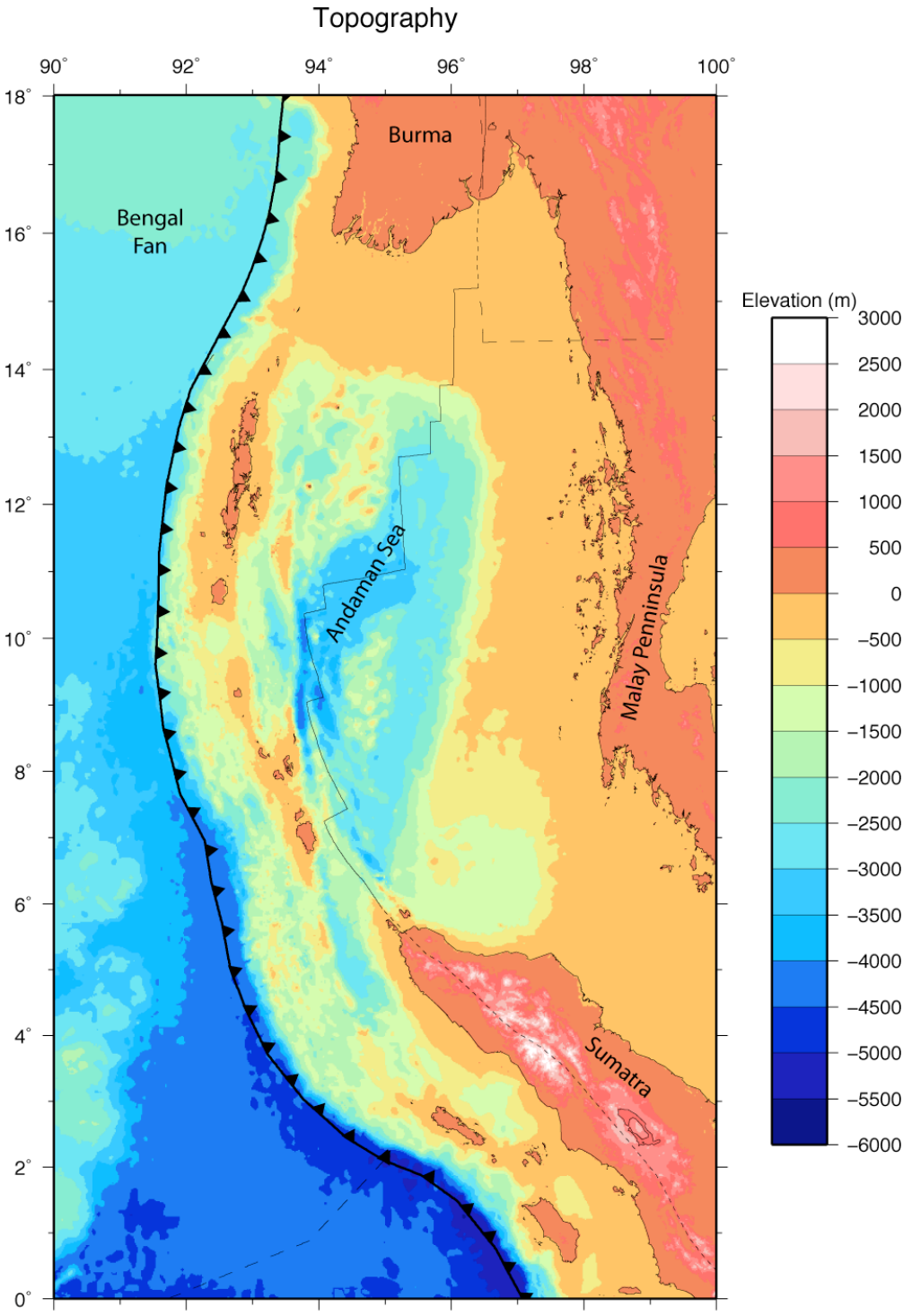

Figure 5.1. Map of topography and bathymetry [*Smith and Sandwell*, 1997], plate boundaries [*Coffin et al*., 1998], and geographic features.

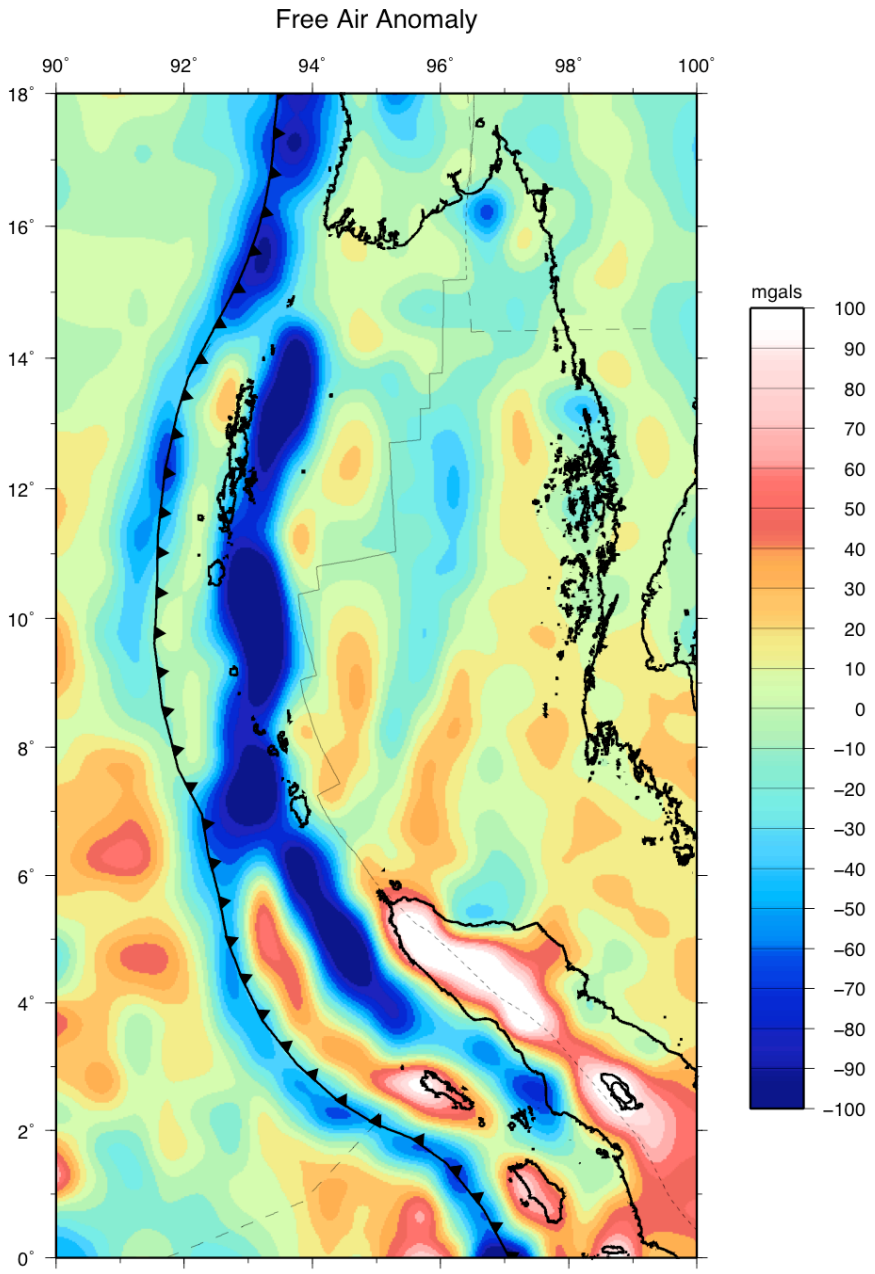

Figure 5.2. GGM02c [*Tapley et al*., 2005] gravity free air anomaly map for the Sumatra-Andaman region.

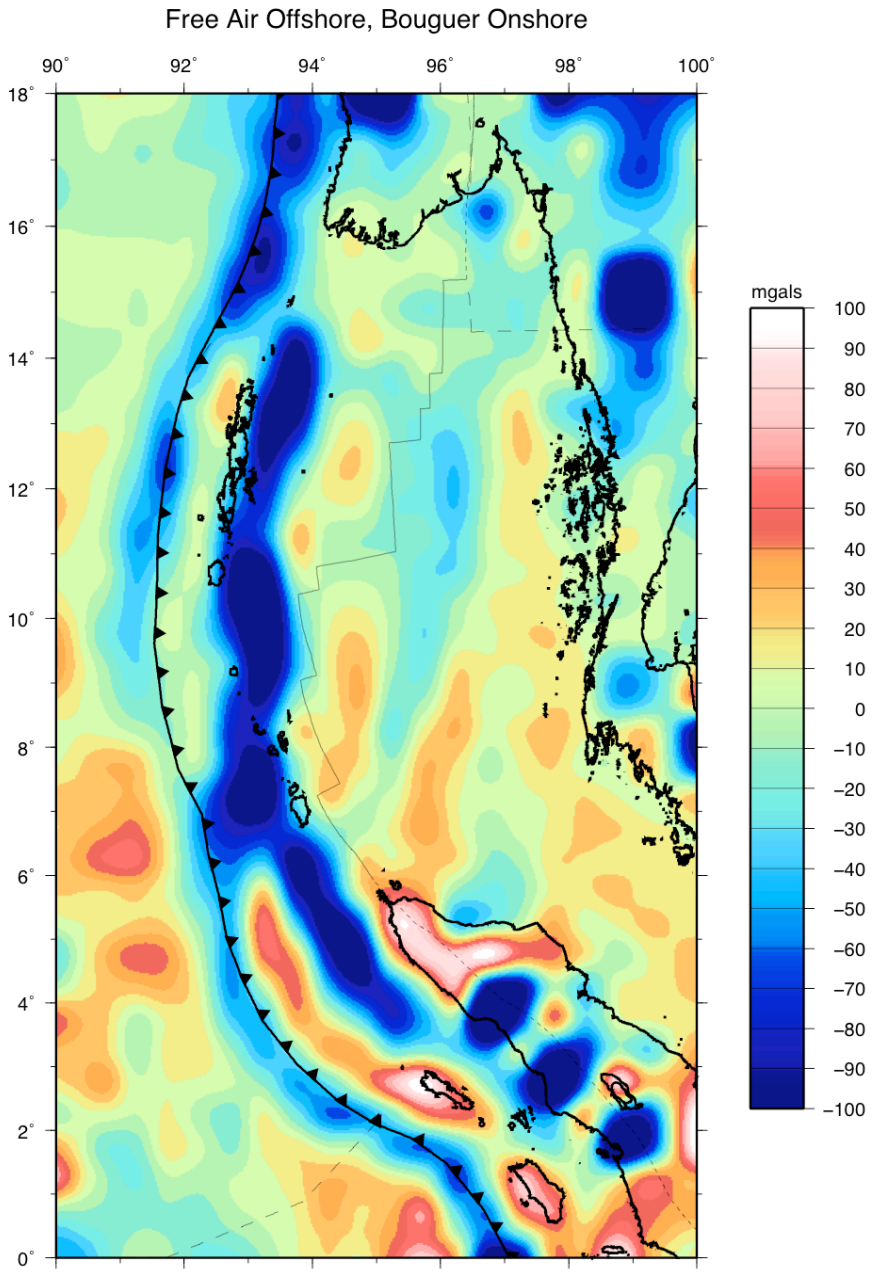

Figure 5.3. Gravity map showing free air anomalies offshore and Bouguer anomalies onshore.

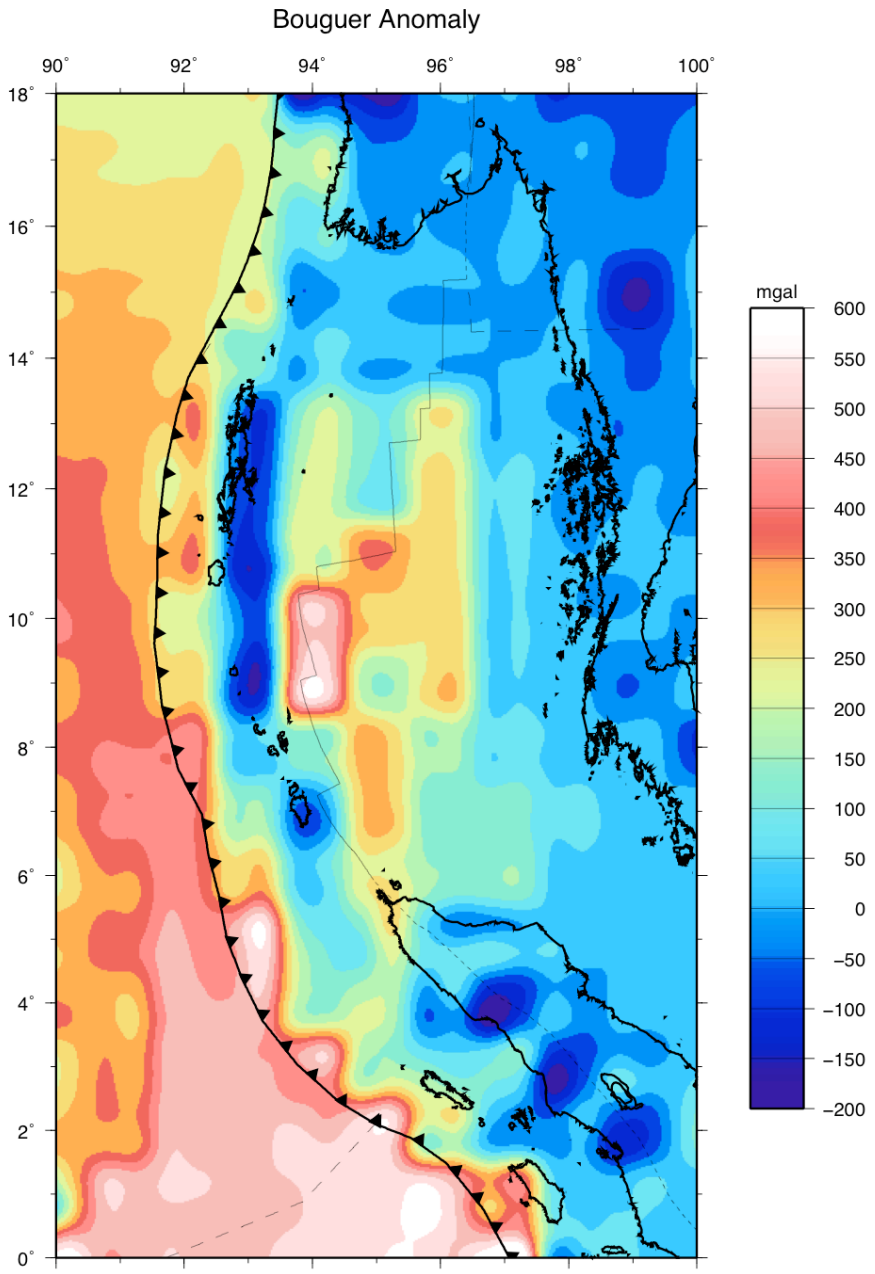

Figure 5.4. Map of Bouguer anomalies on- and offshore. For the Bouguer calculation offshore, the water column at every grid point is replaced with an equivalent thickness of rock of density 2670 kg/m^3.

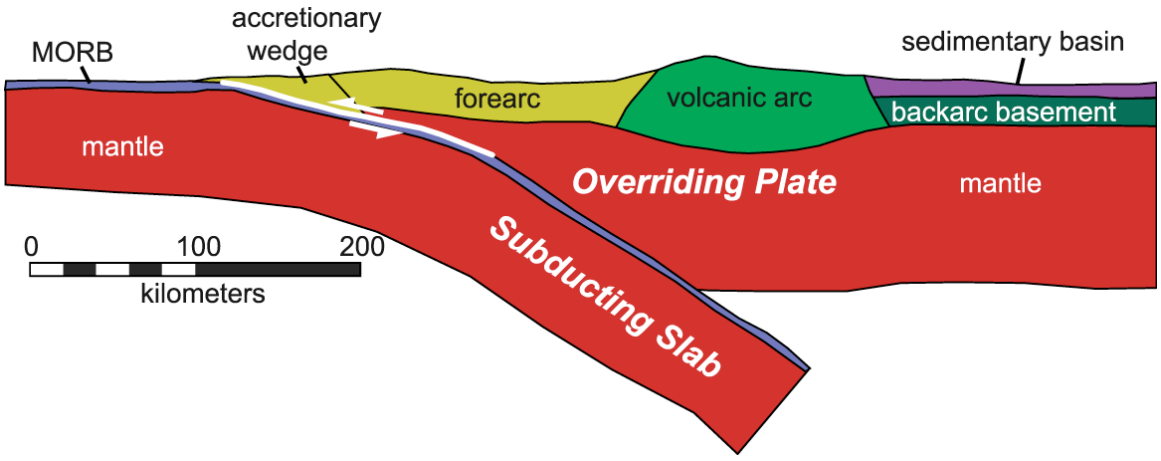

Figure 5.5. 2D FEM design [from *Masterlark and Hughes*, 2008] used for construction of the starting density model and for designation of the geologic units used in the factor analysis.

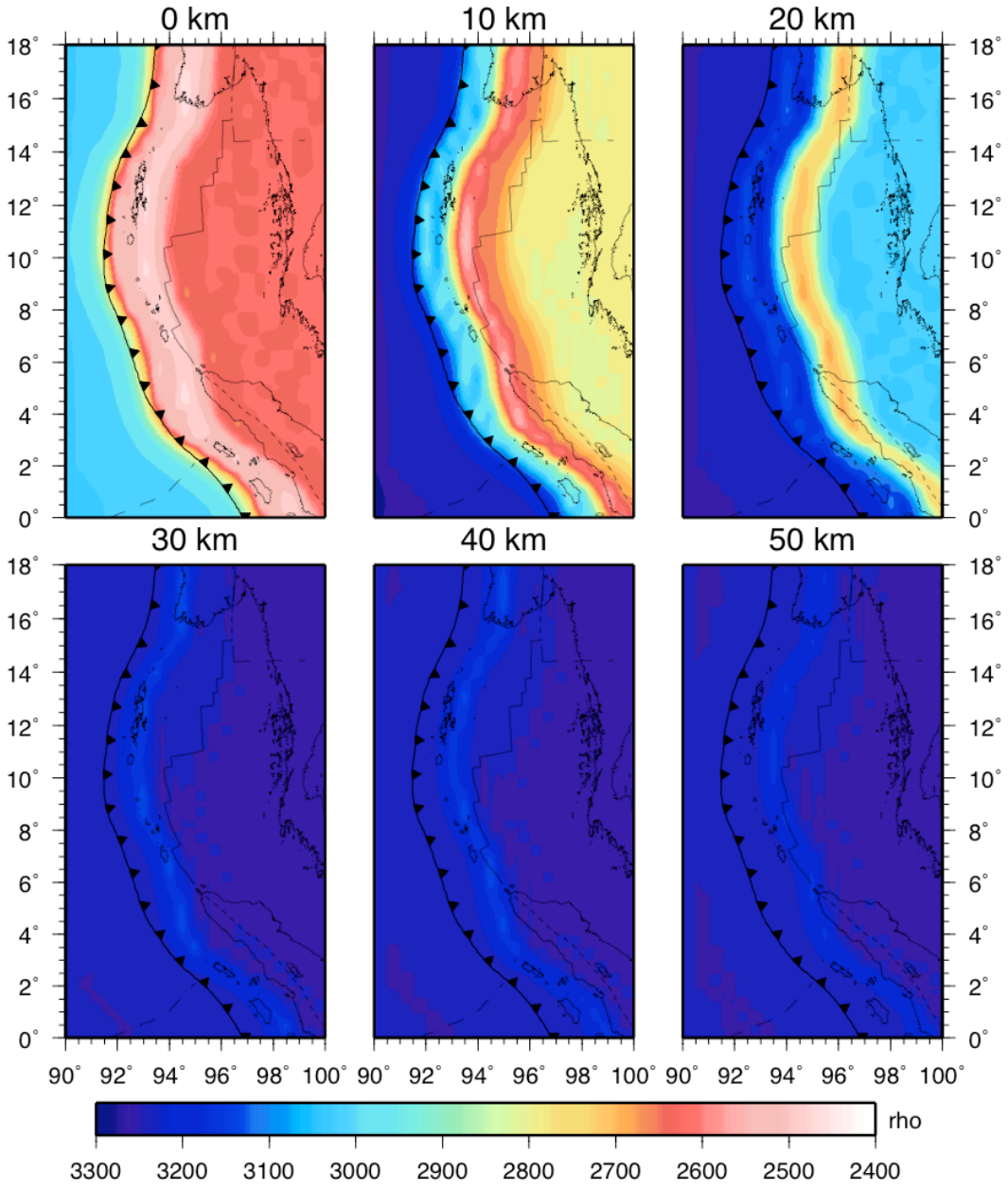

Figure 5.6a. Starting density model constructed from FEM element centroids as discussed in text.

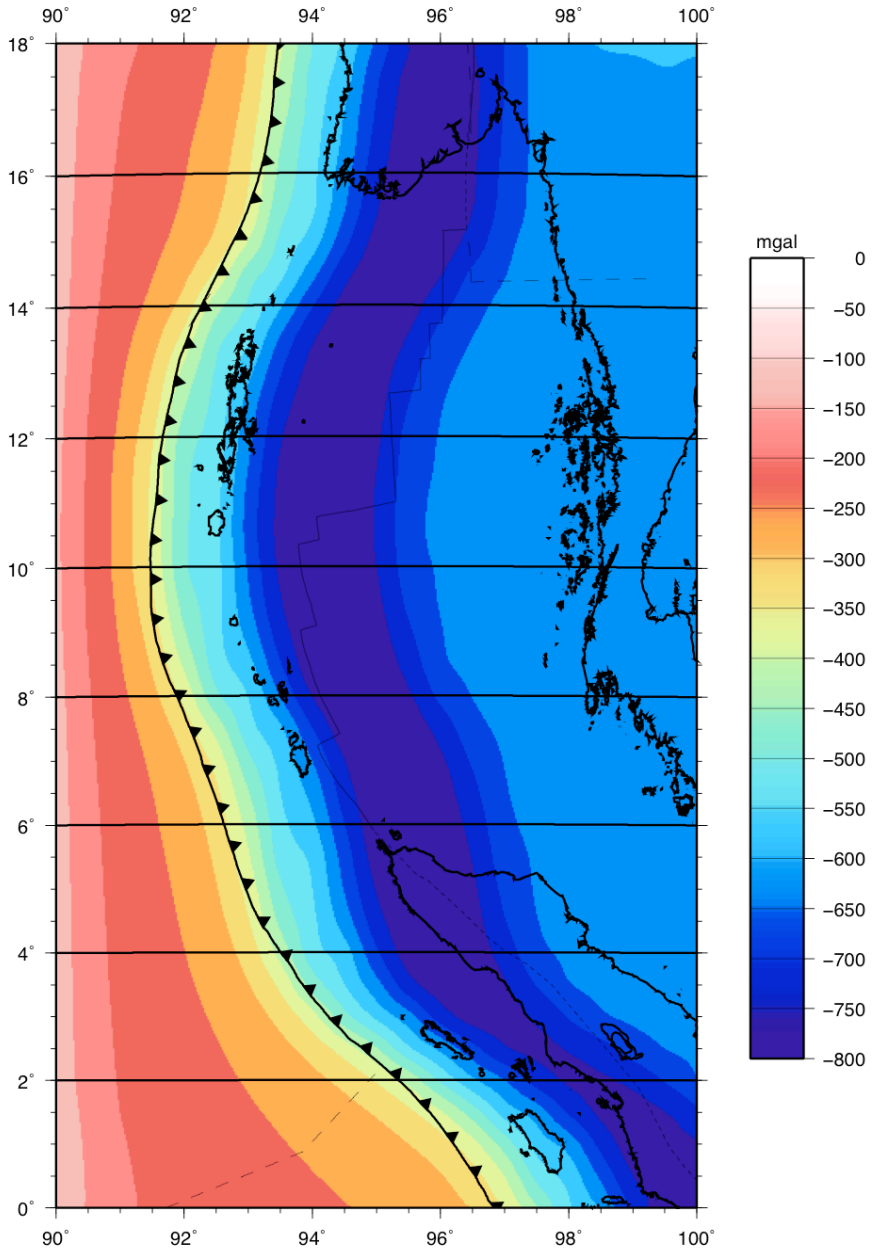

Figure 5.6b. Forward calculation of gravity due to starting density model (Figure 5.6a).

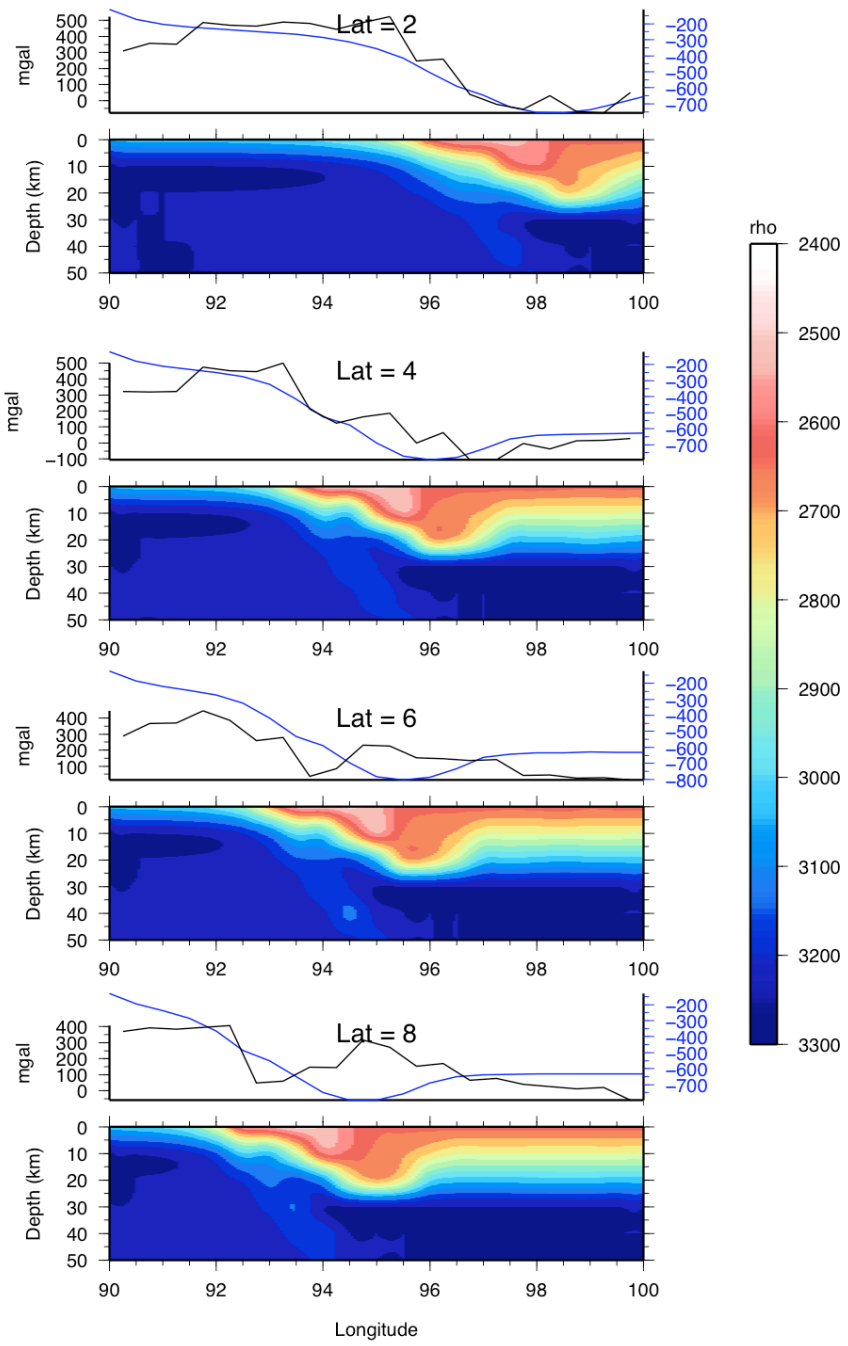

Figure 5.6c. Latitude cross-sections of starting density model with GLQ calculated gravity (blue) and Bouguer anomaly (black) from Figure 5.4.

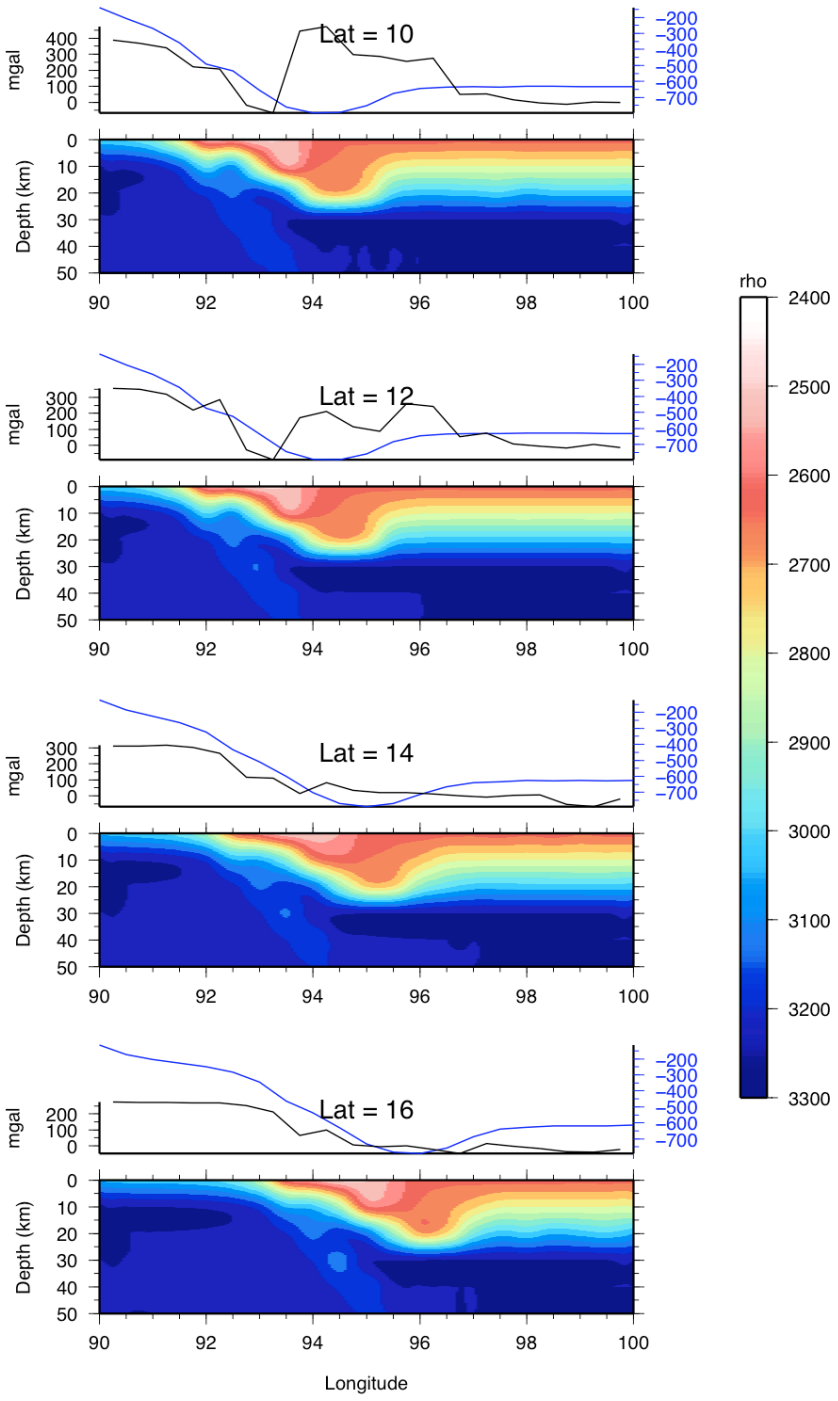

Figure 5.6c. (Continued)

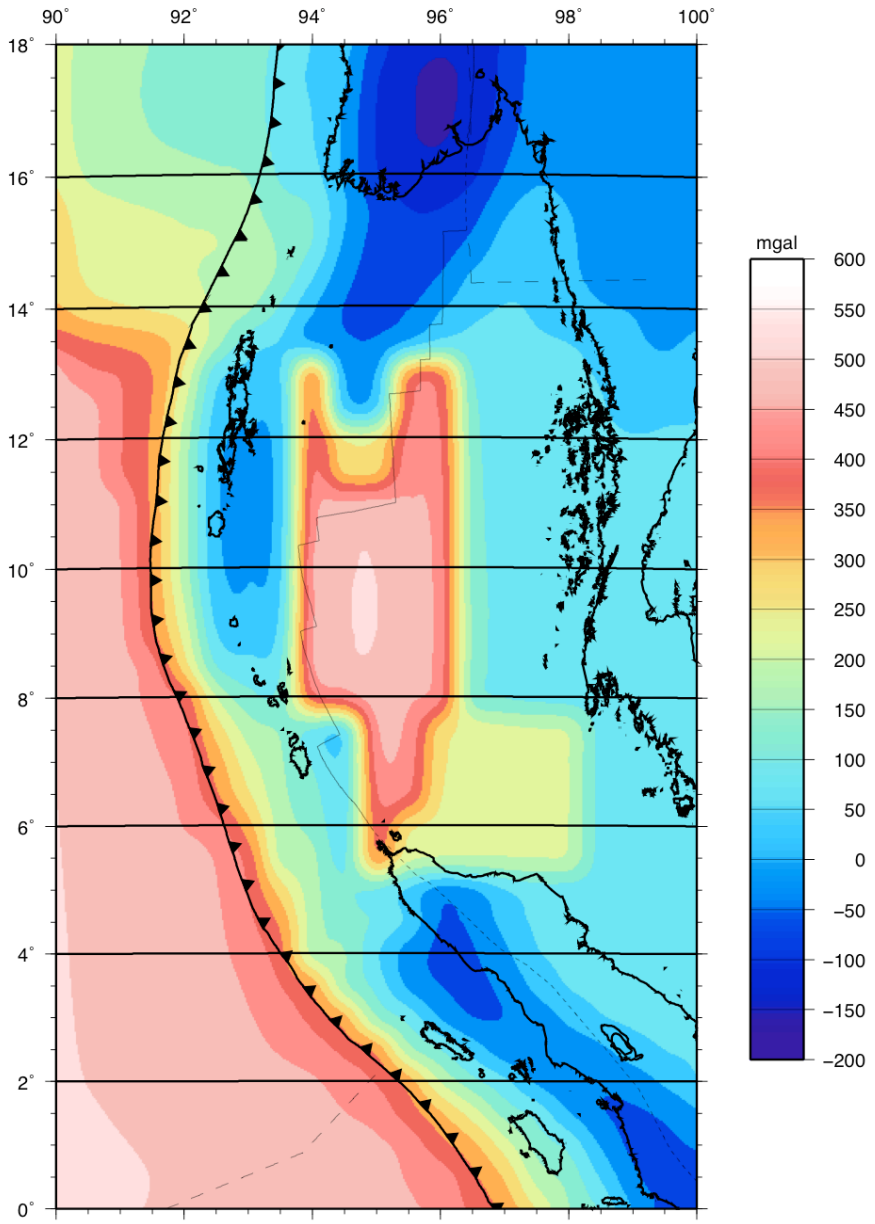

Figure 5.7a. Forward gravity calculation of adjusted density model.

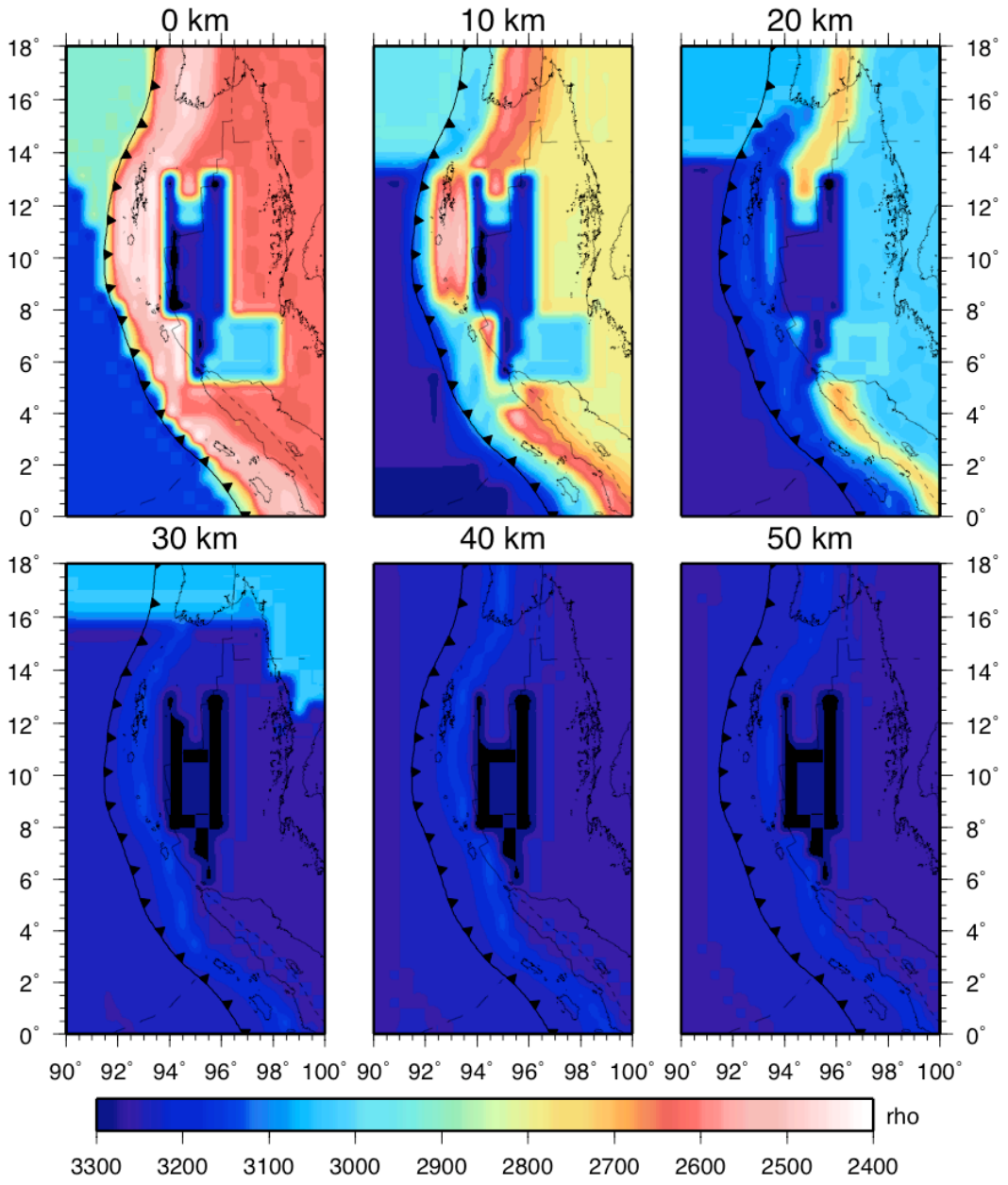

Figure 5.7b. Adjusted Density model. Three major changes relative to Figure 5.5b are sufficient to match long wavelength features of the observed gravity: 1) thinned crust in the Andaman Basin and thus higher density mantle at shallower depths, 2) deeper crustal roots beneath Burma and the Malay Peninsula, and 3) lower density Bengal fan sediments in the NE.

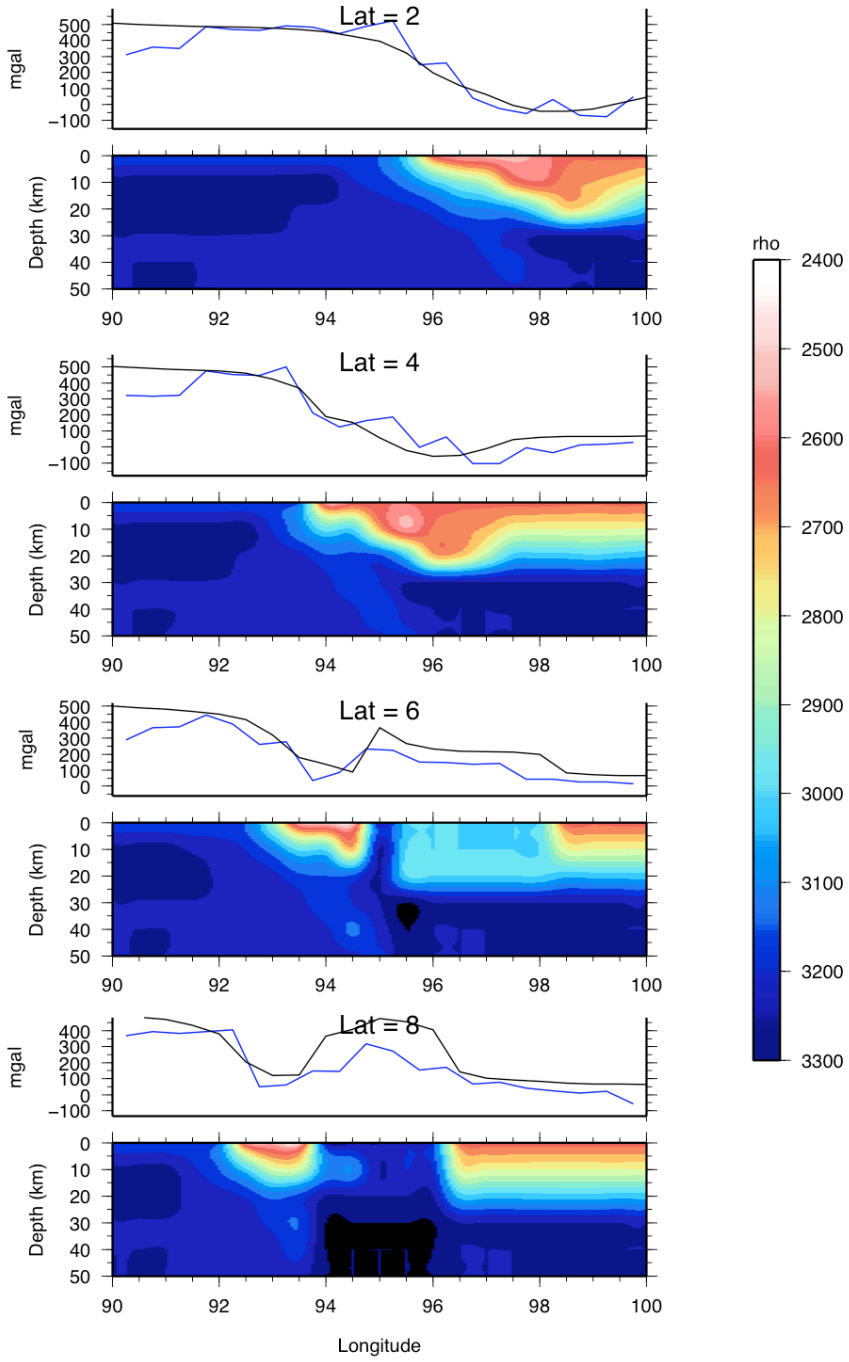

Figure 5.7c. Latitude cross-sections of adjusted density model with GLQ calculated gravity (blue) and Bouguer anomaly (black) from Figure 5.4.

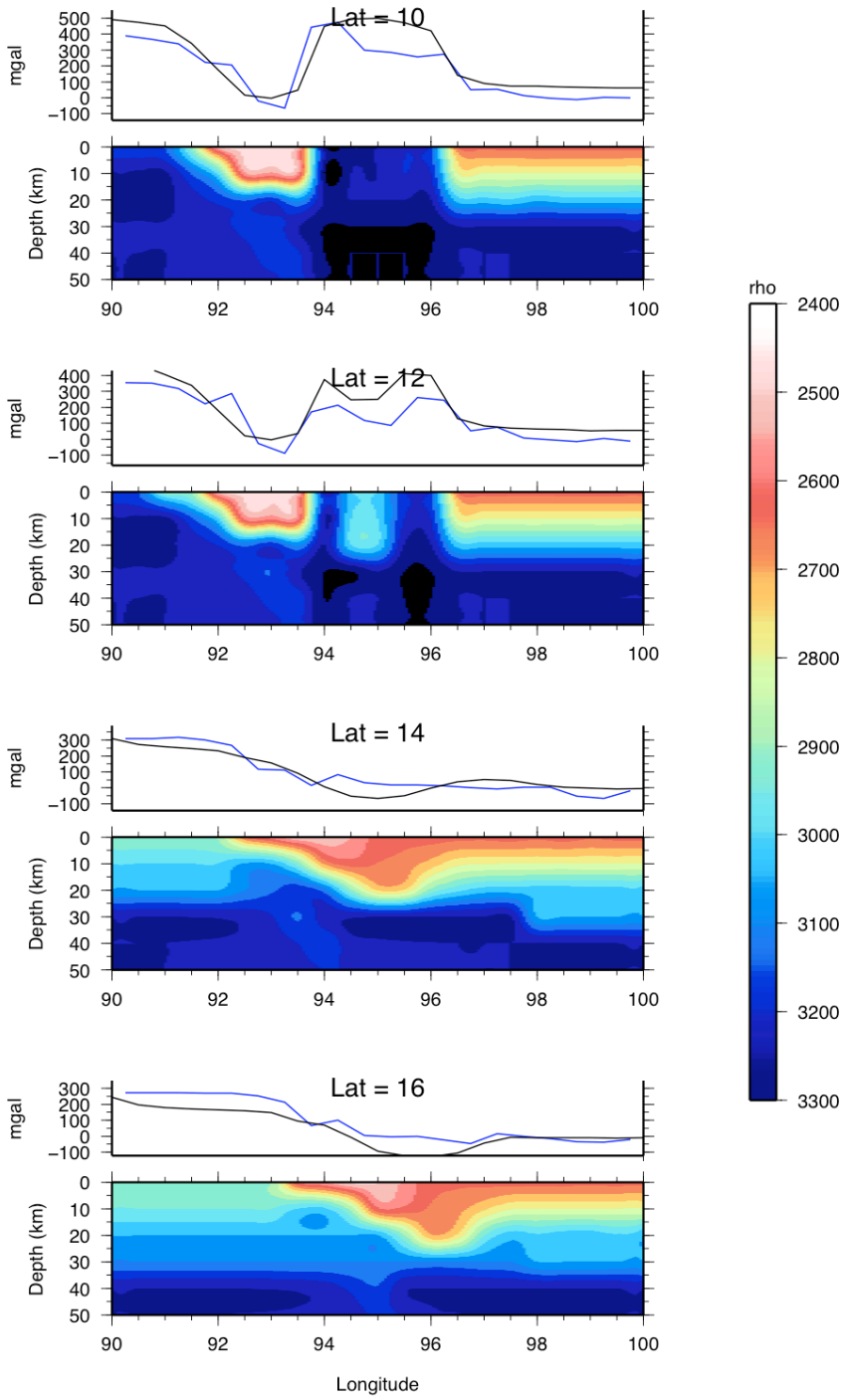

Figure 5.7c (continued).

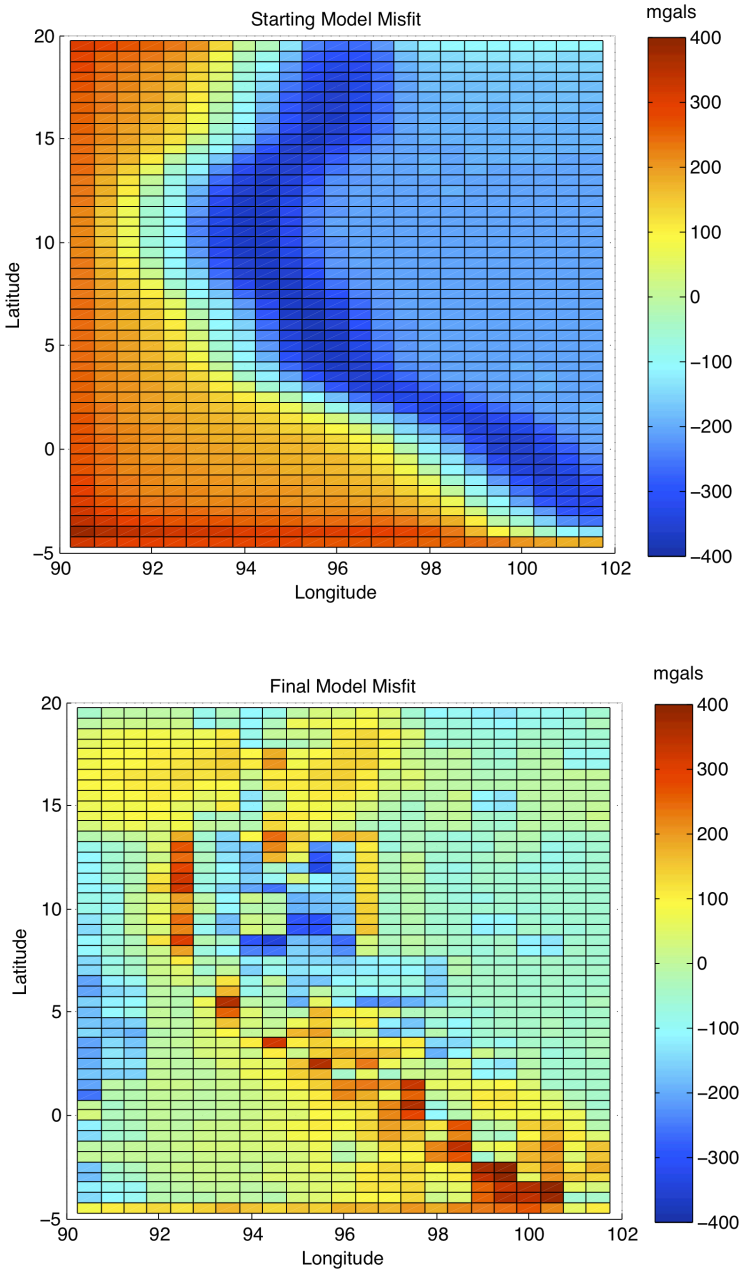

Figure 5.8. Comparison of misfit at each model prism for the starting model constructed from the FEM (top) and for the final model (bottom). Misfit values are shown after removal of the mean misfit, as discussed in text.

CHAPTER 6: Conclusions

The teleseismic tomography and relocation studies presented herein achieve significant advances in the resolution of teleseismic data, which in turn contributes to advancing our understanding of the structure of the Sumatra-Andaman subduction zone. Despite the difficulties posed by the remoteness of the region, subduction zone structure has been determined to a level of precision approaching that of other subduction zones where much better regional station coverage exists. In Chapter 2, the results revealed that the lithospheric slab beneath northern Sumatra is folded throughout the upper mantle (e.g. Figure 2.4, 2.S8). The correlation of this feature with the curvature of the trench and volcanic arc, the locations of the epicenters of the 2004 and 2005 great earthquakes, and with the arcuate shape of a tightly clustered group of earthquakes on the megathrust at shallow depths (Figure 4.11), suggests that this fold is a primary feature of the subducting plate that may influence rupture propagation in the region.

In Chapter 3, I described and illustrated the benefits of treating the teleseismic tomography problem as nonlinear. Images of the subducting slab can be greatly sharpened and focused when an iterative scheme is employed with data reweighting and source relocation between iterations. These techniques have previously proven successful for local earthquake tomography (LET) studies with dense networks of sources and receivers. The technical limitations that have prevented their broader usage at larger scales are slowly diminishing as global seismic catalogs increase in size and coverage. The Sumatra-Andaman region, with its improved distribution of seismicity following the 2004 and 2005 great earthquakes, served as a test case for the application of

high-precision LET techniques to teleseismic scales. The results presented in Chapter 3 confirm that there is resolution to be gained in teleseismic tomography models by applying nonlinear techniques. This is best illustrated by the improved images of the subducting slab below Burma (e.g. Figures 3.9b, 3.10b, 3.11b, 3.12, 3.13), where the nonlinear solution including source relocation recovered anomalies in the slab where there were gaps previously (e.g. Figure 2.2). These images revised the interpretation of a slab tear beneath Burma and may have similar implications for slab continuity elsewhere across the earth.

The recovery of a continuous slab in the tomography images beneath Burma can be attributed mostly to improving the accuracy of the regional earthquake locations within the iterative tomographic method presented in Chapter 3. These event locations were determined using more accurate 3-D global and regional velocity models and more precise differential times, as described in Chapter 4. The use of multiple event relocation techniques, such as the double-difference (DD) method, has many well-known advantages over single event relocation techniques. As I have shown in Chapter 4, these advantages lead to improvements in event locations at teleseismic distances as well. In regions where local data are scarce, these techniques produce better constraints on the spatio-temporal development of seismicity than is otherwise possible. For the important Sumatra seismic sequences of 2004 and 2005, aftershock relocations better define slab and megathrust geometry (e.g. Figure 4.7) and have revealed discrete seismic features on the megathrust (Figures 4.11, 4.13) that were not readily visible in teleseismic catalogs.

In Chapter 5, density modeling of the region was conducted using newly available satellite data and a fully 3-D spherical modeling technique. More commonly employed gravity modeling techniques build 3-D density models by constructing polygons in 2-D profiles and simply interpolating between profiles to obtain 3-D structure. In contrast, the spherical prism method allows construction of more realistic 3-D density models at the resolution of the gravity data. The resulting density model, presented in Chapter 5, helps to constrain the structure of the Sumatra-Andaman region at shallow depths where the resolving power of the teleseismic data is minimal.

Taken together, these studies present novel ways of determining 3-D plate boundary structure, from the surface to the lower mantle, in a region that is poorly sampled by precise local data. The results show significant improvements over previous studies in the region, as summarized by Figure 6.1. Application of these techniques to other subduction zones can be expected to yield a similar sharpening of images of slab structure and earthquake distribution.

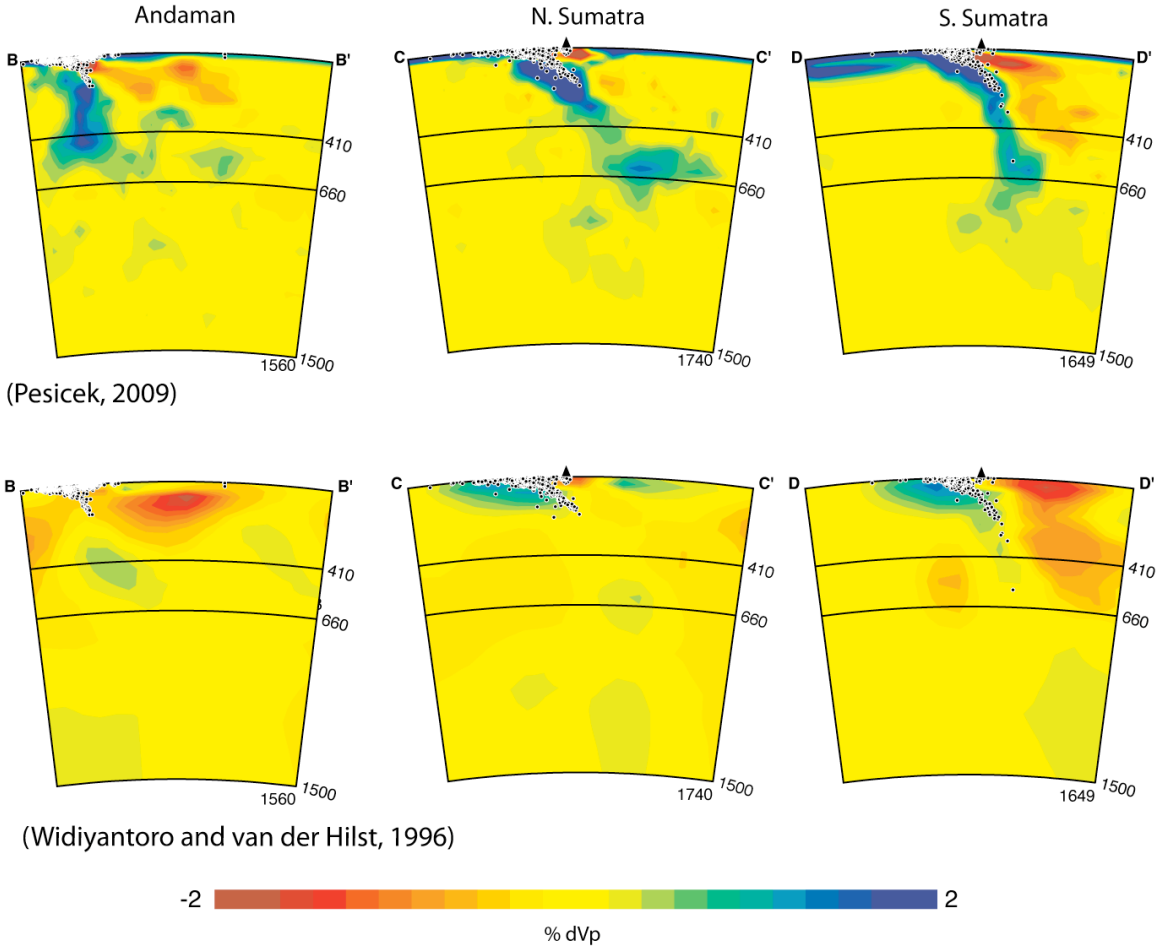

Figure 6.1. Comparison of the tomography model presented in Chapter 3 (top) and the model of Widiyantoro and van der Hilst [1996] (reference listed in Chapter 2) along 3 different cross-sections (positions shown in Figure 2.1) through the Sumatra-Andaman region. Earthquake locations (circles) are improved double-difference relocations, as discussed in Chapter 4.